Dynamics and thermodynamics of molecular motor-cargo systems

Von der Fakultät Mathematik und Physik der Universität Stuttgart
zur Erlangung der Würde eines Doktors der
Naturwissenschaften (Dr. rer. nat.) genehmigte Abhandlung

Vorgelegt von

Eva Zimmermann

aus Reutlingen

Hauptberichter:	Prof. Dr. Udo Seifert
Mitberichter:	Prof. Dr. Christian Holm

Tag der Einreichung:	13. Februar 2015
Tag der mündlichen Prüfung:	21. April 2015

II. Institut für Theoretische Physik der Universität Stuttgart

2015

Contents

Abbreviations and symbols

Abbreviations

ATP	adenosine triphosphate
ADP	adenosine diphosphate
$\mathrm{P_i}$	inorganic phosphate
FDT	fluctuation-dissipation theorem
LDB	local detailed balance
NESS	nonequilibrium steady state
VACF	velocity autocorrelation function

Mathematical notations

$\mathrm{d}, \mathrm{đ}$	complete, incomplete differential
$\delta(t)$	Dirac distribution
$\dot{x}$	time derivative of x
∂_x	partial derivative with respect to x
$\tilde{f}$	Fourier transform of function f
$\lfloor . \rfloor$	floor function
$\bar{x}$	observable x averaged with the Gaussian distribution
$\langle . \rangle$	ensemble average
$\mathrm{S}(t)$	sawtooth wave
$\hat{v}$	averaged observable v in the limit of time-scale separation

Symbols

$C_{\dot{x}}$	velocity autocorrelation function
c_i	concentration of nucleotide species i
δ	step size of the probe
d, d_{ij}^{α}	full and partial step size of the motor
D	diffusion coefficient

D_w, D_Ω	effective diffusion coefficient; detailed, coarse-grained system
E	internal energy
F	free energy
F^{enz}	free energy of the motor
F^{sol}	free energy of the solvent
ΔF_{ij}^{α}	free-energy change (including solvent) due to transition (i, j, α)
$\Delta \mathcal{F}_{ij}^{\alpha}$	free-energy change for equilibrium concentrations due to transition (i, j, α)
f, f_{ex}	(constant) external force
$f_{\mathrm{ex}}^{\mathrm{st}}$	stall force
γ	friction coefficient
$\gamma^{\pm}(x)$	transition rates of the probe
$j(x)$, $j_i^x(x)$	probability current concerning a continuous variable; continuous, hybrid state space
j_{ij}, $j_{ij}^{\alpha}(x)$	transition/net current between states i, j; discrete, hybrid state space
j_{ij}^{α}	operational current between states i, j
J_a, $J_a^{\pm}$	net and directed cycle currents of cycle a
κ	spring constant of the linker
λ	coupling strength between motor and linker
η	friction coefficient of the motor
η_{Q}	pseudo efficiency
η_{S}	Stokes efficiency
η_{T}	thermodynamic efficiency
$\Omega^{\pm}$, Ω_{ij}^{α}	coarse-grained transition rates
$p(x)$, p_i, $p_i(x)$	probability distribution; continuous, discrete, hybrid state space
P_i	marginal distribution
$\hat{p}(x)$, $\hat{p}_i(x)$, $\hat{P}_i$	probability (distribution) in the limit of time-scale separation
$p_i^{\mathrm{st}}(x)$, P_i^{st}	probability (distribution) at stall
$p^G(y)$	Gaussian distribution
$\dot{Q}_{\mathrm{P}}$, $\dot{Q}_{\mathrm{M}}$	average dissipation rate of probe and motor
$R_{\dot{x}}$	response function
σ^2	variance of the Gaussian distribution
s^{tot}	total entropy
s^{sys}=$s^{\mathrm{enz}} + s^{\mathrm{sol}}$	entropy of the system (motor plus solvent)
s^{med}	entropy of the heat bath
s	stochastic entropy

$\dot{S}$	average entropy production rate
τ, T	time intervals
θ^+, θ^-, $\theta_{ij}^{\alpha,+}$, $\theta_{ij}^{\alpha,-}$	mechanical load sharing factors
μ_i	chemical potential of nucleotide species i
$\Delta\mu$, $\Delta\mu_{ij}^{\alpha}$	free-energy change of the solvent due to nucleotide binding, release or ATP hydrolysis/synthesis
V	potential of the linker
$\mathcal{V}$	potential or free energy
ν	local mean velocity
v	average velocity
W	work, corresponding to the external force
w_0, k_{ij}^{α}	attempt frequencies
w_{ij}, $w_{ij}^{\alpha}(x)$, $w^{\pm}$	transition rates of the motor; discrete, hybrid state space, one-state process
χ	microstates
χ_{ij}	chemical load sharing factor
$\xi(t)$, $\zeta(t)$	Gaussian white noise
x, n	spatial variables
y	elongation of the linker

Kurzfassung

Diese Arbeit widmet sich der Dynamik und Thermodynamik molekularer Motoren. Insbesondere wird der Einfluss eines angekoppelten Testteilchens auf die Eigenschaften des Motors untersucht. Molekulare Motoren sind Enzyme, die chemische Energie, die z.B. aus der Hydrolyse von ATP gewonnen wird, in mechanische Bewegung umwandeln können. Sie sind an einer Reihe von wichtigen Vorgängen, die die Funktionsweise biologischer Zellen ausmachen, beteiligt, wie beispielsweise dem Transport von Organellen, der Zellteilung, der Kontraktion von Muskeln oder sogar der Synthese von ATP.

Obwohl sie mikroskopische Objekte von der Größenordnung einiger Nanometer sind und daher stark von thermischen Fluktuationen beeinflusst werden, zeigen sie eine außergewöhnlich stabile und effiziente Funktionsweise. Folglich ist es in der Physik, Biologie, Chemie und Medizin von großem wissenschaftlichen Belang, ihre Struktur und Wirkungsweise zu verstehen.

Experimentelle Untersuchungen beinhalten üblicherweise Testteilchen, die am Motor befestigt sind und dazu dienen, die Motorbewegung darzustellen und externe Kräfte auf den zu untersuchenden Motor auszuüben. Da diese Testteilchen oft mehr als zehn mal größer sind als der Motor selbst, kann man davon ausgehen, dass sie eine erhebliche Beeinträchtigung für den Motor darstellen und dessen Dynamik und Thermodynamik nachhaltig beeinflussen. Eigenschaften des Motors aus experimentellen Daten abzuleiten ist eine heikle Angelegenheit, da einerseits nur die Trajektorie des Testteilchens zugänglich ist und andererseits jedes Messergebnis dem Gesamtsystem bestehend aus Motor und Testteilchen zuzuordnen ist anstatt nur dem Motor. Oftmals ist es *a priori* unklar, welche Motoreigenschaften vom Testteilchen beeinflusst werden und wie stark sich der Einfluss der Testteilchens auswirkt.

Da sie Teil mesoskopischer biologischer Systeme sind, ist die Dynamik molekularer Motoren nicht nur von thermischen Fluktuationen beeinflusst sondern findet meist sogar im Nichtgleichgewicht statt. Die theoretische Beschreibung dieser mikroskopischen Maschinen erfordert daher die Berücksichtigung von Fluktuationen und Nichtgleichgewichtsbedingungen. Einen solchen Rahmen bieten die stochastische Dynamik und stochastische Thermodynamik.

In dieser theoretischen Arbeit untersuchen wir die Dynamik und Energetik molekularer Motoren, die an ein Testteilchen gekoppelt sind, im Hinblick auf Effekte, die durch das Vorhandensein des Testteilchens verursacht werden. Unser Ziel ist es,

festzustellen, wie das Testteilchen verschiedene Eigenschaften der Motordynamik und -Energetik beeinflusst und Charakteristika experimenteller Daten zu identifizieren, die Auswirkungen des angekoppelten Testteilchens darstellen. Zudem entwickeln wir eine thermodynamisch konsistente Methode zur Vereinfachung der theoretischen Beschreibung, wobei das System aus Motor und Testteilchen auf ein effektives Motorteilchen abgebildet wird. Um derartige Effekte zu untersuchen, erstellen wir ein allgemeines Modell mit zwei Freiheitsgraden, welche Motor und Testteilchen darstellen und über eine elastische Verbindung gekoppelt sind. Mittels Monte Carlo Simulationen oder durch numerisches Lösen der Fokker-Planck Gleichung erhalten wir Ergebnisse, die wir anschließend mit experimentellen Daten vergleichen. Gelegentlich verwenden wir auch vereinfachte Modelle, die analytisch gelöst werden können.

Kapitel 2: Grundlagen Dieses Kapitel bietet einen kurzen Überblick über stochastische Dynamik, stochastische Thermodynamik und molekulare Motoren. Zum Konzept der stochastischen Dynamik gehört die Langevin-Gleichung für einzelne Trajektorien ebenso wie die Fokker-Planck- und die Master-Gleichung auf Ensemble-Ebene. Die Interpretation des ersten und zweiten Hauptsatzes entlang einer Einzeltrajektorie bildet das Grundprinzip der stochastischen Thermodynamik. Wir bieten einen kurzen Einblick in das Vorkommen und die Funktionsweisen molekularer Motoren sowie eine kurze Übersicht über experimentelle und theoretische Herangehensweisen, die bei der Erforschung molekularer Motoren zum Einsatz kommen.

Kapitel 3: Modellierung Viele Experimente mit einzelnen molekularen Motoren beinhalten Testteilchen, die an den Motor gekoppelt sind. Die theoretische Analyse solcher Untersuchungen berücksichtigt hingegen oftmals nur die Freiheitsgrade, die den Motor darstellen. In diesem Kapitel stellen wir ein einfaches Modell mit zwei Freiheitsgraden vor, welche Motor und Kugel repräsentieren. Beide Teilchen sind mittels einer elastischen Verbindung gekoppelt. Die Dynamik des kombinierten Systems besteht aus diskreten Sprüngen des Motors und kontinuierlicher Brownscher Bewegung des Testteilchens. Wir berücksichtigen sowohl Motormodelle mit nur einem internen Zustand als auch solche mit mehreren internen Zuständen. Diese Art von Modellen bezeichnen wir als Hybrid-Modelle.

Kapitel 4: Effizienz molekularer Motoren mit Testteilchen Da molekulare Motoren oftmals Arbeit gegen Reibungskräfte verrichten, existieren verschiedene Effizienzdefinitionen. Die thermodynamische Effizienz bezieht sich auf die Arbeit gegen externe Kräfte, wohingegen die Stokes oder verallgemeinerte Effizienz und die Pseudo-Effizienz auch Arbeit gegen Reibungskräfte berücksichtigen, im Falle

der Pseudo-Effizienz werden sogar Fluktuationen erfasst. Diese drei Effizienzdefinitionen wurden alle anhand der F_1-ATPase untersucht. Die F_1-ATPase ist ein rotierender Motor, der an der ATP Synthese in biologischen Zellen beteiligt ist. Diese Experimente lieferten Effizienzen von nahezu 1 was bedeutet, dass die F_1-ATPase fast die gesamte chemische Energie in Rotation umzusetzen vermag. Wir verwenden das Hybrid-Modell mit einem Ein-Zustands-Motor, um die drei Effizienzdefinitionen sowohl mittels Simulationen als auch mittels einer Gauß-Näherung zu untersuchen. Da unser Motor eine direkte Kopplung zwischen chemischer Reaktion und mechanischem Schritt enthält, erreicht die thermodynamische Effizienz den Wert 1 bei Maximallast. Aufgrund der diskreten Sprünge des Motors ist die Stokes-Effizienz wesentlich kleiner als 1 für kleine ATP Konzentrationen, was jedoch für höhere ATP Konzentrationen weniger relevant wird. Im Gegensatz dazu erreicht die Pseudo-Effizienz Werte größer als 1 nahe dem Gleichgewicht und für eine sehr asymmetrische Freie Energie Oberfläche mit einer Barriere nahe des Ausgangszustands. Im Vergleich mit experimentellen Daten zeigt sich eine gute Übereinstimmung für alle drei Effizienzen. Abweichungen, die bei sehr kleinen Phosphatkonzentrationen auftreten, sind der Einfachheit unseres Modells geschuldet.

Kapitel 5: Einfluss des Testteilchens auf die Motordynamik Dieses Kapitel befasst sich mit Auswirkungen des Testteilchens auf die Dynamik des Motors, die sich in experimentell zugänglichen Größen zeigen, welche aus der Testteilchentrajektorie gewonnen werden können. Wir befassen uns insbesondere mit der Geschwindigkeitsautokorrelationsfunktion (VACF) und der Antwortfunktion des Testteilchens sowie der Wartezeitenverteilung der Motorsprünge. Zunächst betrachten wir drei analytisch lösbare vereinfachte Versionen des Hybrid-Modells mit einem Ein-Zustands-Motor, um festzustellen, welche Art von Motordynamik welche Art Struktur in der VACF und der Antwortfunktion verursacht. Wir untersuchen speziell Motormodelle mit von der Kugelposition unabhängigen Sprungraten, vollständig gekoppelte kontinuierliche Motormodelle und Modelle mit deterministischen Sprungzeiten. Dies zeigt uns, dass jegliche Art von Struktur in der VACF, die über einen exponentiellen Zerfall hinausgeht, diskrete Motorsprünge voraussetzt, die nicht rein zufällig auftreten. Simulationen des ursprünglichen Modells zeigen ausgeprägte Oszillationen, die der periodischen Struktur bei deterministischen Sprungzeiten ähneln. Folglich muss die Kopplung dazu führen, dass Motorsprünge nicht rein zufällig auftreten. Übereinstimmend damit zeigt sich in der Wartezeitenverteilung ein Maximum, was auf eine nicht markovsche Dynamik hinweist. Dies ist besonders zu beachten, da ein Maximum in der Wartezeitenverteilung üblicherweise weiteren Zwischenzuständen des Motors zugeschrieben wird. In Experimenten mit der F_1-ATPase bestimmte Korrelations- und Antwortfunk-

tionen stimmen qualitativ mit unseren Simulationsergebnissen überein.

Kapitel 6: Mechanismus der Energieumwandlung In diesem Kapitel untersuchen wir den Einfluss des Testteilchens auf den Mechanismus der Energieumwandlung im Motor. Der Vorgang der Energieumwandlung im Motor kann untersucht werden, indem man so starke externe Kräfte am Testteilchen anlegt bis der Motor stehen bleibt und die Geschwindigkeit im Mittel verschwindet. Die maximale Kraft entspricht dann der maximalen Arbeit pro Motorschritt, die aus dem System entnommen werden kann. Um die Auswirkungen des Testteilchens auf die Energetik des Motors zu bestimmen, vergleichen wir die Maximalkraft, je nachdem ob die externe Kraft am Testteilchen oder direkt am Motor angreift. Da sich der Einfluss des Testteilchens auf die Motordynamik mithilfe der Netzwerktheorie einsichtig darstellen lässt, führen wir in diesem Kapitel zunächst die Netzwerkdarstellung des Hybrid-Modells ein. Diese erhält man, indem man die Kugelvariable diskretisiert. Zudem simulieren wir spezielle Hybrid-Modelle mit unizyklischen und multizyklischen Motoren. Unsere Analyse zeigt, dass die Maximalkraft für unizyklische Motoren mit und ohne Testteilchen gleich ist. Bei multizykilschen Motoren hingegen hängt die Maximalkraft von der Kugelgröße ab und kann kleiner, gleich oder sogar größer als im Fall ohne Testteilchen sein. Aus experimenteller Sicht ist es wichtig zu berücksichtigen, dass die gemessene Maximalkraft dem Gesamtsystem Motor-Testteilchen entspricht und nicht notwendigerweise Eigenschaften des Motors widerspiegelt. Die beobachtete Variation der Maximalkraft dient als Beweis, dass der untersuchte Motor multizyklisch ist. Erstaunlicherweise kann durch Anbringen eines Testteilchens die maximal zu extrahierende Arbeit sogar vergrößert werden.

Kapitel 7: Thermodynamisch konsistente Vergröberung der Dynamik Während Modelle mit mehreren Freiheitsgraden, wie unser Hybrid-Modell, präziser sind und den eigentlichen experimentellen Versuchsaufbau widerspiegeln, bestehen die meisten theoretischen Modelle nur aus einem Teilchen, das den Motor darstellt. Die Vorteile solcher Ein-Teilchen Modelle ist naheliegend: sie sind mathematisch wesentlich einfacher zu handhaben. Außerdem werden sie oft verwendet, um grundsätzliche Konzepte zu illustrieren. In diesem Kapitel entwickeln wir eine Methode zur Vergröberung der Dynamik, die ein Modell mit zwei gekoppelten Freiheitsgraden für Motor und Testteilchen auf ein effektives Ein-Teilchen Modell abbildet, indem die Dynamik des Testteilchens dynamisch und thermodynamisch konsistent aus der Beschreibung entfernt wird. Die vergröberten Raten unterliegen einer lokalen detaillierten Balance Bedingung und führen zu den korrekten mittleren Strömen. Zusätzlich bleiben die mittlere Entropieproduktion und die thermodynamische Effizienz erhalten. Im Allgemeinen zeigen die vergröberten Raten

eine kompliziertere Kraft- und Konzentrationsabhängigkeit als die Raten eines entsprechenden Ein-Teilchen Modells. Nur unter der unrealistischen Annahme, dass das Testteilchen extrem schnell relaxiert, stimmen die Raten überein. Schließlich wenden wir unsere Vergröberungsmethode auf zwei beispielhafte Modelle für die F_1-ATPase und Kinesin an und zeigen, wie ein solches vergröbertes Modell aus experimentellen Daten konstruiert werden kann.

Abstract

This thesis is dedicated to the dynamics and thermodynamics of molecular motors. In particular, it focuses on the influence of a coupled probe particle on the properties of the motor protein. Molecular motors are enzymes that are able to convert chemical energy available from, e.g., ATP hydrolysis into mechanical motion. They are involved in a variety of important processes that account for cellular function like transport of organelles, cell division, muscle contraction and even ATP synthesis.

Although molecular motors are microscopic objects of the size of several nanometers whose dynamics is strongly influenced by thermal fluctuations, they exhibit a surprisingly stable and efficient performance. Hence, understanding the structure and mode of operation is of great scientific relevance in the fields of physics, biology, chemistry and medicine.

Experimental studies typically imply some kind of probe particle that is attached to the motor and serves as a sensor to visualize the motor motion and that allows to exert forces on the motor under investigation. Since these probe particles are often more than ten times larger than the motor itself, they can be expected to constitute a considerable hindrance to the motor and to severely influence its dynamics and thermodynamics. Inferring properties of the motor from experimental data is a delicate task since on the one hand, only the trajectory of the probe is directly accessible, while on the other hand any measurement results apply to the motor-probe complex rather than the motor itself. In the first place, it is often unclear which properties of the motor are influenced by the coupled probe and to what extent.

Belonging to the class of mesoscopic biological systems, the dynamics of molecular motors is subject to thermal fluctuations. Furthermore, the motors operate under genuine nonequilibrium conditions. Hence, a theoretical description of these microscopic machines requires the consideration of fluctuations and nonequilibrium conditions, which is provided by the framework of stochastic dynamics and stochastic thermodynamics.

In this thesis, we theoretically analyze the dynamics and energetics of a molecular motor coupled to a probe particle with regard to the effects caused by the presence of the probe. Our goal is to determine the influence of the probe particle on several properties of the motor dynamics and energetics and to identify features in the experimental data that are consequences of attaching a probe and

do not belong to the motor itself. Furthermore, we provide a thermodynamically consistent procedure to simplify the theoretical description by mapping motor and probe to an effective motor particle. In order to investigate these effects we set up a generic model comprising two degrees of freedom representing motor and probe, respectively, that are coupled via an elastic linker. Results are obtained from Monte Carlo simulations of the system and from numerically solving the Fokker-Planck equation. In some cases, we also apply simplified models that can be solved analytically. We also compare our results to available experimental data.

Chapter 2: Basics In this chapter, we briefly present an overview of stochastic dynamics, stochastic thermodynamics and molecular motors. The concept of stochastic dynamics includes the Langevin equation for an individual trajectory and the Fokker-Planck and master equation on the ensemble level. The interpretation of the first and second law along a single fluctuating trajectory constitute the basic principles of stochastic thermodynamics. We briefly review the field of application and the general mode of operation of molecular motors and present experimental as well as theoretical approaches applied to motor proteins.

Chapter 3: Modeling of motor and probe dynamics Many single molecule experiments for molecular motors comprise not only the motor but also large probe particles coupled to it. The theoretical analysis of these assays, however, often takes into account only the degrees of freedom representing the motor. In this chapter, we introduce a simple model comprising two degrees of freedom representing the motor and the probe particle. Both constituents are coupled via an elastic linker. The combined dynamics consists of discrete steps of the motor and continuous Brownian motion of the probe. We discuss motor models with a single internal state as well as motor models with several internal states. We will refer to these kind of models as hybrid models.

Chapter 4: Efficiencies of molecular motors with probe particles Since molecular motors often perform work only against viscous load, several different definitions of efficiency exist. The genuine thermodynamic efficiency focuses on the work against an external force, whereas the Stokes or generalized efficiency and the pseudo efficiency also consider work against viscous friction, the latter even fluctuations. These three definitions of efficiency have all been experimentally studied for the F_1-ATPase, which is a specific rotary motor involved in ATP synthesis within cells. These experiments indicated values of almost 1 for all efficiencies suggesting that the F_1-ATPase can use the complete chemical energy to rotate the probe. Here we apply the hybrid model with a one-state motor to investigate the three types of efficiencies both in simulations and in a Gaussian approximation.

We find that the thermodynamic efficiency becomes 1 at stall conditions since our motor is tightly coupled. The Stokes efficiency is much smaller than 1 for small ATP concentrations due to the discrete nature of the motor steps which become less relevant with increasing ATP concentration. In contrast, we find that the pseudo efficiency becomes larger than 1 close to equilibrium conditions and for a very asymmetric free-energy landscape with a barrier close to the initial state. Comparing our theoretical results to the experimental data, we find overall good agreement for all three types of efficiencies. Deviations concerning the pseudo efficiency occur for small P_i concentrations due to the simplicity of the one-state motor model.

Chapter 5: Influence of cargo particle on motor dynamics This chapter is dedicated to effects caused by the influence of the probe on the motor dynamics that are visible in experimentally accessible quantities obtained from the trajectory of the probe. In particular, we investigate the velocity autocorrelation function (VACF) and the response function of the probe as well as the dwell-time distribution of the motor jumps. First, we use three simplified hybrid models with one-state motors that can be solved analytically to determine which kind of motor dynamics causes which kind of structure in the VACF of the probe. Specifically, we investigate a motor model with jump rates independent of the probe, a fully coupled motor model with continuous state space and a motor model with deterministic jump times. We find that additional structure in the VACF and response function beyond a single exponential decay requires discrete motor jumps that are not purely random and symmetric coupling between motor and probe. Since simulation results of the original hybrid model show distinct oscillatory behavior reminiscent of the periodic structure obtained for the deterministic motor jumps, we conjecture that the coupling of the probe causes the motor to jump less randomly. This is consistent with the analysis of the dwell-time distribution which exhibits a peak indicating a non-Markovian dynamics. Such a phenomenon is of particular interest since a peaked dwell-time distribution is usually attributed to additional (hidden) motor states. Experimentally obtained VACFs and response functions of the F_1-ATPase qualitatively agree with our simulation results.

Chapter 6: Energy transduction mechanism and stall force anomaly Here we focus on the influence of the probe on the energy transduction mechanism of the motor. Information about the energy transduction mechanism can be obtained by applying external forces to the motor-probe setup until the system reaches stall conditions with zero average velocity. The stall force corresponds to the maximum extractable work per motor step. In order to investigate the effect of the probe on the energetics of the motor, we compare the stall conditions when the external

force is applied via the probe particle with the case where it is applied directly to the motor. Since the effects of the probe particle on the energy transduction can be clearly presented using elements of network theory, we introduce the network description of the hybrid model in this chapter. The network representation is obtained by discretizing the state space of the probe. Additionally, we perform simulations of specific hybrid models with unicyclic and multicyclic motors. Our analysis reveals that for one-state motor models and unicyclic motor models, the stall force is not altered by the presence of the probe. For multicyclic motor models, however, the stall force with probe particle varies with probe size and can be smaller, equal to or even larger than the stall force of the bare motor. From an experimental point of view it is important to keep in mind that the measured stall force corresponds to the motor-probe setup and does not necessarily represent the motor properties. The observed variation of the stall force with probe size serves as proof that the motor is multicyclic. Furthermore, applying a probe particle can have the surprising effect that the maximum extractable work can be increased.

Chapter 7: Thermodynamically consistent coarse-graining method While multiparticle models like our hybrid model are more precise and represent the actual experimental setup, most theoretical models include only one particle representing the motor. The advantage of one-particle models is obvious: they are much easier to handle mathematically. Furthermore, they are often applied to illustrate basic ideas. In this chapter, we present a coarse-graining method that maps a model comprising two coupled degrees of freedom which represent motor and probe particle to such an effective one-particle model by eliminating the dynamics of the probe particle in a thermodynamically and dynamically consistent way. The coarse-grained rates obey a local detailed balance condition and reproduce the net currents. Moreover, the average entropy production as well as the thermodynamic efficiency is invariant under this coarse-graining procedure. Our analysis reveals that in general the coarse-grained rates exhibit a more complex force and concentration dependence than the corresponding a priori one-particle rates. Only by assuming unrealistically fast probe particles, the rates coincide. We apply this coarse-graining method to specific case studies of the F_1-ATPase and the kinesin motor. We also provide guidelines how such a coarse-grained model can be constructed on the basis of experimental data.

1. Introduction

Embedded in an aqueous solution, small biological systems like cells, proteins, DNA and vesicles as well as colloidal particles belong to the large class of soft matter objects. Such microscopic objects with a size of several nm to µm are subject to thermal fluctuations induced by collisions with the molecules constituting the surrounding solution. The resulting stochastic dynamics of the object is well known as Brownian motion and has been first described in the 19^{th} century by R. Brown [1]. Most biological systems perform specific operations that require permanent energy input. In the case of molecular motors, the energy supply is used to generate directed motion which comes along with dissipation of energy into the surrounding solvent. For constant energy input, the system reaches a nonequilibrium steady state (NESS) with constant average currents.

The mathematical and physical framework suitable to study such stochastic dynamics is based on the work of Einstein, Langevin and Smoluchowski [2–4]. The Langevin equation describes the evolution of a single trajectory subject to thermal noise whereas the Fokker-Planck and the master equation represent continuity equations for the probability distribution of an observable.

Concerning the thermodynamic interpretation of small systems, classical thermodynamics is inadequate since fluctuations are not taken into account. Moreover, biological systems often operate far away from equilibrium [5]. A consistent interpretation of thermodynamic quantities like heat, work and entropy along a single fluctuating trajectory is provided by stochastic thermodynamics [6–8].

A particularly interesting class of small biological systems are molecular motors, enzymatic complexes that convert chemical energy into mechanical motion. Molecular motors constitute the "machinery of life": They are essential components involved in a variety of biological processes. From the generation of ATP in mitochondria, the transport of organelles inside cells, DNA replication and cell division, the motion of cilia, e.g., in the lung, the propulsion of sperm and bacteria up to the contraction of muscles, all these processes depend on various kinds of molecular motors [9–11]. While most motors like kinesin or myosin consume ATP to gain energy from the hydrolysis reaction, the F_oF_1-ATPase is a special motor that re-synthesizes the hydrolyzed ATP using energy from electrochemical potential gradients across membranes (see Nobel Prize in Chemistry 1997 [12]). Humans convert roughly 40 kg of ATP per day that way [11, 13].

One of the most intriguing properties of molecular motors is their ability to

maintain a stable and efficient performance despite ubiquitous thermal fluctuations. Much scientific attention has been paid to the structure and function of these microscopic machines which attain much larger efficiencies than their macroscopic counterparts [14]. The F_1-ATPase is in principle able to use the full free energy obtained from ATP hydrolysis to rotate attached objects through viscous solvent without notable dissipation in the motor domain itself [15–17]. Kinesin has been found to transport its cargo for roughly hundred steps before detaching from its track [18, 19].

The first motors discovered in 1940s were myosins, followed by dyneins in 1960s, kinesins in 1985 and the F_oF_1-ATPase in the 1990s [9, 20–22]. Since then, experimental and theoretical studies of molecular motors have become a broad and current field of research.

New experimental techniques which allow to investigate a single molecule along a individual trajectories have evolved since the 1990s and are commonly known as single molecule techniques [14, 23–25]. Many of these setups comprise colloidal particles coupled to the motor to serve as probe to visualize the trajectory or to exert forces on the motor under investigation. Those probe particles are often much larger than the motor itself. On the basis of experimental data, theoretical models are designed and properties of the motor are inferred from these experimental setups. In the theoretical analysis of such assays, the motor is usually modeled as a particle hopping on a discrete state space with transitions governed by a master equation [26–31]. Alternatively, the so-called ratchet models combine continuous diffusive spatial motion with stochastic switching between different potentials corresponding to different chemical states [32, 33]. These approaches often comprise only one particle explicitly, representing the motor. The contribution of external forces which in the experiments act on the motor only via the probe are then included in the transition rates [28, 29, 34–40] (or Langevin equation for the spatial coordinate [41, 42]) of the motor particle directly. However, theoretical models that are used to reproduce the experimental observations should comprise at least two (coupled) degrees of freedom, one for the motor and one for the probe particle. Omitting the explicit dynamics of the probe and attributing the experimentally observed features to only the motor yields overly complex motor models with possibly unrealistic thermodynamic properties. In general, it is *a priori* unclear which properties of the motor dynamics and energetics and to what extent they are influenced by the coupling to the probe. Thus, for theoretical modeling as well as interpretation of experimental data it is crucial to consider both the motor and the probe as equal constituents of the setup.

In this thesis, we study theoretically the dynamics and thermodynamics of single molecular motors coupled to a probe particle. We especially focus on the influence of the probe on the motor which affects various properties of the dynamics and

energetics accessible in experiments. In chapter 2, we provide a brief overview of stochastic dynamics, stochastic thermodynamics and experimental and theoretical research concerning molecular motors. Chapter 3 introduces the so-called hybrid model representing a generic motor-probe setup that we will use to investigate several effects caused by the coupling between motor and probe. In chapter 4 we study three different definitions of efficiency for molecular motors using hybrid models with a one-state motor. We apply our model to the F_1-ATPase and compare our results with recent experimental data. We then focus on the velocity autocorrelation function and the response function of the probe as well as on the dwell-time distribution, which can be obtained rather easily in experiments, in chapter 5. We apply three simplified one-state models to obtain analytical results providing insights into the connection between the motor dynamics and the observed velocity autocorrelation of the probe. We compare the analytical results with simulations and experimental data of the F_1-ATPase. The last two chapters address more general aspects concerning generic unicyclic and multicyclic motors. We introduce the network representation of the hybrid models in chapter 6 and show how the presence of the probe affects the net currents in the network Chapter 7 provides a thermodynamically consistent coarse-graining procedure that allows to map hybrid models to effective one-particle models maintaining the correct average currents, local detailed balance conditions and entropy production. A concluding perspective can be found in chapter 8.

Publications

Parts of this thesis involve the following publications:

- "Efficiencies of a molecular motor: A generic hybrid model applied to the F_1-ATPase"
  E. Zimmermann and U. Seifert, New J. Phys. **14**, 103023 (2012)

- "Fine-structured large deviations and the fluctuation theorem: Molecular motors and beyond"
  P. Pietzonka, E. Zimmermann, and U. Seifert, EPL **107**, 20002 (2014)

- "Effective rates from thermodynamically consistent coarse-graining of models for molecular motors with probe particles"
  E. Zimmermann and U. Seifert, Phys. Rev. E **91**, 022709 (2015)

2. Basics

2.1. Stochastic dynamics

Since molecular motors and colloidal particles are mesoscopic objects, thermal fluctuations have a strong impact on their dynamics and energetics. The random motion of such particles immersed in an aqueous solvent is well known as Brownian motion. Since the smaller molecules of the solvent relax much faster than the Brownian particle, the dynamics exhibit a time-scale separation between the dynamics of the fast degrees of freedom and the slower ones. Thus, the random motion of the Brownian particle can be approximated very well by a Markov process [43]. We will restrict the discussion here to one spatial dimension. The random dynamics along a continuous coordinate x can be described by the Langevin equation [44, 45]

$$m\ddot{x} = -\gamma\dot{x} - \partial_x \mathcal{V}(x) + f + \xi(t), \tag{2.1}$$

which is Newton's equation of motion augmented by a random force $\xi(t)$ that the solvent molecules exert on the Brownian particle. The mass of the Brownian particle is denoted by m, γ is the friction coefficient, f a (constant) external driving force and $\mathcal{V}(x)$ a potential or, if the particle has internal degrees of freedom or if the dynamics involves chemical reactions in the solvent, the free energy of system and solvent. If inertial effects are negligible, the Langevin equation in the overdamped limit reads

$$\dot{x} = \left(-\partial_x \mathcal{V}(x) + f\right)/\gamma + \zeta(t) \tag{2.2}$$

with $\zeta(t) = \xi(t)/\gamma$. The random contributions are usually modeled as Gaussian white noise with zero mean and correlations

$$\langle \zeta(t_2)\zeta(t_1)\rangle = 2D\delta(t_2 - t_1). \tag{2.3}$$

In the following, we set Boltzmann's constant $k_\mathrm{B} = 1$ and temperature $T = 1$.

In equilibrium, the Einstein relation $D = 1/\gamma$ relates the diffusion coefficient D of the Brownian particle to its friction coefficient, which is a special case of the fluctuation-dissipation theorem [46]. We will assume that driving the system out of equilibrium does not affect the heat-bath properties of the solvent and $D = 1/\gamma$ remains valid.

A Kramers-Moyal expansion [44] provides the corresponding Fokker-Planck equation for the evolution of the probability distribution $p(x)$

$$\partial_t p(x,t) = -\partial_x\Big((-\partial_x \mathcal{V}(x) + f)p(x,t) - \partial_x p(x,t)\Big)/\gamma \tag{2.4}$$

$$\equiv -\partial_x j(x,t) \tag{2.5}$$

which constitutes a continuity equation for the probability current $j(x,t)$.

On a discrete state space with states labeled by i, the equivalent to the Fokker-Planck equation is given by the master equation [43]

$$\partial_t p_i(t) = \sum_j \left(p_j(t)w_{ji}(t) - p_i(t)w_{ij}(t)\right), \tag{2.6}$$

with transition rates $w_{ij} \geq 0$. The master equation is a balance equation for fluxes into and out of state i involving all other states j linked to i. The directed (net) transition current between two states is denoted by

$$j_{ij}(t) \equiv p_i(t)w_{ij}(t) - p_j(t)w_{ji}(t) = -j_{ji}(t). \tag{2.7}$$

In a stationary state, the left hand sides of Eqs. (2.5, 2.6) vanish. In genuine equilibrium the currents $j(x,t)$ and $j_{ij}(t)$ are zero and the stationary distribution corresponds to the Boltzmann distribution

$$p^{\mathrm{eq}}(x) = \frac{\exp[-\mathcal{V}(y)]}{\int_{-\infty}^{\infty}\exp[-\mathcal{V}(y)]\,\mathrm{d}y} \tag{2.8}$$

or

$$p_i^{\mathrm{eq}} = \frac{\exp[-\mathcal{V}_i]}{\sum_i \exp[-\mathcal{V}_i]}, \tag{2.9}$$

respectively. Hence, from Eqs. (2.7, 2.9) one obtains

$$\frac{p_i^{\mathrm{eq}}w_{ij}}{p_j^{\mathrm{eq}}w_{ji}} = 1 \qquad \text{or} \qquad \frac{p_i^{\mathrm{eq}}}{p_j^{\mathrm{eq}}} = \frac{w_{ji}}{w_{ij}} = \exp[-\Delta\mathcal{V}_{ji}^{\mathrm{eq}}] \tag{2.10}$$

which is known as detailed balance condition [43]. The potential or free-energy difference between the states i, j is denoted by $\Delta\mathcal{V}_{ij} = \mathcal{V}_j - \mathcal{V}_i$. In a nonequilibrium steady state (NESS), there are in general constant nonzero currents. A NESS can be generated by, e.g., external driving forces or, in the case of enzymatic reactions, by constant nonequilibrium concentrations of the involved solvent molecules. The chemical reaction then delivers free energy driving the system out of equilibrium which is incorporated in $\Delta\mathcal{V}_{ij} \neq \Delta\mathcal{V}_{ij}^{\mathrm{eq}}$. For thermodynamic consistency it is mandatory to impose the so-called local detailed balance condition on the transition rates which can additionally include work W_{ij} corresponding to the external driving force [6, 37, 47–52]

$$\frac{w_{ij}}{w_{ji}} = \exp[-\Delta\mathcal{V}_{ij} + W_{ij}]. \tag{2.11}$$

2.2. Stochastic thermodynamics

The solvent molecules surrounding a Brownian particle can be considered as a heat bath in contact with the system of interest, which allows a consistent thermodynamic interpretation [6]. The framework of stochastic thermodynamics then provides an identification of thermodynamic quantities on the level of a single fluctuating trajectory.

Suppose the potential or free energy $\mathcal{V}(x)$ is not affected by the external driving, then the work applied to the system is given by [7, 53]

$$đw = f\,\mathrm{d}x \qquad \text{or} \qquad W_{ij} = f d_{ij} \tag{2.12}$$

for a discrete state space with a spatial separation of d_{ij} between states i, j. Using the first law, $đw = \mathrm{d}E + đq$, the heat can be identified as [6, 51]

$$đq = -\partial_x \mathcal{V}(x)\,\mathrm{d}x + f\,\mathrm{d}x - \mathrm{d}s^{\mathrm{sys}}(x) \tag{2.13}$$

or, using Eq. (2.11),

$$q_{ij} = -\Delta\mathcal{V}_{ij} + f d_{ij} - \Delta s^{\mathrm{sys}}_{ij} = \ln\frac{w_{ij}}{w_{ji}} - \Delta s^{\mathrm{sys}}_{ij}. \tag{2.14}$$

The intrinsic entropy of the system $s^{\mathrm{sys}} = s^{\mathrm{enz}} + s^{\mathrm{sol}}$ originating from fast internal degrees of freedom and chemical reactions in the solvent occurs only if $\mathcal{V}$ is not a bare potential but a free energy. For the first law, one then has to split the internal energy into $E = \mathcal{V} + s^{\mathrm{sys}}$ [6, 51].

The total entropy production of the system and the surrounding solvent consists of the following contributions. First, the entropy change of the solvent $\dot{s}^{\mathrm{med}}$, which is caused by the dissipated heat (2.13, 2.14), second the internal entropy change of the system $\dot{s}^{\mathrm{sys}}$, which accounts for entropy changes of the particle and the solvent due to chemical reactions. Third, the contribution of the stochastic entropy [54]

$$s(t) = -\ln p(x(t), t) \qquad \text{or} \qquad s(t) = -\ln p_{i(t)}(t) \tag{2.15}$$

with $p(x(t), t)$, $p_{i(t),t}$ being the solution of Eqs. (2.5, 2.6), which represents the entropy produced along a trajectory due to changing $p(x, t)$. Hence, the total entropy production reads [54]

$$\dot{s}^{\mathrm{tot}}(t) = \dot{s}^{\mathrm{med}} + \dot{s}^{\mathrm{sys}} + \dot{s}(t) = -\frac{\partial_t p(x,t)}{p(x,t)}\Big|_{x(t)} + \frac{\gamma j(x,t)}{p(x,t)}\Big|_{x(t)}\dot{x} \tag{2.16}$$

for continuous dynamics where we have made use of the probability current defined in Eq. (2.5). On a discrete state space, using Eq. (2.14), the total entropy production rate is given by [6]

$$\dot{s}^{\mathrm{tot}}(t) = -\frac{\partial_t p_i(t)}{p_i(t)}\Big|_{i(t)} + \sum_k \delta(t - \tau_k)\ln\frac{p_{i_k}(\tau_k) w_{i_k j_k}}{p_{j_k}(\tau_k) w_{j_k i_k}}. \tag{2.17}$$

On average, the total entropy production fulfills the second law,

$$\dot{S}^{\mathrm{tot}} \equiv \langle s^{\mathrm{tot}} \rangle = \int \frac{\gamma j^2(x,t)}{p(x,t)}\,\mathrm{d}x \geq 0 \qquad \text{and} \tag{2.18}$$

$$\dot{S}^{\mathrm{tot}} \equiv \langle s^{\mathrm{tot}} \rangle = \frac{1}{2}\sum_{ij}\Big(p_i(t)w_{ij} - p_j(t)w_{ji}\Big)\ln\frac{p_i(t)w_{ij}}{p_j(t)w_{ji}} \geq 0. \tag{2.19}$$

Note that in Eq. (2.19), the average entropy production is positive along each link and hence also for any subgroup of states.

2.3. Molecular motors

2.3.1. General aspects

In this section, we will briefly provide an overview of molecular motors, the various experimental approaches that are used to investigate these nanomachines as well as popular theoretical modeling.

Biological cells are active systems operating in nonequilibrium environment. Many of the processes involved in cellular function are conducted by molecular motors. Molecular motors are enzymatic complexes on the size of a few nanometers that are able to transduce energy available from chemical reactions into mechanical motion. Their field of activity ranges from the synthesis of ATP, providing the energy source for further processes, transport of vesicles and organelles, DNA polymerization, production of proteins up to contraction of muscles and propulsion of flagella [9, 10, 20, 55–57].

Within the cell, molecular motors operate in aqueous solution. Unbalanced concentrations of the nucleotides providing chemical energy release during ATP hydrolysis cause the motor proteins to operate under nonequilibrium conditions, which allows for a rectified motion with non-zero average velocity. Under physiological conditions, the free energy released from the hydrolysis of a single ATP molecule is roughly $20\,k_{\mathrm{B}}T$ [10]. Due to their small size and since they operate at energy scales comparable to the thermal energy of the surrounding solvent, molecular motors are subject to thermal fluctuations. Hence, their dynamics and energetics become stochastic. Moreover, they move in a crowded environment. Surprisingly, molecular motors exhibit a very efficient and robust performance which makes them a very interesting object of research for physical, chemical and biological science. The microscopic details of the energy conversion mechanism of molecular motors have been of scientific interest for quite some time and are still not fully understood [20].

In general, binding or hydrolysis of a nucleotide molecule causes configurational changes in the motor molecule that finally yield rotations of parts of the molecule

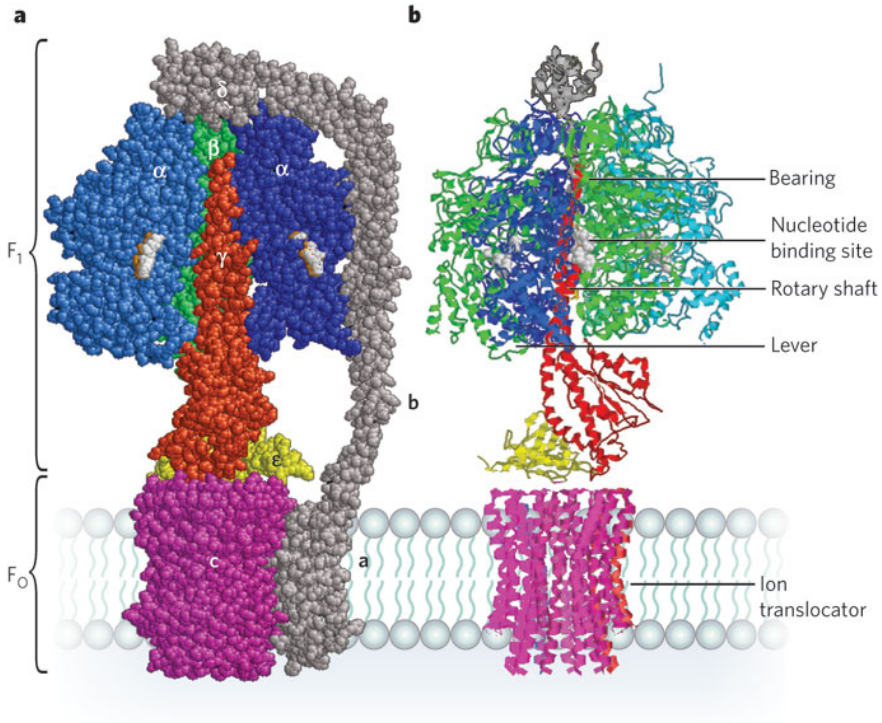

Figure 2.1.: Structural model of the F_oF_1-ATPase [62]. Both the space-filling model (a) and the ribbon model (b) have been constructed on the basis of several partial structures provided by the Protein Data Bank [63]. During proton translocation, the c subunit (purple) of the membrane-embedded F_o rotates and drives the rotation of the asymmetric central γ stalk (red). The rotation of γ induces conformational changes in the α and β subunits of F_1 since the stator (subunits a, b, δ; gray) fixes the orientation of α and β relative to the membrane. Reprinted by permission from Macmillan Publishers Ltd: *Nature*, Ref. [62], ©2009

[58, 59] or a stronger or weaker coupling to the filament [60, 61]. This mechanism allows for directed rotation along the preferred direction or for linear motion along a filament. After releasing the hydrolysis products into the solvent, the chemomechanical cycle is completed and the motor is in its original configurational state yet having advanced a certain distance.

Since we will later apply our theoretical models and compare simulation results with experimental data of the F_1-ATPase and the kinesin motor, we will briefly present these motors in more detail.

Oxidative phosphorylation is the process that provides energy on the cellular level from oxidation of nutrients. Several protein complexes are involved including the F_oF_1-ATPase which finally synthesizes ATP. It can be found in the mitochondria of human and animal cells, in the thylakoid membranes of chloroplasts and

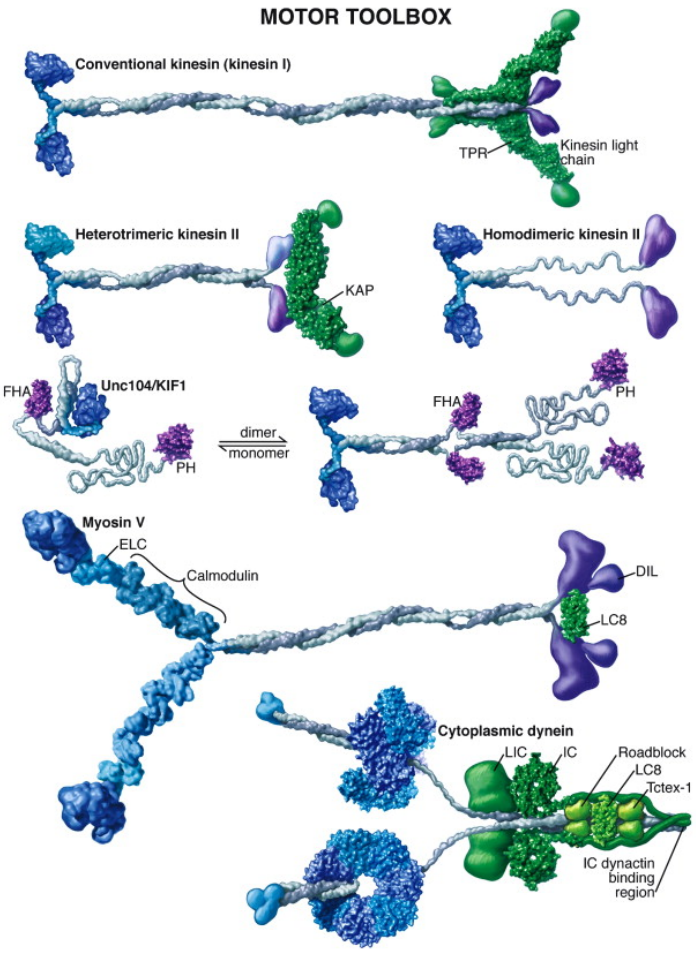

Figure 2.2: Structural models of the cytoskeleton motors kinesin, myosin and dynein [64]. The catalytic domains involving ATP hydrolysis and binding and unbinding from the filaments are colored blue whereas the tail domains that attach to the cargo are shown in purple. The models are based on the crystal structure of the respective motor when available. Reprinted from Ref. [64], ©2003, with permission from Elsevier.

in bacterial plasma membranes. It consists of two parts, the membrane-embedded F_o that uses a proton gradient to rotate a central stalk connected to the F_1 part inside the mitochondrion or bacterium, see Fig. 2.1. The rotation of the asymmetric stalk induces conformational changes in the subunits of the F_1 part which facilitates binding of ADP and P and synthesis of an ATP molecule [22, 62, 65–70]. This mechanism works also in reverse [71]. Both parts can be separated and studied in detail [15, 16, 41, 58, 66, 72–77]. The particularly well studied F_1-motor consists of three α and three β subunits arranged around the central γ stalk [78, 79]. Forced ATP synthesis has not only been observed within the cell [80] but also in experiments exerting torque on the stalk [81]. In the absence of an external torque and in the presence of ATP in excess, the F_1-ATPase prefers to run in the reverse direction hydrolyzing ATP. Binding and hydrolysis of an ATP molecule at a β subunit drives a rotation of the γ shaft of 120° [73] which has been observed to consist of two substeps of 90° (80°) and 30° (40°) [74]. The

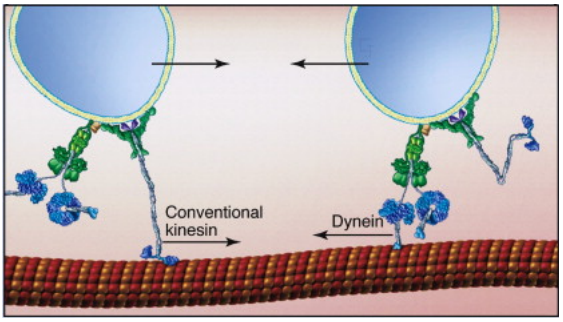

Figure 2.3: Kinesin and dynein transporting cargo along a microtubule [64]. Bidirectional transport involving different motor species is useful, e.g., to overcome obstacles on the microtubule. Reprinted from Ref. [64], ©2003, with permission from Elsevier.

structural composition [82, 83] as well as the chemomechanical reaction pathway of the F_1-ATPase has been studied in detail [84–90]. These studies suggest that for the F_1-ATPase chemical and mechanical processes are tightly coupled due to a single chemomechanical cycle that relates chemical energy input to mechanical output.

The ATP that has been generated by the F_oF_1-ATPase is used by cytoskeleton motors like kinesin, dynein and myosin [61, 64]. Structural models of several cytoskeleton motors are shown in Fig. 2.2. Cytoskeletal motor proteins move linearly along cytoskeletal filaments that serve as a track. Myosin moves along actin filaments and is well known for causing muscle contraction [91, 92] while dynein moves towards the minus end of microtubules and occurs in spindle formation, chromosome segregation and transport of organelles [93].

Kinesin is a dimeric motor that moves along microtubules in the plus direction [9, 93]. It steps in a hand-over-hand fashion [94] with a step size of 8 nm [95] and is involved mainly in transport of organelles and vesicles. It is a highly processive motor taking many steps before detaching from the microtubule [18, 19]. ATP hydrolysis is used to weaken the coupling of one "head" with the filament [60, 61, 96]. Thus, the (rear) head can unbind and diffuse forward searching the next binding site. Kinesin has been studied extensively both experimentally [18, 19, 95–99] and theoretically [28, 49, 100–103]. It was found that kinesin is able to walk backwards hydrolyzing ATP [104]. Hence, these studies suggest that several chemomechanical cycles are involved in the energy transduction process [28, 103, 105].

In addition to research on single motor molecules transporting cargo, various experimental and theoretical studies have focused on several coupled motors or several teams of motors coupled to the same cargo as depicted in Fig. 2.3. Such collective transport seems to be the most realistic view of cargo translocation in cells [106–112].

2.3.2. Experimental techniques

Since the early 1990, in vitro experiments with single molecules have experienced broad application in the field of molecular motors. The fact that molecular motors are objects of only $\sim$ 10 nm in size but can take more than 100 steps per second [74, 99] poses challenges to experimental methods. Techniques that have been applied successfully to molecular motors comprise fluorescence labeling and spectroscopy as well as the investigation of large attached probe particles suitable for optical trap and magnetic tweezer experiments [14, 20, 24, 25].

Fluorescent dyes can be attached directly to the motor in order to observe its motion [19, 113]. Using an optical microscope, the resolution is limited by the diffraction limit ($\sim$ 200 nm) which is much larger than the motor itself ($\sim$ 10 nm). Improved spatial resolution below the diffraction limit can be obtained using a variety of methods known as super-resolution microscopy (see Nobel Prize in Chemistry 2014 [114]) [24, 115]. Fluorescence imaging provided the insight that kinesin moves hand-over-hand [94]. Förster resonance energy transfer (FRET) can be used to detect conformational changes during the catalytic cycles [24, 116, 117].

Another group of very popular experimental methods involve probe particles of the size of micrometers that are attached to the motor. The probe particles are linked via biotin and streptavidin molecules to the motors which are assumed to constitute a relatively soft linker. Concerning kinesin, the probe takes over the role of the transported vesicle, whereas in the case of the F_1-ATPase, the probe is attached at the rotating central stalk. The applied probe particles range from actin filaments [73] over dimeric and monomeric polystyrene beads [15, 77, 98, 99, 118], magnetic beads [15, 119] down to gold colloids of the size of only 40 nm [74, 87, 120, 121].

The advantages of these methods are on the one hand that at least the larger probes can be observed using conventional microscopy and, on the other hand, that such probes allow to exert forces on the motors. Many optical and magnetic tweezer experiments have been performed using such motor-probe setups [15, 73, 77, 81, 99, 122]. These techniques are of great importance since they allow to gain insights not only in the dynamics but also in the thermodynamics and energy transduction mechanism of molecular motors.

Despite their relevance, motor-probe setups also have shortcomings. Literally speaking, in these assays one cannot observe the motion of the motor directly but rather has to infer its properties from analyzing the trajectory of the probe particle. Since the probe is often almost an order of magnitude larger, it often constitutes a considerable hindrance to the motor and can severely influence its dynamics (and thermodynamics). Inferring properties of the motor protein requires to consider the interaction effects that depend on the linkage between motor protein and probe [16, 101, 108, 110, 123–128].

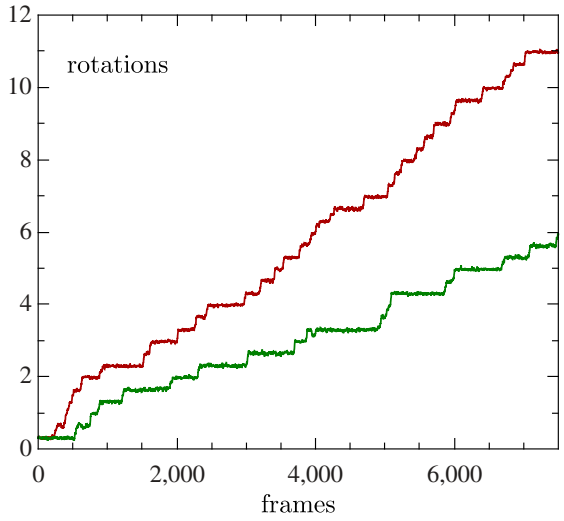

Figure 2.4: Trajectory of a motor-probe setup with the F_1-ATPase motor as used in [15]. Concentrations: $c_T = 0.4\mu M$, $c_D = 0.4\mu M$, $c_{P_i} = 1mM$. Experimental data kindly provided by S. Toyabe.

A typical experimental trajectory of a motor-probe setup is shown in Fig. 2.4. The trajectory of the probe shows a distinct staircase form indicating that the motor advances with fast discrete steps.

2.3.3. Theoretical modeling

Operating in aqueous solution, the dynamics and energetics of molecular motors are subject to thermal fluctuations. Hence, a stochastic dynamics approach is best suited to model molecular motors.

Molecular motors are complex proteins that contain a large number of microscopic degrees of freedom. In order to simplify the description, one usually focuses on a set of relevant mesoscopic states x of the motor like, e.g., ATP bound to the motor, hydrolysis products bound or nothing bound to the motor. Equilibration among the microstates corresponding to the same mesostate has to be fast compared to transitions between the mesostates. Nevertheless, the microscopic degrees of freedom can influence the latter processes and should not be ignored [6, 51]. The microstates of the motor and its surrounding solvent, collectively denoted by χ, have a configurational energy $\Phi(\chi)$ which includes interactions between motor and solvent. The influence of the fast degrees of freedom on the mesoscopic dynamics is then captured in the notion of a free-energy surface acting on x which is formally obtained by summing over all χ belonging to the specific x [6, 51, 129],

$$F(x) = -\ln \sum_{\chi|x} \exp[-\Phi(\chi)]. \tag{2.20}$$

Hence, investigation of the dynamics and thermodynamics of molecular motors requires the notion of a free energy instead of a potential as presented in the

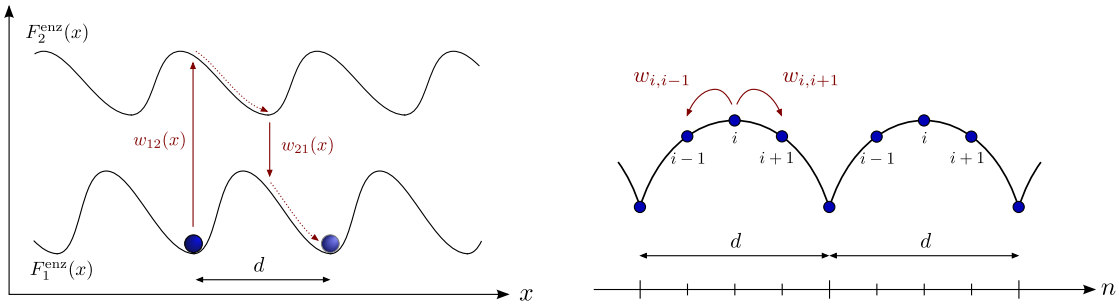

Figure 2.5.: Schematic representation of a ratchet model (left) and a discrete state model (right), adapted from [20]. The red arrows indicate the mechanism of directed motion in the ratchet or the network. The ratchet potentials $F_1^{\mathrm{enz}}(x)$ and $F_2^{\mathrm{enz}}(x)$ have a periodicity interval of length d. In the discrete state model, each transition involves a mechanical step. Within one cycle of length d the motor jumps between several internal states with rates $w_{i,i+1}$, $w_{i,i-1}$.

previous section.

The dynamics of x subject to the free-energy surface $F(x)$ can now be described using Langevin, Fokker-Planck or master equations [20, 26, 32, 57, 129, 130]. We will briefly discuss two classes of models that have become very popular in modeling molecular motors and are sketched in Fig. 2.5.

The so called ratchet models combine continuous diffusive spatial motion with stochastic switching between different spatially periodic potentials $F_i^{\mathrm{enz}}(x) \equiv F_i(x) - F_i^{\mathrm{sol}}$ corresponding to different chemical states i and representing only enzymatic conformations [32, 33, 41, 42]. The dynamics of the system is described by a set of Fokker-Planck equations with source terms

$$\begin{aligned}\partial_t p_i(x,t) = &- \partial_x((-\partial_x F_i^{\mathrm{enz}}(x) + f)p_i(x,t) - \partial_x p_i(x,t))/\gamma \\ &+ \sum_j \left(p_j(t)w_{ji}(x) - p_i(t)w_{ij}(x)\right). \end{aligned} \tag{2.21}$$

Directed motion can be generated when the system is not in equilibrium and the switching rates w_{ij} do not obey detailed balance. The energy input $\Delta F_{ij}^{\mathrm{sol}}$ is then used to switch the potentials in such a way that the motor diffuses on average in one direction. A simple ratchet model with two chemical states is shown in Fig. 2.5. Ratchet models need the explicit form of the free-energy landscape which is not known in most cases. They are also not practical for motors with many chemical or internal states i.

Discrete state stochastic models constitute a different approach [26–28, 28–31, 34–40]. The state space is represented by a network where the nodes are the states and the edges correspond to the transition rates. The dynamics on the set of discrete states is governed by a master equation (2.6). Each state represents

an internal state of the motor and is assigned a free energy F_i^{enz}. Transitions between two states occur with transition rates w_{ij} where microscopic reversibility implies $w_{ij} \neq 0 \Leftrightarrow w_{ji} \neq 0$. Transitions between the states i can be purely chemical involving binding or release of nucleotides, purely conformational, purely mechanical, or any combination thereof. Thermodynamic consistency requires the rates to obey a LDB condition [6, 20]. If a transition involves binding or release of nucleotides, the free-energy change appearing in the LDB condition (2.11) has a contribution from the solvent, i.e., $\Delta\mathcal{V}_{ij} = \Delta F_{ij} = \Delta F_{ij}^{\mathrm{enz}} + \Delta F_{ij}^{\mathrm{sol}}$.

Such network models with instantaneous transitions between states provide a good approximation of the motor dynamics since experimental data indicate that the individual steps indeed occur on very small timescales. If the network comprises a single cycle, the motor is called unicyclic. In general, motors with several states typically contain several chemomechanical cycles and are called multicyclic. The chemical and mechanical steps can be tightly or loosely coupled [131]. Tight mechanochemical coupling requires that every cycle of the motor comprises the chemical (input) as well as the mechanical (output) transitions. All unicyclic motors are automatically tightly coupled. Loose mechanochemical coupling implies the presence of cycles that contain typically only transitions consuming chemical energy but do not contribute to mechanical force generation. Such cycles clearly reduce the energy-transduction efficiency of the motor and are called idle cycles [38, 132].

In principle, ratchet models correspond to the continuum limit of a special class of discrete state hopping models. Discretizing the the spatial coordinate of the ratchet yields a discrete model where each state is linked to neighboring states via chemical-conformational transitions (the original switching of the potential) and mechanical-conformational transitions (the original diffusion process).

The contribution of external forces which in the experiments act on the motor only via the probe are often included in the transition rates [28, 29, 34–40] or Langevin equation for the spatial coordinate [41, 42] of the motor particle directly.

A theoretical model combining diffusive motion and a network description is developed in [133]. Here, the states of the motor are represented by the nodes of a network but the motor evolves diffusingly along the edges rather than jumping instantaneously.

In contrast to these rather coarse models, molecular motors are also investigated using molecular dynamics simulations based on the known structure of the individual proteins that build up the motor complex [90, 134].

3. Modeling of motor and probe dynamics

3.1. Introduction

In this chapter we will set up the models that will be used to investigate various aspects of the coupling between a molecular motor and its attached probe particle. In the following, we will denote models comprising motor and probe particles as "hybrid models". Such models consisting of one degree of freedom hopping on a discrete state space representing the motor coupled to a continuously moving degree of freedom representing the probe are discussed in [16, 101, 108–110, 128, 135, 136].

3.2. Motors with a single internal state

3.2.1. Single-molecule dynamics

Considering experimental realizations of motor-probe systems as mentioned in section 2.3.2, the observed trajectories exhibit a staircase form. Thus, it is convenient to model the transitions of the motor protein as sudden jumps that instantaneously translocate the motor by its specific step size d in forward or backward direction. According to the network models, a motor with only one internal state will be modeled as a particle that jumps between discrete states $n(t)$ separated by d.

The noisy appearance of the experimental trajectories during the plateaus between two steps can be attributed to the diffusion of the probe particle around the actual motor position. The dynamics of the probe particle is assumed to be a continuous diffusion and drift along a one-dimensional coordinate $x(t)$. Since the commonly used probe particles range from gold colloids with a diameter of 40 nm to polystyrene beads or actin filaments almost on the order of µm, the dynamics of the probe particle is described by an overdamped Langevin equation.

The system is characterized by the pair of variables (n,x) and is "bipartite" in these variables since transitions do not happen in both variables at the same time. Both constituents are coupled via some kind of elastic linker with potential energy $V(n-x)$ as shown in Fig. 3.1.

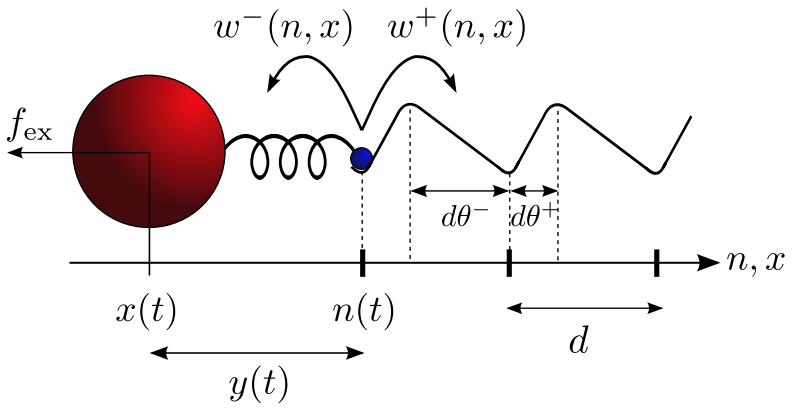

Figure 3.1.: Schematic representation of a motor-bead model comprising a one-state motor (blue) attached via an elastic linker to the probe particle (red) [137]. An external force f_{ex} is applied to the bead. The transition rates of the motor are denoted by $w^+(n,x)$ and $w^-(n,x)$. The load sharing factors θ^+ and θ^- indicate the position of an underlying unresolved potential barrier relative to the minimum of the free-energy landscape of the motor. ©2015 American Physical Society.

The Langevin equation governing the dynamics of the probe reads

$$\dot{x}(t) = \left(-\partial_x V(n-x) - f_{\mathrm{ex}}\right)/\gamma + \zeta(t), \tag{3.1}$$

with friction coefficient γ and thermal noise $\zeta(t)$ with correlations $\langle\zeta(t_2)\zeta(t_1)\rangle = 2\delta(t_2-t_1)/\gamma$. The constant external force f_{ex} acting on the probe can be applied using, e.g., optical traps or tweezers.

The transition rates of the motor fulfill a local detailed balance condition

$$\frac{w^+(n,x)}{w^-(n+d,x)} = \exp[\Delta\mu - V(n+d-x) + V(n-x)]. \tag{3.2}$$

The free-energy change of the solvent $\Delta\mu \equiv \mu_{\mathrm{T}} - \mu_{\mathrm{D}} - \mu_{\mathrm{P}}$ with $\mu_i = \mu_i^{\mathrm{eq}} + \ln(c_i/c_i^{\mathrm{eq}})$ and nucleotide concentrations c_i is associated with ATP turnover. In the one-state model, binding of ATP (ADP and $\mathrm{P_i}$), hydrolysis (synthesis) and release of the products all occurs within the forward (backward) jump. The free energy of the motor does not change in the one-state model. Implementing mass action law kinetics and the concept of a barrier in the potential of mean force for the unresolved chemical steps, the individual rates become

$$w^+(n,x) = w_0 \exp[\mu^+ - V(n+d\theta_+ - x) + V(n-x)], \tag{3.3}$$
$$w^-(n,x) = w_0 \exp[\mu^- - V(n-d\theta_- - x) + V(n-x)]. \tag{3.4}$$

The load-sharing factors θ^+ and θ^- satisfy $\theta^+ + \theta^- = 1$ and $\mu^+ = \mu_{\mathrm{T}}$, $\mu^- = \mu_{\mathrm{D}} + \mu_{\mathrm{P}}$. We assume an exponential dependence of the transition rates on the potential

difference of the linker according to Kramers's theory, see also [138]. The attempt frequency is denoted by w_0.

3.2.2. Fokker-Planck equation

The transition rates, as well as the potential of the linker, depend on the instantaneous distance

$$y(t) \equiv n(t) - x(t) \tag{3.5}$$

between motor and probe. The corresponding probability density $p(y,t)$ obeys the Fokker-Planck-type equation

$$\begin{aligned}\partial_t p(y) = \partial_y \Big(&(\partial_y V(y) - f_{\text{ex}})\; p(y) + \partial_y p(y) \Big)/\gamma \\ &+ p(y-d)\, w^+(y-d) + p(y+d)\, w^-(y+d) \\ &- p(y) \Big(w^+(y) + w^-(y) \Big) .\end{aligned} \tag{3.6}$$

For constant nucleotide concentrations that deviate from their equilibrium ratio, the system reaches a nonequilibrium stationary state (NESS) with constant average velocity

$$\begin{aligned} v &\equiv d \int_{-\infty}^{\infty} p^s(y)(w^+(y) - w^-(y))\, \mathrm{d}y \\ &= \int_{-\infty}^{\infty} p^s(y)\, (\partial_y V(y) - f_{\text{ex}})\, /\gamma \, \mathrm{d}y = \langle \dot{x} \rangle \end{aligned} \tag{3.7}$$

and stationary distribution $p^s(y)$.

Simulations of this model using a Gillespie algorithm as described in the Appendix A generates trajectories as shown in Fig. 3.2 in the top row. All parameter sets correspond to an excess of ATP over ADP and P_i which is indicated by a curved arrow in the sketches at the bottom. A positive $\Delta\mu$ yields a positive average velocity except for the second panel where the external force is larger than $\Delta\mu/d$. The center row shows the corresponding $p^s(y)$. The stationary distribution exhibits a shoulder representing the configurations right after a jump of the motor, when the probe has not relaxed yet. The shoulder is most pronounced for the largest $\Delta\mu$ (fourth panel) and almost absent when the probe is very small and relaxes fast (third panel).

3.3. Motors with multiple internal states

3.3.1. Single-molecule dynamics

In this section, we will generalize the model taking into account several different internal states of the motor labeled by i. The motor states represent the nodes

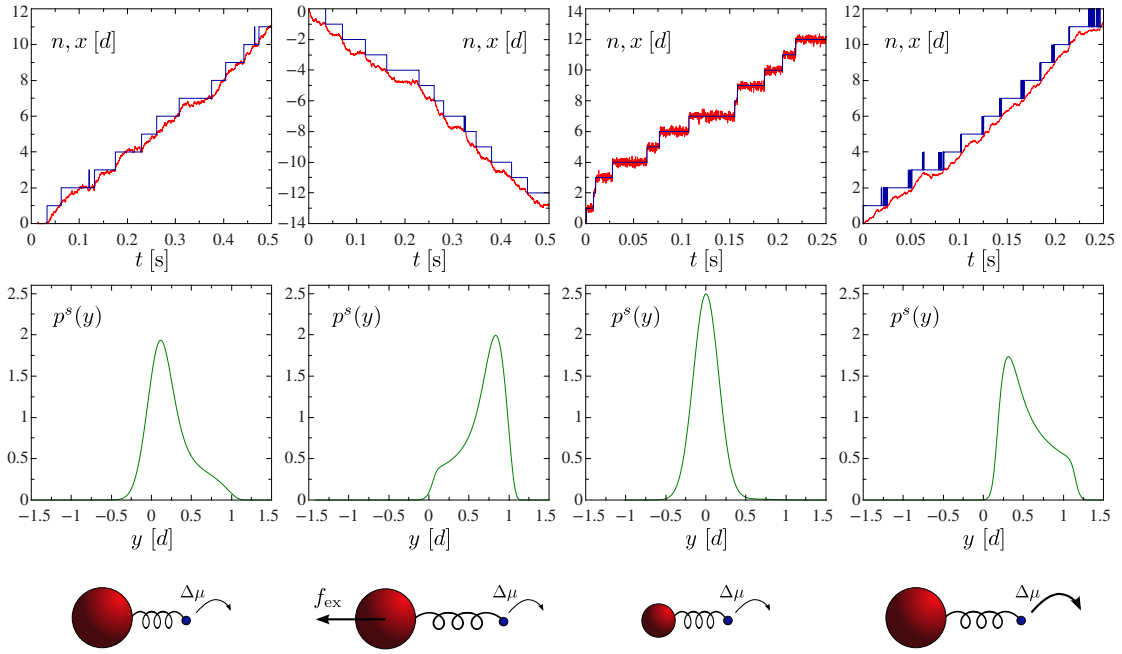

Figure 3.2.: Top: Trajectories of a one-state model for the F_1-ATPase for several parameter sets obtained from simulations. The trajectory of the motor is shown in blue, the one of the probe in red. Center: Stationary distributions $p^s(y)$ corresponding to the trajectories of the top row. Bottom: Sketches of the typical configurations of the motor-probe complex for the corresponding parameter sets. Parameters: $\kappa = 40d^{-2}$, $\theta^+ = 0.1$, $w_0 \exp[\mu_T^{eq}]/c_T^{eq} = 3 \times 10^7$ $(\mathrm{Ms})^{-1}$, $\gamma = 0.5\,\mathrm{s}/d^2$, $f_{ex} = 0$, $c_T = c_D = 2\mu\mathrm{M}$, $c_P = 1\mathrm{mM}$ (far left); $\gamma = 0.5\,\mathrm{s}/d^2$, $f_{ex} = 40\,d^{-1}$, $c_T = c_D = 2\mu\mathrm{M}$, $c_P = 1\mathrm{mM}$ (left); $\gamma = 0.005\,\mathrm{s}/d^2$, $f_{ex} = 0$, $c_T = c_D = 2\mu\mathrm{M}$, $c_P = 1\mathrm{mM}$ (right); $\gamma = 0.5\,\mathrm{s}/d^2$, $f_{ex} = 0$, $c_T = 1\mathrm{mM}$, $c_D = 2\mu\mathrm{M}$, $c_P = 1\mathrm{mM}$ (far right).

and the transitions the edges of a network. Transitions between the motor states i and j change the free energy by

$$\Delta F_{ij}^{\alpha} \equiv \Delta F_{ij}^{\mathrm{enz}} - \Delta\mu_{ij}^{\alpha} \tag{3.8}$$

where $\Delta F_{ij}^{\mathrm{enz}} = F_j^{\mathrm{enz}} - F_i^{\mathrm{enz}}$ is the free-energy difference of the internal states of the motor and $\Delta\mu_{ij}^{\alpha} = -\Delta\mu_{ji}^{\alpha}$ is the free-energy change of the solvent. Depending on the transition, $\Delta\mu_{ij}^{\alpha}$ is given by μ_T, μ_D, μ_P or any combination thereof or 0. Transitions may also advance the motor a distance $d_{ij}^{\alpha} = -d_{ji}^{\alpha}$. Since we allow for several transitions connecting two states, we assign an additional index α to the transitions indicating which link between i and j is used.

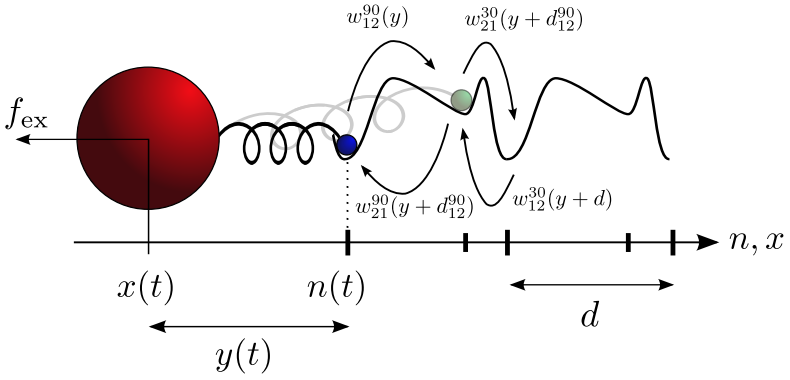

Figure 3.3.: Schematic representation of a motor-bead model for the F_1-ATPase with two internal states of the motor, 1 (blue) and 2 (green) [137]. Transition between states 1 to 2 corresponding to the 90° (30°) substep are labeled with superscript 90 (30). The transition rates are chosen accordingly to Eqs. (3.10, 3.11) with $\phi_{ij}^{\alpha}(y) \equiv 1$. ©2015 American Physical Society.

The transition rates of the motor obey the LDB condition

$$\frac{w_{ij}^{\alpha}(y)}{w_{ji}^{\alpha}(y+d_{ij}^{\alpha})} = \exp[-\Delta F_{ij}^{\alpha} - V(y+d_{ij}^{\alpha}) + V(y)]. \tag{3.9}$$

For multistate motors, Kramers-type transition rates like Eqs. (3.3, 3.4) can be constructed yielding

$$w_{ij}^{\alpha}(y) = k_{ij}^{\alpha}\phi_{ij}^{\alpha}(y)\exp[\mu_{ij}^{\alpha,+} - V(y+d_{ij}^{\alpha}\theta_{ij}^{\alpha,+}) + V(y)], \tag{3.10}$$
$$w_{ji}^{\alpha}(y) = k_{ji}^{\alpha}\phi_{ij}^{\alpha}(y)\exp[\mu_{ij}^{\alpha,-} - V(y-d_{ij}^{\alpha}\theta_{ij}^{\alpha,-}) + V(y)], \tag{3.11}$$

with $\mu_{ij}^{\alpha,+} - \mu_{ij}^{\alpha,-} = \Delta\mu_{ij}^{\alpha}$ and $k_{ij}^{\alpha}/k_{ji}^{\alpha} = \exp[-F_j^{\mathrm{enz}} + F_i^{\mathrm{enz}}]$. The change of chemical free energy $\Delta\mu_{ij}^{\alpha}$ is split into $\mu_{ij}^{\alpha,+}$ and $\mu_{ij}^{\alpha,-}$ indicating that both directions of the transition can involve binding and release of the chemical species that account for $\Delta\mu_{ij}^{\alpha}$. The free-energy change arising from changing the motor state, $F_j^{\mathrm{enz}} - F_i^{\mathrm{enz}}$, is incorporated in the attempt frequencies k_{ij}^{α} of the corresponding states. The function $\phi_{ij}^{\alpha}(y)$ accounts for a possible y-dependence of pure chemical or conformational rates with $d_{ij}^{\alpha} = 0$. Note that $\phi_{ij}^{\alpha}(y)$ has to be chosen such that its contributions cancel in the local detailed balance condition.

An example for a motor with two internal states that is linked to a probe particle is shown in Fig. 3.3. This system represents a motor-probe model of the F_1-ATPase that takes into account the 90° and 30° substep that was observed in [74].

3.3.2. Fokker-Planck equation

The Fokker-Planck-type equation for multistate models is given by

$$\partial_t p_i(y) = \partial_y \left(\left(\partial_y V(y) - f_{\mathrm{ex}} \right) p_i(y) + \partial_y p_i(y) \right) / \gamma + \sum_{j,\alpha} \left(p_j(y + d_{ij}^{\alpha}) w_{ji}^{\alpha}(y + d_{ij}^{\alpha}) - p_i(y) w_{ij}^{\alpha}(y) \right). \tag{3.12}$$

Average quantities in the NESS like the velocity can be obtained by summing over i, j, α and integrating over y,

$$v = \sum_{i,j,\alpha} \int_{-\infty}^{\infty} p_i^s(y) w_{ij}^{\alpha}(y) d_{ij}^{\alpha} \, \mathrm{d}y \tag{3.13}$$

$$= \sum_{i,j,\alpha} \int_{-\infty}^{\infty} p_i^s(y) (\partial_y V(y) - f_{\mathrm{ex}}) / \gamma \, \mathrm{d}y. \tag{3.14}$$

A trajectory generated using the model in Fig. 3.3 is shown in Fig. 3.4. The step length of the motor is divided in two substeps of length $0.75d$ and $0.25d$. For the parameters chosen here, the substeps are not visible in the trajectory of the probe. The right panel shows the stationary distribution for each state. The overall probability to be in state 1 is much larger than the probability for state 2 since for the chosen parameters, the rate-limiting process is the transition from 1 to 2 via the $0.75d$ step. Compared to the one-step model in the previous section, the

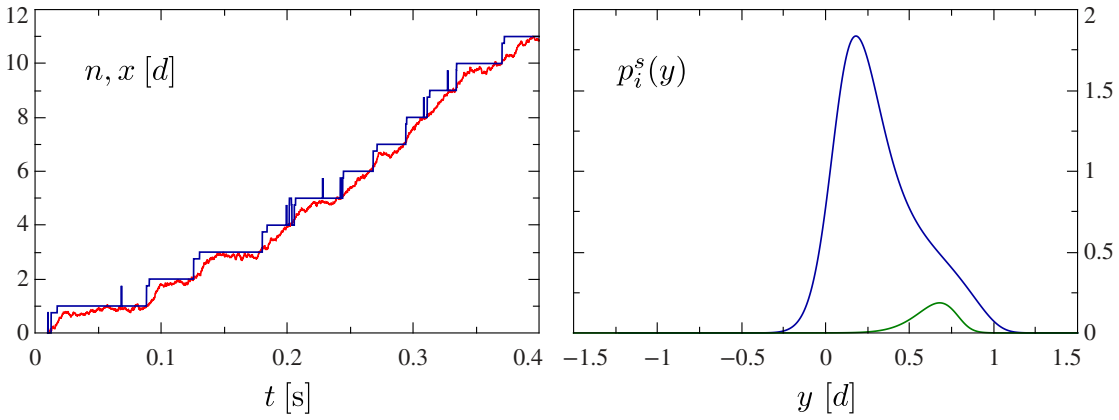

Figure 3.4.: Left: Trajectory of the two-state motor from Fig. 3.3 (blue) and the attached probe particle (red). Left: Stationary distribution for each of the two motor states. The blue curve corresponds to motor state 1, the green one to state 2. Parameters: $\gamma = 0.5\mathrm{s}/d^2$, $\kappa = 40 d^{-2}$, $c_{\mathrm{T}} = 10\mu\mathrm{M}$, $c_{\mathrm{D}} = 2\mu\mathrm{M}$, $c_{\mathrm{P}} = 1\mathrm{mM}$, $\theta_{90,30}^{+} = 0.1$, $k_{12}^{90} \exp[\mu_{\mathrm{T}}^{\mathrm{eq}}]/c_{\mathrm{T}}^{\mathrm{eq}} = 3 \times 10^7 (\mathrm{Ms})^{-1}$, $k_{21}^{90} \exp[\mu_D^{\mathrm{eq}}]/c_{\mathrm{D}}^{\mathrm{eq}} = 3667.5 (\mathrm{Ms})^{-1}$, $k_{21}^{30} = 1000\mathrm{s}^{-1}$, $k_{12}^{30} \exp[\mu_P^{\mathrm{eq}}]/c_{\mathrm{P}}^{\mathrm{eq}} = 40 (\mathrm{Ms})^{-1}$.

shoulder of $p_1^s(y)$ is less pronounced since the step size is smaller and configurations with an elongated linker right after a forward jump by $0.75d$ contribute to $p_2^s(y)$.

4. Efficiencies of molecular motors with probe particles

4.1. Introduction

The operation of molecular motors constitutes a transduction from chemical to mechanical energy. Hence, a quantity of general interest is the efficiency of such stochastic isothermal machines [38, 132, 139–141]. For motor proteins, different kinds of efficiencies can be defined depending on whether one focuses on the work against an external force, i.e., thermodynamic efficiency or whether work against viscous friction is also taken into account like in the Stokes or generalized efficiency [142–147].

In this chapter, we apply the hybrid model with a one-state motor as introduced in section 3.2 to investigate different kinds of efficiencies used previously to describe the energetics of molecular motors. In particular, we compare our results quantitatively to recent experiments of the rotary motor protein F_1–ATPase [15, 77, 119, 148]. Therefore we assume a harmonic potential $V(y) = \kappa y^2/2$ for the linker motivated also by experimental observations [138].

Previous theoretical modeling of the F_1-ATPase using a discrete state model as well as a ratchet model assuming the probe to stick directly at the motor has especially focused on the dependence of the rotational behavior on friction, external forces, nucleotide concentrations and temperature as well as on chemical and thermodynamic efficiency and the fluctuation theorem [41, 76]. Experimental observations of the F_1-ATPase in the hydrolysis direction include the measurements of different kinds of efficiencies. The Stokes efficiency, a Stokes efficiency confined to single jumping events and the thermodynamic efficiency, especially at stall conditions, have been investigated [77, 149, 150]. These experiments led to values for the Stokes efficiency and the thermodynamic efficiency of almost 1 suggesting that the F_1-ATPase can use almost the complete chemical energy either to drive the probe through a viscous medium or to perform work against an external force. Recently, a measure of the efficiency that takes explicitly care of fluctuations was introduced [15]. The definition of efficiency used there also provided values close to 1 for the examined parameters. Our analysis will show that the latter efficiency can easily reach values larger than 1. Most of the results presented in this chapter

have been published in [16].

4.2. Energetics and definitions of efficiency

4.2.1. First law: Single trajectory

Following the concept of stochastic thermodynamics [53, 151] one can assign a first law on the level of a single trajectory. If the probe moves a small distance Δx, the first law becomes

$$\Delta q_{\mathrm{P}} = (-\frac{\partial V}{\partial x} - f_{\mathrm{ex}})\Delta x = (\kappa y - f_{\mathrm{ex}})\Delta x \tag{4.1}$$

where Δq_{P} is the heat dissipated by the probe, $f_{\mathrm{ex}}\Delta x$ is the work against the external force and $(\partial_x V)\Delta x$ the change of the internal energy of the spring due to the motion of only the probe. A jump of the motor protein gives rise to a first law in the form of [51]

$$\begin{aligned} 0 =& \Delta V + \Delta E^{\mathrm{sol}} + \Delta q_{\mathrm{M}} \\ =& \Delta V - \Delta\mu + \Delta s^{\mathrm{sol}} + \Delta q_{\mathrm{M}} \end{aligned} \tag{4.2}$$

without a contribution of the internal energy of the motor as its internal energy does not change in the one–state model. The change of the internal energy of the spring is given by

$$\Delta V \equiv V(n \pm d, x) - V(n, x) \tag{4.3}$$

where the sign depends on the the direction of the jump. Due to ATP turnover, the internal energy of the solution changes by $\Delta E^{\mathrm{sol}} = -\Delta\mu + \Delta s^{\mathrm{sol}}$, where Δs^{sol} is the change of the entropy of the solution. The heat dissipated by the motor protein in this transition is denoted by Δq_{M}.

4.2.2. First law: Ensemble average

On average, the chemical energy gained from ATP consumption that involves changes of the entropy of the solvent will be dissipated as heat Q in the environment and/or is delivered as work against the external force. Under NESS conditions, which we will consider in this chapter, the internal energy of the spring is constant on average. Taking the average rates of (4.1) and (4.2) and summing the two contributions, this first–law condition can be expressed as

$$\dot{\Delta\mu} = \dot{Q}_{\mathrm{P}} + \dot{Q}_{\mathrm{M}} + \dot{S}^{\mathrm{sol}} + f_{\mathrm{ex}} v \tag{4.4}$$

where the dot denotes a rate and

$$\dot{\Delta\mu} \equiv -\langle \dot{F}^{\mathrm{sol}} \rangle = \Delta\mu v/d \tag{4.5}$$

is the rate of free-energy consumption. The rate of dissipated heat $\dot{Q} = \dot{Q}_{\mathrm{P}} + \dot{Q}_{\mathrm{M}}$ has two contributions. First, the heat flow through the motor protein is given by

$$\dot{Q}_{\mathrm{M}} \equiv \langle \dot{q}_{\mathrm{M}} \rangle = \dot{\Delta\mu} - \dot{V}_n - \dot{S}^{\mathrm{sol}}, \tag{4.6}$$

representing the fact that while jumping, the motor protein uses free energy from the hydrolysis to load the spring which corresponds to a change of the internal energy of the spring $\dot{V}_n$ with

$$\dot{V}_n \equiv \int_{-\infty}^{\infty} p^s(y)[w^+(y)(V(y+d) - V(y)) + w^-(y)(V(y-d) - V(y))]\,\mathrm{d}y \tag{4.7}$$

$$= \frac{\kappa d^2}{2}\langle w^+(y) + w^-(y)\rangle + \kappa d\langle y(w^+(y) - w^-(y))\rangle. \tag{4.8}$$

The energy thus stored in the spring is then dissipated by the probe whose heat flow is given by

$$\dot{Q}_{\mathrm{P}} \equiv \langle \dot{q}_{\mathrm{P}} \rangle = \langle (\kappa y - f_{\mathrm{ex}})\nu(y) \rangle \tag{4.9}$$

where

$$\nu(y) \equiv ((\kappa y - f_{\mathrm{ex}}) + \partial_y \ln p^s(y))/\gamma. \tag{4.10}$$

is the local mean velocity of the probe for a given y [152, 153] which corresponds to the current arising from the motion of only the probe in (3.6).

4.2.3. Three different efficiencies

We will now focus on three different definitions of efficiency that have been proposed for motor proteins.

In the absence of an external force ($f_{\mathrm{ex}} = 0$), one can compare the energy that the motor protein transfers to the spring, $\dot{V}_n$, with its available chemical energy $\dot{\Delta\mu}$. From (4.4) and (4.6) it follows that $\dot{V}_n = \dot{Q}_{\mathrm{P}}$. The ratio of on average dissipated heat through the probe and available free energy

$$\eta_{\mathrm{Q}} \equiv \frac{\dot{Q}_{\mathrm{P}}}{\dot{\Delta\mu}} = \frac{d\kappa\langle y\nu\rangle}{v\Delta\mu} \tag{4.11}$$

was proposed as definition of efficiency [15]. We will see below that η_{Q} is not bounded by 1, as it has been anticipated earlier [143, 154], and therefore we will call it a pseudo efficiency.

A second type of efficiency is the Stokes efficiency,

$$\eta_{\mathrm{S}} \equiv \frac{\gamma v^2}{\dot{\Delta}\mu} = \frac{d\kappa\langle y\rangle}{\Delta\mu}, \tag{4.12}$$

that compares the mean drag force γv the probe feels with the available chemical force. In contrast to η_{Q}, η_{S} is bounded by 1 [143]. If the motor protein exerted a constant force on the probe, the Stokes efficiency would be equal to the pseudo efficiency η_{Q} because in this case the average heat dissipated by the probe is the mean drag force times d.

Finally, in the presence of an external force acting on the probe, the thermodynamic efficiency of the system is the ratio between mechanical work delivered to the external force and available free energy [132, 155]

$$\eta_{\mathrm{T}} \equiv \frac{f_{\mathrm{ex}} v}{\dot{\Delta}\mu} = \frac{f_{\mathrm{ex}} d}{\Delta\mu}. \tag{4.13}$$

For $f_{\mathrm{ex}} \neq 0$, the pseudo efficiency η_{Q} can be defined as

$$\eta_{\mathrm{Q}} = \frac{\dot{Q}_{\mathrm{P}} + f_{\mathrm{ex}} v}{\dot{\Delta}\mu}. \tag{4.14}$$

4.3. Gaussian approximation

4.3.1. Derivation

For a comparison with the simulations and in order to gain more analytical insights, it will be convenient to have a simple approximation for the stationary distribution $p^s(y)$. For a Gaussian probability distribution

$$p^G(y) \equiv \frac{1}{\sqrt{2\pi}\sigma} \exp[-\frac{(y-\bar{y})^2}{2\sigma^2}] \tag{4.15}$$

the free parameters $\bar{y}$ for the mean and σ^2 for the variance can be determined by requiring that the time–derivative of these quantities as calculated with the Fokker–Planck equation (3.6) vanishes in the steady state. These conditions result in the following two equations for $\bar{y}$ and σ^2

$$(\kappa\bar{y} - f_{\mathrm{ex}})/\gamma = d(\bar{w}^+ - \bar{w}^-) \tag{4.16}$$

and

$$\begin{aligned}(\kappa\sigma^2 + \kappa\bar{y^2} - f_{\mathrm{ex}}\bar{y} - 1)/\gamma =& d[(\bar{y} - \kappa d\theta^+\sigma^2)\bar{w}^+ - (\bar{y} + \kappa d\theta^-\sigma^2)\bar{w}^-] \\ &+ d^2(\bar{w}^+ + \bar{w}^-)/2,\end{aligned} \tag{4.17}$$

where we have introduced the average jump rates

$$\begin{aligned}\bar{w}^+ &\equiv \int_{-\infty}^{\infty} w^+(y)p^G(y)\,\mathrm{d}y \\ &= w_0 \exp[\mu_\mathrm{T} - \kappa(d\theta^+)^2(1-\kappa\sigma^2)/2 - \kappa d\theta^+\bar{y}] \qquad (4.18)\\ \bar{w}^- &\equiv \int_{-\infty}^{\infty} w^-(y)p^G(y)\,\mathrm{d}y \\ &= w_0 \exp[\mu_\mathrm{D} + \mu_\mathrm{P} - \kappa(d\theta^-)^2(1-\kappa\sigma^2)/2 + \kappa d\theta^-\bar{y}]. \qquad (4.19)\end{aligned}$$

These equations can easily be solved numerically.

4.3.2. Limits $\Delta\mu \to 0$ and $\Delta\mu \to \infty$

Close to chemical equilibrium, i.e., $\Delta\mu = 0$, and for $f_\mathrm{ex} = 0$, we expand $\bar{y}$ and $\kappa\sigma^2 - 1$ up to first order in $\Delta\mu$ and find

$$\bar{y} \approx A\Delta\mu + \tilde{A}(\theta^+ - \theta^-)^2\Delta\mu \qquad (4.20)$$

and

$$\kappa\sigma^2 - 1 \approx B(\theta^+ - \theta^-)\Delta\mu. \qquad (4.21)$$

The coefficients A, $\tilde{A}$ and B obtained by solving the first order of (4.16) and (4.17) are too long to be shown here.

In the limit $\Delta\mu \to \infty$ and $f_\mathrm{ex} = 0$, we obtain for $\bar{y}$ and $\kappa\sigma^2 - 1$

$$\bar{y} \approx \frac{\Delta\mu}{\kappa d} - C\Delta\mu \exp[-\Delta\mu\theta^-] \qquad (4.22)$$

and

$$\kappa\sigma^2 - 1 \approx D\Delta\mu \exp[-\Delta\mu\theta^-] \qquad (4.23)$$

as long as $\theta^- > 0$. The coefficients

$$C = \frac{1 + \kappa d^2(\theta^+ - \theta^-)^2/4}{\gamma\kappa d^3 w_0 \exp[\mu_\mathrm{D} + \mu_\mathrm{P}]} \qquad (4.24)$$

and

$$D = -\frac{\theta^+ - \theta^-}{2\gamma d^2 w_0 \exp[\mu_\mathrm{D} + \mu_\mathrm{P}]} \qquad (4.25)$$

are obtained by solving (4.16) and (4.17) to first and second order in $\Delta\mu$.

4.3.3. Efficiencies

Within this Gaussian approximation, the average heat flow through the probe as given by (4.9) is calculated using the local mean velocity (4.10)

$$\nu(y) = (\kappa y - f_{\mathrm{ex}})/\gamma - (y - \bar{y})/(\gamma\sigma^2). \tag{4.26}$$

The average over y can now be performed leading to

$$\dot{Q}_{\mathrm{P}} = (\kappa^2\sigma^2 + \kappa^2\bar{y}^2 - \kappa - 2\kappa f_{\mathrm{ex}}\bar{y} + f_{\mathrm{ex}}^2)/\gamma. \tag{4.27}$$

This expression is used to determine η_{Q} in this approximation as

$$\eta_{\mathrm{Q}} = d\kappa\frac{\kappa\sigma^2 - 1 + \kappa\bar{y}^2 - f_{\mathrm{ex}}\bar{y}}{\Delta\mu(\kappa\bar{y} - f_{\mathrm{ex}})} \tag{4.28}$$

with $\bar{y}$ and σ^2 being the solution of (4.16) and (4.17) for given nucleotide concentrations and w_0.

For small $\Delta\mu$, using (4.20) and (4.21), η_{Q} takes the form

$$\eta_{\mathrm{Q}} \approx \frac{dB(\theta^+ - \theta^-)}{(A + \tilde{A}(\theta^+ - \theta^-)^2)\Delta\mu} + \kappa dA + \kappa d\tilde{A}(\theta^+ - \theta^-)^2. \tag{4.29}$$

If $\theta^+ \neq \theta^-$, η_{Q} diverges for vanishing $\Delta\mu$. For $\theta^+ > \theta^-$, η_{Q} can become negative due to those jumps of the motor protein that occur when the previous diffusion of the probe has resulted in $y < -0.5d$. Then, the energy stored in the spring is dissipated by the motor protein during jumping.

In the limit of large $\Delta\mu$, we use (4.23) and (4.24) to obtain

$$\eta_{\mathrm{Q}} \approx 1 - \kappa dC\exp[-\Delta\mu\theta^-] + \frac{dD\exp[-\Delta\mu\theta^-]}{\Delta\mu/(\kappa d) - C\Delta\mu\exp[-\Delta\mu\theta^-]} \tag{4.30}$$

which approaches 1.

The Stokes efficiency in the Gaussian approximation without an external force is simply given by

$$\eta_{\mathrm{S}} = \frac{d\kappa\bar{y}}{\Delta\mu}. \tag{4.31}$$

For $\kappa\sigma^2 > 1$, which is the case for $\theta^+ < 0.5$, the Stokes efficiency is always smaller than η_{Q}. For vanishing $\Delta\mu$, η_{S} approaches a finite value, $\eta_{\mathrm{S}} \approx d\kappa A + d\kappa\tilde{A}(\theta^+ - \theta^-)^2$, while for $\Delta\mu \to \infty$ it also converges to 1.

4.4. Results

In this section, we study the three efficiencies for our hybrid model as functions of the chemical energy $\Delta\mu$, the absolute concentrations of the nucleotides, i.e. $w^{\mathrm{eq}} \equiv w_0 \exp[\mu_{\mathrm{T}}^{\mathrm{eq}}]$, the external force f_{ex} and the load sharing factor θ^+. The data are obtained from simulations (see Appendix A) and compared with the Gaussian approximation.

We use model parameters as given in table 4.1 which are motivated by experimental results for the F_1–ATPase as described in section 4.5 below. The load sharing factor θ^+ remains as a free parameter.

Table 4.1.: Values of the model parameters used for the simulation and the Gaussian approximation.

γ [s/d^2]	κ [d^{-2}]	$w^{\mathrm{eq}}/c_{\mathrm{ATP}}^{\mathrm{eq}}$ [$\mathrm{M}^{-1}\mathrm{s}^{-1}$]
0.407	40	3×10^7

4.4.1. Pseudo efficiency η_{Q}

We will first investigate the pseudo efficiency η_Q as a function of $\Delta\mu$, w^{eq} and θ^+. We extract $\dot{Q}_{\mathrm{P}}$ from the numerical data by averaging over one sufficiently long trajectory. The results are shown in Fig. 4.1. The most striking fact of these data is the observation that η_{Q} is larger than 1 for small enough $\Delta\mu$ and θ^+ which shows up in the Gaussian approximation as well. This effect can be understood as follows. In a jump, the motor protein can take heat from the solution in order to change the internal energy of the spring by an amount larger than $\Delta\mu$. If, subsequently, the probe dissipates this internal energy of the spring as heat back into the environment, $\dot{Q}_{\mathrm{P}}$ can indeed become larger than $\dot{\Delta\mu}$ without any violation of the second law. Using the obtained parameter for the spring constant κ, the motor protein transfers $20\,(k_{\mathrm{B}}T)$ to the spring if it starts the jump from the minimum of the harmonic potential. For small values of θ^+, the forward jump rate of the motor protein depends only weakly on the current position of the probe as shown in Fig. 4.2. Therefore, jumps will occur even if the associated change of internal energy of the spring, ΔV, is larger than $\Delta\mu$. For rather small w^{eq}, backward jumps are rare and the probe relaxes to the potential minimum between successive forward jumps. This leads to $\dot{V}_n > \dot{\Delta\mu}$ on average and hence to $\eta_Q > 1$ for $\Delta\mu$ considerably smaller than 20 as shown in Fig. 4.1. As the value of θ^+ increases, η_{Q} decreases because the forward jumps of the motor protein are

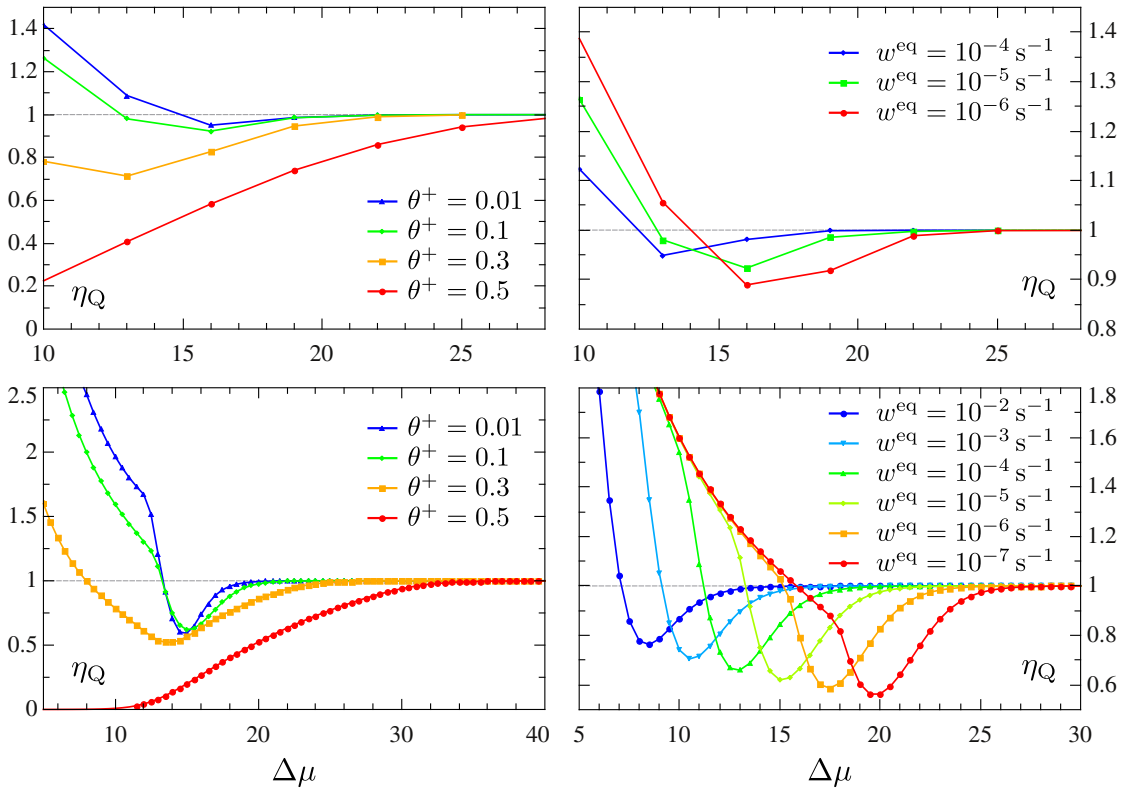

Figure 4.1.: Pseudo efficiency η_Q from the simulation, top; and within the Gaussian approximation, bottom. Top: η_Q as a function of $\Delta\mu$ for different values of the load sharing factor θ^+ and fixed $w^{eq} = 10^{-5}s^{-1}$. Bottom: η_Q as a function of $\Delta\mu$ for different values of w^{eq} with fixed $\theta^+ = 0.1$. The remaining parameters are $\kappa = d^{-2}$, $\gamma = 0.407s/d^2$. In the simulation, the error is of the order of the symbol size.

suppressed. On average, in this case the motor protein jumps only if the probe has diffused forward and exerts a pulling force on the motor through the spring.

Increasing the absolute concentrations of the nucleotides, i.e., increasing w^{eq}, results in more forward but also more backward jumps, which can be seen for the far right panel in Fig. 3.2. For small $\Delta\mu$, the occasional backward jumps follow especially those forward jumps for which the change of internal energy of the spring has been larger than $\Delta\mu$, leading to a smaller η_Q.

In the limit of large $\Delta\mu$, the motor protein jumps even when the spring is previously stretched which can result in changes of the internal energy of the spring by an amount larger than 20. The coupling between the motor protein and the probe induces a balancing effect between the forward motion of the motor

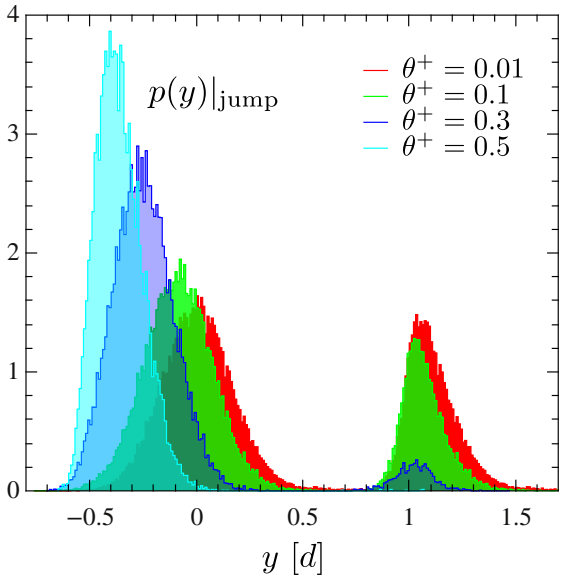

Figure 4.2: Probability distribution $p(y)|_{\text{jump}}$ of the distance y just before a jump of the motor protein for several values of θ^+ at $\Delta\mu = 13k_{\text{B}}T$ and $w^{\text{eq}} = 10^{-5}\text{s}^{-1}$. For small θ^+, the forward jumps of the motor protein are almost independent of the position of the probe resulting in a peak at $y \simeq 0$ whereas for larger θ^+ the peak clearly shifts to $y < 0$ implying that the motor protein prefers to jump when the probe has diffused ahead. The peaks around $y = 1$ indicate backward jumps which take place more often in the case of small θ^+ when the backward rate is more sensitive to the position of the probe.

protein and the drag of the probe maintaining a typical $\dot{V}$ that turns out to be approximately $\dot{\Delta}\mu$, leading to $\eta_{\text{Q}} \simeq 1$ (see also discussion in Appendix C).

4.4.2. Stokes efficiency η_{S}

We also obtain the Stokes efficiency (4.12) from the simulated trajectories and the Gaussian approximation as shown in Fig. 4.3. Characteristically, starting close to 0 for small $\Delta\mu$, η_{S} monotonically increases with $\Delta\mu$ reaching 1 for $\Delta\mu \to \infty$. For small $\Delta\mu$, the trajectory of the probe shows a staircase form with small average velocity leading to small values of the Stokes efficiency in contrast to values of the pseudo efficiency $\eta_{\text{Q}} > 1$. For large $\Delta\mu$, the probe does not relax to the potential minimum between consecutive jumps resulting in a more linear trajectory of the probe as if it was exposed to an almost constant force. In this limit of an almost linear motion of the probe, the pseudo efficiency becomes the Stokes efficiency. As η_{S} is bounded by 1, η_{Q} can not reach values larger than 1 in this limit either.

Increasing the load sharing factor θ^+ results in decreasing average velocities. Therefore, the Stokes efficiency also decreases which can be seen in Figs. 4.3 left, top and bottom. With increasing absolute concentrations of nucleotides, i.e., with increasing w^{eq}, the average velocity and therefore also the Stokes efficiency at fixed $\Delta\mu$ increases as shown in Figs. 4.3 right, top and bottom.

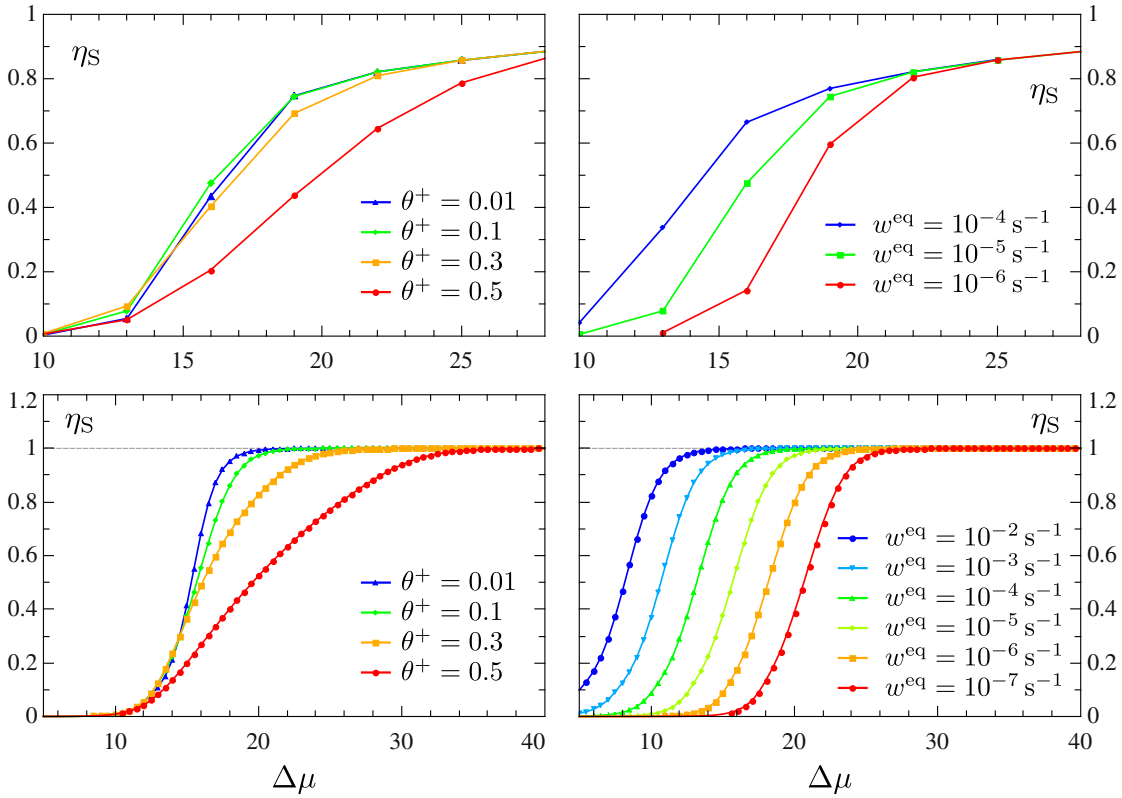

Figure 4.3.: (a) Stokes efficiency η_S from the simulation, top; and within the Gaussian approximation, bottom. The data is obtained from the same trajectories used to obtain η_Q in Fig. 4.1 top. Left: η_S as a function of $\Delta\mu$ for different values of the load sharing factor θ^+ and fixed $w^{eq} = 10^{-5}s^{-1}$. Right: η_S as a function of $\Delta\mu$ for different values of w^{eq} for fixed $\theta^+ = 0.1$.

4.4.3. Thermodynamic efficiency η_T

The thermodynamic efficiency of the system can be studied only if an external force is applied to the probe. Tight mechanochemical coupling of the one-state motor, i.e., the average velocity equals the rate of ATP hydrolysis, implies that η_T is given by Eq. (4.13). Hence, η_T increases linearly with f_{ex} for fixed $\Delta\mu$ up to stall conditions. For one-state motors, the stall force equals $\Delta\mu$ and $\eta_T|_{stall} = 1$ and $\dot{Q}_P = 0$. At stall conditions, the work corresponding to the stall force refers to the maximum work the motor protein can convert on average. Thus, the one-state motor is able to convert the full $\Delta\mu$ into extractable work. In our model, where the motor interacts with the external force only via the spring, this result is not as trivial as it would have been if we had applied f_{ex} directly to the motor. A detailed discussion about stall conditions also of multistate motors is given in section 6.3.

In the simulation, applying $f_{\rm ex} = \Delta\mu/d$ generates a diffusive motion of the motor protein with $v \simeq 0$ and $\dot{Q}_{\rm P} \simeq 0$ for various values of θ^+ and $\Delta\mu$, including the ones with $\eta_{\rm Q} > 1$ and $\eta_{\rm Q} < 1$. Under these conditions, $p^s(y)$ is Gaussian with $\langle y \rangle = \Delta\mu/(dk)$ and the same variance as the Boltzmann-distribution in equilibrium, $\sigma^2 = 1/\kappa$.

Within the Gaussian approximation we can insert $f_{\rm ex} = \Delta\mu/d$ in (4.16) and (4.17). With $\kappa\sigma^2 = 1$, $\bar{y} = \Delta\mu/(d\kappa)$, i.e., $v = 0$ is a solution for $f_{\rm ex} = \Delta\mu/d$ with $\dot{Q}_{\rm P} = 0$, implying that also in the Gaussian approximation the motor protein is able to convert the full $\Delta\mu$ into extractable work for any values of the load sharing factors given that $\theta^+ + \theta^- = 1$.

4.5. Case study: F_1-ATPase

In this section, we apply our hybrid model to the F_1–ATPase and compare the simulations with recent experimental data [15, 77, 148].

4.5.1. Model parameters

For a quantitative comparison we have to map the rotary motion of the F_1–ATPase to our linear model and determine the model parameters. In our model, one jump of the motor protein covering a distance d corresponds to a rotation of the γ shaft of 120°. Using large probe particles like polystyrene beads or actin filaments, the substeps in one 120° rotation are not resolved experimentally. Therefore, we will omit the substeps here, too. We assume that the solution is at room temperature ($T \simeq 24$°C) and that the probe consists of two beads of diameter 287nm [15]. The friction coefficient of the probe can be calculated using the formula for the rotational frictional coefficient Γ from [41, 119] with the viscosity

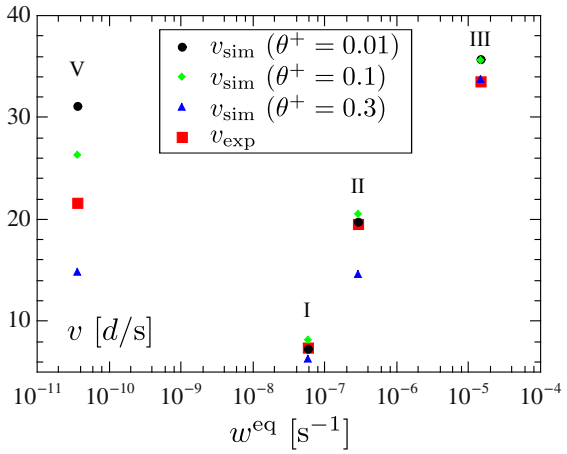

Figure 4.4: Comparison of the mean velocities observed experimentally [15] (red squares) and in the simulation for several load sharing factors θ^+ (black dots, green diamonds and blue triangles). The labeling I, II, III, V refers to the corresponding parameter sets in Fig. 4.5.

of water ($\eta \simeq 0.001\mathrm{Ns/m^2}$). The frictional torque $N = \Gamma\dot{\varphi}$ acting on the probe with angular velocity $\dot{\varphi}$ corresponds to a frictional force

$$f_{\mathrm{fr}} = \frac{\Gamma}{r^2}\dot{x} = \gamma\dot{x} \tag{4.32}$$

acting on the probe at distance r from the γ shaft. Within one 120° rotation, the probe at distance r covers $d = 2\pi r/3$. For the linear model, the friction coefficient γ can be calculated as

$$\gamma = \frac{\Gamma}{r^2} = \frac{4\pi^2\Gamma}{9d^2} \tag{4.33}$$

leading to $\gamma = 0.407\mathrm{s}/d^2$.

Following the mass action law assumption, the equilibrium transition rate w^{eq} is supposed to depend linearly on the concentrations of nucleotides in the solvent. For low ATP concentrations ($c_{\mathrm{ATP}} \simeq 10^{-6}\mathrm{M}$), the mean velocity of the motor protein is dominated by the rate of ATP binding. In the one-step model this feature holds for all concentrations. Therefore we choose w^{eq} to be the experimentally determined rate of ATP binding $w^{\mathrm{eq}} \simeq 3 \times 10^7\mathrm{M^{-1}s^{-1}}c^{\mathrm{eq}}_{\mathrm{ATP}}$[74]. For known nonequilibrium concentrations of nucleotides like in the experiments, the structure of the transition rates (3.3) and (3.4) leaves the choice of the equilibrium concentrations arbitrary as long as they obey

$$\frac{c^{\mathrm{eq}}_{\mathrm{ATP}}}{c^{\mathrm{eq}}_{\mathrm{ADP}}c^{\mathrm{eq}}_{\mathrm{P_i}}} \simeq 4.89 \times 10^{-6}\frac{1}{\mathrm{M}} \tag{4.34}$$

for pH 7 (and $T = 23°\mathrm{C}$) [41]. For given w^{eq} and $\Delta\mu$, one possible choice of the nonequilibrium concentrations of nucleotides is $c_{\mathrm{ADP}} = c^{\mathrm{eq}}_{\mathrm{ADP}}$, $c_{\mathrm{P_i}} = c^{\mathrm{eq}}_{\mathrm{P_i}}$ and $c_{\mathrm{ATP}} = c^{\mathrm{eq}}_{\mathrm{ATP}}\exp[\Delta\mu]$ which was used for the simulation and the Gaussian approximation.

In order to determine the spring constant κ and the load sharing factor θ^+ we use both the experimental data of the mean velocities [15] and the histogram of the angular position of the probe at a jump [148]. While both data sets depend on both parameters, the velocity, especially for large w^{eq}, is more sensitive to κ whereas the peak position of the histogram mainly depends on θ^+. Therefore, we primarily use the velocity data to fit κ and determine the load sharing factor θ^+ by comparing the peak position of the experimental histogram [148] with the left peak position of the corresponding histograms obtained by our simulation as the ones shown in Fig. 4.2.

As a result, we obtain $\kappa = 40 \pm 5\,d^{-2}$ and a value of θ^+ in the range $0.1 \lesssim \theta^+ \lesssim 0.3$. In Fig. 4.4, we show how for this value of κ changing the load sharing factor affects the mean velocity for which we get the best overall agreement for $\theta^+ = 0.1$. Experiments on the ATP binding and hydrolysis rates as functions of

the rotary angle indicate that 9% of the ATP-binding step is supported by thermal fluctuations which agrees very well with $\theta^+ = 0.1$ [138]. For later purposes, we also include data for $\theta^+ = 0.01$.

4.5.2. Comparison of efficiencies with experimental data

Pseudo efficiency

Experimentally, the heat flow of the probe is determined using the Harada-Sasa relation [156]. In the appendix, we show that this heat flow is equal to $\dot{Q}_\mathrm{P}$ as defined in (4.9). In Fig. 4.5, we plot the average heat released through the probe per step, Q_P, plus the work against the external force, W, obtained by the simulation for $\kappa = 40\, d^{-2}$ and $\theta^+ = 0.1$ and compare it with the experimental results [15]. We find quite good agreement between theory and experiment for the parameter sets I-IV where either the maximum deviation is 15% (II-IV) or our theoretical value is included in the experimental error range (I). As an aside, we note that for the parameter sets I-III (without external force) also the simulated mean velocities coincide well with the experimental values with a maximum deviation of 10% as shown in Fig. 4.4. For illustrative purposes, we also plot Q_P plus W for $\theta^+ = 0.01$ which shows better agreement with the experimental data (but is not consistent with the range of θ^+ obtained in section 4.5.1).

Discrepancies between our theory and the experiment are visible in Figs. 4.4 and 4.5 where for parameter set V both the average velocity and the pseudo efficiency deviate significantly from the experimental values for $\kappa = 40\, d^{-2}$ and $\theta^+ = 0.1$. For $\Delta\mu = 28.12(k_\mathrm{B}T)$ corresponding to the data set V in Fig. 4.5, the probe just reaches the potential minimum between consecutive jumps of the motor protein. Therefore on average at most $20(k_\mathrm{B}T)$ can be transferred to the spring leading to $\eta_\mathrm{Q} \simeq 0.7$, which is less than the experimental value. This discrepancy is most likely caused by the simplicity of our model which does not capture the structural complexity of the motor and the linker.

The confinement of θ^+ to the range $0.1 \lesssim \theta^+ \lesssim 0.3$ implies on the one hand that the potential of mean force of the motor protein should be asymmetric and on the other hand that asymmetric potentials with a barrier state close to the initial state seem to enhance the ability of the motor protein to perform work on the spring, in accordance with [157]. If θ^+ was larger, η_Q would decrease and the experimentally determined values of η_Q would not be reached in the simulation. If θ^+ was smaller, η_Q would approach the experimental values better, however, the distribution of the position of the probe just before a jump as shown in Fig. 4.2 would then no longer coincide with the experimentally observed distribution (see [148]).

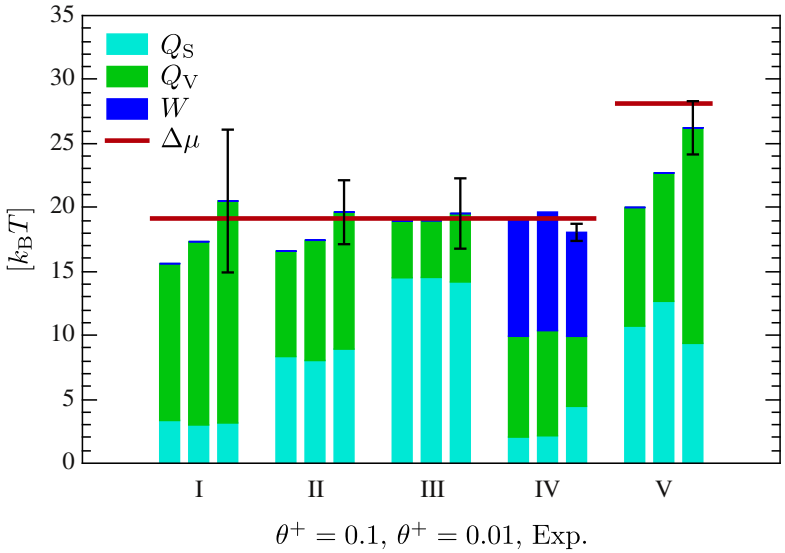

Figure 4.5.: Average heat Q_P released through the probe (green and cyan) and work $W \equiv f_{ex} d$ against the external force (blue) compared to the available free energy per step $\Delta\mu$ (red line). The dissipated heat of the probe is split into two contributions Q_S and Q_V according to the two terms of the Harada–Sasa relation (B.3). The contribution from the linear motion with constant mean velocity, Q_S (cyan), appears in the numerator of the Stokes efficiency while Q_V (green) is the contribution due to the non–uniform jumping motion of the motor protein. In each of the five parameter sets labeled by I-V, the left and the central bar represent results from the simulation for $\theta^+ = 0.1$ and $\theta^+ = 0.01$, respectively, while the right bar shows the experimental results and error bars from [15]. The following parameters were used in the five cases: (I) $c_T = 0.4\mu M$, $c_D = 0.4\mu M$, $c_P = 1mM$, i.e, $w^{eq} = 5.87 \times 10^{-8}\,s^{-1}$ and $\Delta\mu = 19.14$; (II) $c_T = 2\mu M$, $c_D = 2\mu M$, $c_P = 1mM$, i.e, $w^{eq} = 2.93 \times 10^{-7}\,s^{-1}$ and $\Delta\mu = 19.14$; (III) $c_T = 100\mu M$, $c_D = 100\mu M$, $c_P = 1mM$, i.e, $w^{eq} = 1.47 \times 10^{-5}\,s^{-1}$ and $\Delta\mu = 19.14$; (IV) $c_T = 2\mu M$, $c_D = 2\mu M$, $c_P = 1mM$, $f_{ex} = 9.27 d^{-1}$, i.e, $w^{eq} = 2.93 \times 10^{-7}\,s^{-1}$ and $\Delta\mu = 19.14$; (V) $c_T = 2\mu M$, $c_D = 0.5\mu M$, $c_P = 0.5\mu M$, i.e, $w^{eq} = 3.67 \times 10^{-11}\,s^{-1}$ and $\Delta\mu = 28.12$.

Thermodynamic efficiency

Information about the thermodynamic efficiency of the motor protein can be obtained by applying an external force to the probe. In Fig. 4.6 we show the extracted/delivered work as well as the dissipated heat and their sum obtained from our simulations in comparison with experimental results from [118, 158]. The data is obtained for a fixed value of $\Delta\mu$ by increasing the external force from 0 far beyond the stall force.

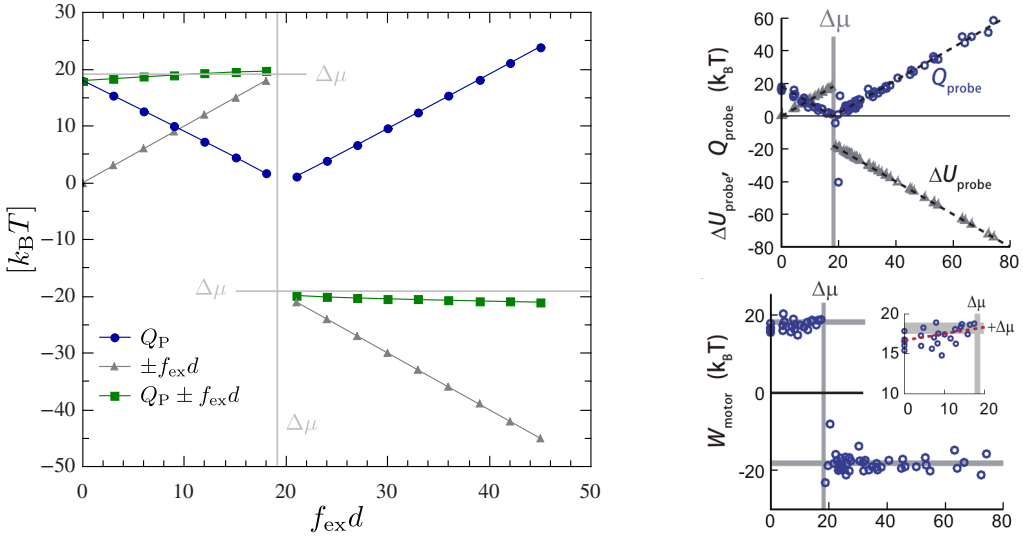

Figure 4.6.: Comparison of the simulation results (left) with experimental data from [118] (right). The concentrations used in the simulation are the same as in the experiment: $c_T = c_D = 10\mu M$, $c_P = 1mM$, $\theta^+ = 0.1$.

The extracted work increases up to $f_{ex}d = \Delta\mu$ at the stall force, which is found to be $f_{ex}^{st} = \Delta\mu/d$ also in the experiment [77, 158]. Thus, the motor is able to convert the full $\Delta\mu$ into extractable work without any dissipation. Both in the experiment and in the simulation, the dissipated heat through the probe decreases linearly from almost $\Delta\mu$ at $f_{ex} = 0$ to zero at the stall force.

Beyond stall conditions, the external force has to be considered as energy supply to run the F_1-ATPase in reverse to synthesize ATP. Producing one ATP molecule, the motor uses $(-)\Delta\mu$ from the available $(-)f_{ex}d$ per step. The excess energy delivered by the external force is then dissipated through the motor and the probe as heat. We find that the dissipated heat increases linearly with f_{ex} which implies that the excess energy is mainly dissipated through the probe.

The sum of both contributions, extracted/delivered work and dissipated heat through the probe, is almost equal to $\pm\Delta\mu$ for external forces both smaller and larger than the stall force. This corresponds to the almost dissipation-free energy conversion in the motor. Note that even if the energy conversion in the motor is dissipation-free, any $v \neq 0$ involves dissipation at the probe. The maximum extracted work with $\dot{Q}_P = 0$, $\dot{Q}_M = 0$ can be attained only at $v = 0$. For the parameters used in the experiment, we find a very good agreement between our simulation and the experimental data also for external forces far beyond the stall force.

One has to keep in mind that the parameters used in this illustrative example

yield a pseudo efficiency of almost 1 in the absence of external forces. Using parameters which yield smaller or larger pseudo efficiencies for $f_{\mathrm{ex}} = 0$, one should also expect deviations of $\eta_{\mathrm{Q}} \simeq 1$ in the presence of external forces.

It is important to note that observing $f_{\mathrm{ex}}d{=}\Delta\mu$ at stall conditions does not imply that the motor does not have idle cycles. That condition just states that the full $\Delta\mu$ obtained from one hydrolysis event can be converted into mechanical power. However, as long as one does not measure the rate of ATP turnover, there can be many additional idle cycles wasting $\Delta\mu$ without any displacement (see detailed discussion in section 6.5). Experiments controlling also the ATP concentrations indicate that the F_1-ATPase does not have idle cycles [86].

4.6. Conclusion

In summary, we have discussed three types of efficiencies within a hybrid-model with one-state motor using both simulations and a Gaussian approximation to the stationary distribution for the distance between motor and probe. The genuine thermodynamic efficiency is non-zero only if an external force is applied to the probe. The Stokes efficiency deviates from 1 due to the discrete nature of the motor steps which become less relevant with increasing ATP concentration. A pseudo efficiency measuring how much of the free energy of ATP hydrolysis ends up in loading the elastic element can even become larger than 1 close to equilibrium and for a barrier state close to the initial state. This result is not in conflict with the second law since the pseudo efficiency involves heat dissipated by the probe rather than work that is extracted from the system.

Applying this minimal model to recent experimental data for the F_1–ATPase we find overall good agreement concerning all three types of efficiencies. Considering the pseudo efficiency, deviations occur for those parameters where especially the P_i concentration is very small originating from the simplicity of our model. To overcome these limitations, we have split the 120° rotation into two steps of 90° and 30° (see section 3.3 and Fig. 3.3) and also incorporated an additional hydrolysis step. The linker potential has been replaced by a superposition of two harmonic potentials with different spring constants weighted depending on y. Even with these amendments, we do not obtain simulation results that match the experimental data over the complete parameter range considering average velocity, pseudo efficiency and the shape of the velocity autocorrelation function.

Since any extension of the model comes along with additional fit parameters and a much more complicated analysis, we show only results from the simple one-state model and the harmonic linker here. The basic properties of motor-bead interaction are already captured by this simple setup, which provides deeper insight into the origin of the observed effects.

5. Influence of cargo particle on motor dynamics

5.1. Introduction

The presence of probe particles not only constitutes a drag on the motor slowing down its average velocity but also severely influences its dynamics. It has been found that the presence of cargo particles can make the motor dynamics almost deterministic and also change its dwell-time distribution from a single-exponential distribution to a distribution with a distinct peak [135, 159].

In this chapter, we will present an additional effect that demonstrates the influence of the probe on the dynamics of the motor. Analyzing experimental data, it is essential to be aware of these effects caused by probe particles. Attributing all features to the motor dynamics would yield overly complex motor models with "wrong" parameters.

First, we will focus on the velocity autocorrelation function and the response function of the probe particle since these quantities can be investigated experimentally [15]. We investigate three different simplified one-state motor models with different motor dynamics to identify which motor characteristics causes the structure in the correlation and response function observed in the simulation (and also slightly in experimental data). We find that it is possible to infer properties of the dynamics of the motor from the velocity autocorrelation of the probe particle. As a consequence thereof, the influence of the probe on the dynamics of the motor is also visible in the velocity autocorrelation. Second, we will briefly discuss the dwell-time distribution between subsequent motor jumps in our one-state motor model.

The analysis in this chapter is restricted to NESS conditions without external forces acting on the probe. In order to obtain analytical results with the simplified models, we will assume a harmonic linker potential.

5.2. Velocity autocorrelation function and response function

5.2.1. General aspects

An experimentally accessible quantity in single-molecule setups is the velocity autocorrelation function (VACF) of the probe particle as measured in [15]. The VACF is defined as

$$C_{\dot{x}}(t_2, t_1) \equiv \langle \dot{x}(t_2)\dot{x}(t_1)\rangle. \tag{5.1}$$

Inserting the Langevin equation for the dynamics of the probe particle, Eq. (3.1), with the harmonic linker potential $V(y) = \kappa y^2/2$, the VACF takes the following form

$$\begin{aligned} C_{\dot{x}}(t_2, t_1) =& \kappa^2 \left(\langle n(t_2)n(t_1)\rangle - \langle n(t_2)x(t_1)\rangle - \langle x(t_2)n(t_1)\rangle + \langle x(t_2)x(t_1)\rangle\right)/\gamma^2 \\ &+ \kappa \left(\langle n(t_2)\zeta(t_1)\rangle - \langle x(t_2)\zeta(t_1)\rangle + \langle \zeta(t_2)n(t_1)\rangle - \langle \zeta(t_2)x(t_1)\rangle\right)/\gamma \\ &+ \langle \zeta(t_2)\zeta(t_1)\rangle. \end{aligned} \tag{5.2}$$

The linear response of the average velocity of the probe at time t_2 to a small external perturbation $h(t)$ applied at t_1 is defined as [44]

$$R_{\dot{x}}(t_2, t_1) \equiv \frac{\delta\langle \dot{x}(t_2)\rangle}{\delta h(t_1)}\Big|_{h=0}. \tag{5.3}$$

In the NESS, the response function can be expressed by a correlation function

$$R_{\dot{x}}(t_2, t_1) = \langle \dot{x}(t_2)B(t_1)\rangle \tag{5.4}$$

with the conjugate variable $B(t)$. The conjugate variable can be calculated, *inter alia*, using a path weight approach [160]. The path weight of the full system with motor and probe dynamics is given by $\mathcal{P}[n(t), x(t), h(t)] \equiv \exp\left[-S[n(t), x(t), h(t)]\right]$ with

$$\begin{aligned} S[n(t), x(t), h(t)] =& S^{\text{motor}}[n(t)|x(t), h(t)] \\ &+ \frac{\gamma}{4}\int_0^t \Big(\left(\dot{x}(t') - (\kappa y(t') - f_{\text{ex}} + h(t'))/\gamma\right)^2 \\ &\qquad + \partial_x \left(\kappa y(t') - f_{\text{ex}} + h(t')\right)/(2\gamma)\Big)\, \mathrm{d}t' \end{aligned} \tag{5.5}$$

where the explicit expression for the action $S^{\text{motor}}[n(t)|x(t), h(t)]$ depends on the actual motor model. If the small perturbation acts only on the probe (which is

the case in all of our models considered here), the conjugate variable $B(t)$ includes only contributions from the dynamics of the probe particle,

$$B(t_1) = -\frac{\delta S[n(t), x(t), h(t)]}{\delta h(t_1)}\Big|_{h=0} \tag{5.6}$$

$$= -\frac{\delta}{\delta h(t_1)}\Big[\frac{\gamma}{4}\int_0^t \Big((\dot{x}(t') - (\kappa y(t') - f_{\mathrm{ex}} + h(t'))/\gamma)^2 + \partial_x(\kappa y(t') - f_{\mathrm{ex}} + h(t'))/(2\gamma)\Big)\,\mathrm{d}t'\Big]\Big|_{h=0} \tag{5.7}$$

$$= \frac{1}{2}\left(\dot{x}(t_1) - (\kappa y(t_1) - f_{\mathrm{ex}})/\gamma\right). \tag{5.8}$$

The response function then follows as

$$R_{\dot{x}}(t_2, t_1) = \frac{1}{2}\langle \dot{x}(t_2)[\dot{x}(t_1) - (\kappa y(t_1) - f_{\mathrm{ex}})/\gamma]\rangle. \tag{5.9}$$

Using the Langevin equation (3.1), the response function can be simplified by replacing $(\kappa y(t) - f_{\mathrm{ex}})/\gamma = \dot{x}(t) - \zeta(t)$ [153],

$$R_{\dot{x}}(t_2, t_1) = \frac{1}{2}\langle \dot{x}(t_2)\zeta(t_1)\rangle \tag{5.10}$$

$$= \frac{1}{2}\Big(\kappa\langle n(t_2)\zeta(t_1)\rangle/\gamma - \kappa\langle x(t_2)\zeta(t_1)\rangle/\gamma + \langle\zeta(t_2)\zeta(t_1)\rangle\Big). \tag{5.11}$$

For systems in equilibrium, a relation known as the fluctuation-dissipation theorem (FDT) states that the response function equals the VACF [46, 161, 162].

5.2.2. Independent motor dynamics

Velocity autocorrelation

First, we will consider a simplification of the one-state motor model introduced in section 3.2. We assume that the motor performs a biased random walk on a discrete state space independent of the probe position. The rates then obey a reduced LDB condition

$$\frac{w^+}{w^-} = \exp[\Delta\mu]. \tag{5.12}$$

The dynamics of the probe evolves according to the Langevin equation (3.1) with $V(y) = \kappa y^2/2$ whose formal solution for $f_{\mathrm{ex}} = 0$ and $x(0) = 0$ is given by

$$x(t) = \exp[-\kappa t/\gamma]\int_0^t (\kappa n(t')/\gamma + \zeta(t'))\exp[\kappa t/\gamma]\,\mathrm{d}t'. \tag{5.13}$$

Using this expression, the VACF in the form (5.2) can be calculated analytically. Since $n(t)$ and $\zeta(t)$ are independent, we have $\langle n(t)\zeta(t')\rangle = \langle n(t)\rangle\langle\zeta(t')\rangle = 0$.

The autocorrelation function of the motor position can be obtained using the generating function [43] of the corresponding master equation

$$\partial_t p(i,t) = p(i-1,t)w^+ + p(i+1,t)w^- - p(i,t)(w^+ + w^-) \tag{5.14}$$

with $n = di$. For the initial condition $p(i,t_1) = \delta_{ij}$, the generating function reads

$$F(z,t \mid j,t_1) \equiv \sum_i z^i p(i,t) \tag{5.15}$$

$$= \exp\left[(w^+ z + w^-/z - (w^+ + w^-))(t-t_1)\right] z^j. \tag{5.16}$$

Using the properties of the generating function [43], the autocorrelation function of the motor position is given by [163]

$$\langle n(t_2)n(t_1)\rangle = d^2(w^+ - w^-)^2 t_2 t_1 + d^2(w^+ + w^-)t_1 \qquad \text{for } t_1 < t_2. \tag{5.17}$$

The VACF of the probe particle for independent motor jumps can now be calculated and yields in the limit $t_2, t_1 \to \infty$,

$$C_{\dot{x}}^{\mathrm{ind}}(\tau) = \frac{\kappa}{\gamma}\left(\frac{d^2}{2}(w^+ + w^-) - \frac{1}{\gamma}\right)\exp[-\kappa\tau/\gamma] + \frac{2}{\gamma}\delta(\tau) + d^2(w^+ - w^-)^2. \tag{5.18}$$

with the average velocity $d(w^+ - w^-)$ and $\tau = t_2 - t_1$.

For independent motor jumps, the VACF of the probe particle decays exponentially on the timescale of the relaxation of the probe just as an overdamped harmonic oscillator would. The presence of the motor affects only the amplitude of the VACF. Depending on whether the (bare) diffusion coefficient of the probe, $1/\gamma$, is larger or smaller than the diffusion coefficient of the motor, $d^2(w^+ + w^-)/2$, the velocity of the probe is anticorrelated or correlated (relative to the squared average velocity), respectively.

If the diffusion coefficient of the motor is smaller than the one of the probe, jumps are rather rare and the probe spends most of the time fluctuating around $y = 0$. If fluctuations induce velocities of the probe significantly larger (smaller) than the average velocity, the restoring force of the stretched linker will induce a smaller (larger) velocity of the probe shortly after. Therefore, in the anticorrelated regime, the influence of motor jumps is barely noticeable and the correlation of the velocity is dominated by the restoring force of the linker.

For large diffusion coefficients of the motor, frequent forward and backward jumps of the motor occur. Suppose a jump of the motor induces a large velocity of

the probe, the velocity will typically remain larger than the average until the probe has relaxed yielding a positive correlation of the velocity. Since motor jumps are frequent, such events outweigh the influence of the restoring force. Furthermore, fluctuation-induced large velocities of the probe may be even more increased by subsequent motor jumps in the corresponding direction.

Response function

Since the contribution of the motor jumps to the action of the path weight is independent of the perturbation, the response function in the form of Eq. (5.11) can be used, where the first summand is zero. A simple calculation then yields

$$R_{\dot{x}}^{\mathrm{ind}}(\tau) = -\frac{\kappa}{\gamma^2}\exp[-\kappa\tau/\gamma] + \frac{1}{\gamma}\delta(\tau). \tag{5.19}$$

This response function is equivalent to the response function of an overdamped harmonic oscillator. Except for $w^+ = w^- = 0$, it never matches the VACF, not even in equilibrium, which constitutes a violation of the FDT. The origin of the violation is the missing coupling of the motor to the spring. Since the external perturbation causing the response is applied to the probe particle, the dynamics of the motor is not influenced by the external perturbation at all. Therefore, the response of the velocity of the probe to such an external perturbation does not contain any contributions of the motor dynamics either.

Obviously, omitting the coupling of the motor to the linker results in an unphysical system. In any well-defined model, the FDT in equilibrium should hold. In the case of violated FDT, also the heat flow through the probe particle obtained using stochastic thermodynamics, Eq. (4.1), is no longer consistent with the heat flow obtained using the Harada-Sasa relation (see Appendix B).

5.2.3. Continuous motor dynamics

Velocity autocorrelation

As mentioned above, omitting the influence of the coupling on the motor dynamics is quite unrealistic. Therefore we want to set up a model that is able to capture the full coupling between motor and probe while still being analytically tractable. A possible realization comprises two coupled degrees of freedom representing motor and probe that perform a biased diffusion on a continuous state space. The dynamics of motor and probe are then represented by two harmonically coupled overdamped Langevin equations

$$\dot{x}(t) = \kappa\left(n(t) - x(t)\right)/\gamma + \zeta(t) \tag{5.20}$$

$$\dot{n}(t) = -\lambda\kappa\left(n(t) - x(t)\right)/\eta + \Delta\mu/(\eta d) + \xi(t), \tag{5.21}$$

where η is the friction coefficient and $\xi(t)$ with $\langle \xi(t_2)\xi(t_1)\rangle = 2\delta(t_2 - t_1)/\eta$ the thermal noise acting on the motor. For later purposes, we introduce a coupling strength λ. The chemical energy obtained from ATP turnover is represented by a chemical force or affinity $\Delta\mu/d$ acting on the motor. (The chemical contribution can also be incorporated in the thermal noise in form of a nonzero average of the noise.) Since the two coupled Langevin equations are linear, they can be written as a matrix equation

$$\underbrace{\begin{pmatrix}\dot{x}(t)\\ \dot{n}(t)\end{pmatrix}}_{\dot{\mathbf{z}}(t)} = \underbrace{\begin{pmatrix}-\kappa/\gamma & \kappa/\gamma\\ \lambda\kappa/\eta & -\lambda\kappa/\eta\end{pmatrix}}_{\mathbf{K}} \underbrace{\begin{pmatrix}x(t)\\ n(t)\end{pmatrix}}_{\mathbf{z}(t)} + \underbrace{\begin{pmatrix}\zeta(t)\\ \Delta\mu/(\eta d) + \xi(t),\end{pmatrix}}_{\mathbf{\Gamma}(t)} \tag{5.22}$$

whose solution for $x(0) = 0$, $n(0) = 0$ is given by [44]

$$z_i(t) = \int_0^t G_{ij}(t - t')\Gamma_j(t')\,\mathrm{d}t' \tag{5.23}$$

with Green's function $\mathbf{G}(t) = \exp[\mathbf{K}t]$. The explicit solutions read

$$\begin{aligned} x(t) = \int_0^t \Bigg(&\frac{\lambda\gamma\zeta(t') + \eta\xi(t') + \Delta\mu/d}{\lambda\gamma + \eta} \\ &- \frac{\eta(\xi(t') - \zeta(t')) + \Delta\mu/d}{\lambda\gamma + \eta} \exp\left[-\kappa\frac{\lambda\gamma + \eta}{\gamma\eta}(t - t')\right]\Bigg)\,\mathrm{d}t' \end{aligned} \tag{5.24}$$

$$\begin{aligned} n(t) = \int_0^t \Bigg(&\frac{\lambda\gamma\zeta(t') + \eta\xi(t') + \Delta\mu/d}{\lambda\gamma + \eta} \\ &+ \frac{\lambda\gamma\left(\xi(t') - \zeta(t') + \Delta\mu/(\eta d)\right)}{\lambda\gamma + \eta} \exp\left[-\kappa\frac{\lambda\gamma + \eta}{\gamma\eta}(t - t')\right]\Bigg)\,\mathrm{d}t'. \end{aligned} \tag{5.25}$$

Inserting these expressions in the VACF (5.2) and using the correlations of the noise, we obtain in the limit $t_2, t_1 \to \infty$

$$\begin{aligned} C_{\dot{x}}^{\mathrm{cont}}(\tau) =& \frac{\kappa}{\gamma}\left(\frac{\gamma + \eta}{\gamma(\lambda\gamma + \eta)} - 2/\gamma\right)\exp\left[-\kappa\frac{\lambda\gamma + \eta}{\gamma\eta}\tau\right] + \frac{2}{\gamma}\delta(\tau) \\ &+ \frac{\Delta\mu^2}{d^2(\lambda\gamma + \eta)^2}. \end{aligned} \tag{5.26}$$

If we consider $\lambda = 1$, which corresponds to symmetric coupling of motor and probe to the linker, the VACF reduces to

$$C_{\dot{x}}^{\mathrm{cont}}(\tau) = -\frac{\kappa}{\gamma^2}\exp\left[-\kappa\frac{\eta + \gamma}{\eta\gamma}\tau\right] + \frac{2}{\gamma}\delta(\tau) + \frac{\Delta\mu^2}{(\eta + \gamma)^2 d^2}. \tag{5.27}$$

It has the same amplitude (relative to the squared average velocity) as a harmonic oscillator that is obtained by fixing the motor position. For the coupled continuous scenario, however, the VACF decays faster than the harmonic oscillator with an effective friction coefficient $\eta\gamma/(\eta+\gamma)$ since the motor contributes to the relaxation of the linker. If the linker is stretched, its restoring force acts on probe and motor in the same fashion and induces a drift of the probe and, as the motor moves continuously, also of the motor in the opposite direction relaxing the linker. Thus, the relaxation time of the restoring force and therefore also the correlation time of the VACF is smaller than in the previous scenario where the restoring force acts only on the probe particle.

We will now consider $\lambda = 0$ which corresponds to zero coupling. This scenario is analogous to the assumption that the jump rates introduced in the previous section are independent of the probe position. In this limit, the VACF is given by

$$C_{\dot{x}}^{\mathrm{cont}}(\tau) = \frac{\kappa}{\gamma}\left(\frac{1}{\eta} - \frac{1}{\gamma}\right)\exp[-\kappa\tau/\gamma] + \frac{2}{\gamma}\delta(\tau) + \frac{\Delta\mu^2}{\eta^2 d^2}, \tag{5.28}$$

which is consistent with Eq. (5.18) since $1/\eta$ represents the diffusion coefficient of the motor and $\Delta\mu/(\eta d)$ the average velocity.

Response function

The response function is given by Eq. (5.11) and can be calculated easily yielding

$$R_{\dot{x}}^{\mathrm{cont}}(\tau) = -\frac{\kappa}{\gamma^2}\exp\left[-\kappa\frac{\lambda\gamma+\eta}{\gamma\eta}\tau\right] + \frac{1}{\gamma}\delta(\tau). \tag{5.29}$$

For the fully coupled scenario with $\lambda = 1$ we obtain

$$R_{\dot{x}}^{\mathrm{cont}}(\tau) = -\frac{\kappa}{\gamma^2}\exp\left[-\kappa\frac{\gamma+\eta}{\gamma\eta}\tau\right] + \frac{1}{\gamma}\delta(\tau), \tag{5.30}$$

which is consistent with the VACF (5.27) in equilibrium, where we have $\Delta\mu = 0$ and vanishing average velocity $\Delta\mu/((\eta+\gamma)d) = 0$. The δ contribution lacks the prefactor 2 since $R_{\dot{x}}(\tau)$ is only defined for $\tau \geq 0$. Thus, the fully coupled model fulfills the FDT in equilibrium. In the case $\lambda = 0$, the response function (5.29) reduces to Eq. (5.19) which again violates the FDT.

In NESS conditions, the VACF (5.27) differs from the response function (5.30) only by an offset given by the squared average velocity. Therefore, the heat flow through the probe is simply given by the contribution appearing in the Stokes efficiency, $\dot{Q}_{\mathrm{P}} = \gamma\Delta\mu^2/(d^2(\eta+\gamma)^2) = \gamma v^2$, which can easily be seen using the Harada-Sasa relation. Apparently, continuous motor dynamics (energetically) resembles a constant external driving of the probe particle. Detailed discussions of the efficiency of this model can be found in Appendix C.

Note that despite the coupling between the dynamics of motor and probe, the VACF as well as the response function decay purely exponentially.

5.2.4. Fully deterministic motor jumps

Velocity autocorrelation

We will now return to the discrete modeling of the motor. In contrast to section 5.2.2, we assume that the motor jumps deterministically, i.e., after a fixed time-interval T the motor jumps a distance d in the forward direction. Its trajectory is then given by

$$n(t) = d \left\lfloor \frac{t}{T} \right\rfloor \tag{5.31}$$

with initial condition $n(0) = 0$, where $\lfloor . \rfloor$ represents the floor function. The dynamics of the probe obeys the Langevin equation (3.1).

Using the formal solution of the Langevin equation (5.13) and the explicit trajectory $n(t)$, the VACF (5.2) can be calculated analytically. Since $n(t)$ is a deterministic process and independent of $x(t)$, we have $\langle n(t_2)n(t_1)\rangle = d^2 \lfloor t_2/T \rfloor \lfloor t_1/T \rfloor$ and $\langle n(t)\zeta(t')\rangle = 0$. The calculation of the VACF is lengthy but straightforward, therefore it is not shown here. In the limit $t_2, t_1 \to \infty$ the VACF is given by

$$\begin{aligned}\langle \dot{x}(t_2)\dot{x}(t_1)\rangle =& \frac{d^2\kappa^2 \exp[2\kappa T/\gamma]}{\gamma^2(1-\exp[\kappa T/\gamma])^2} \exp[-\kappa T(\mathrm{S}(t_2)+\mathrm{S}(t_1))/\gamma] \\ & - \frac{\kappa}{\gamma^2}\exp[\kappa(t_2-t_1)/\gamma] + \frac{2}{\gamma}\delta(t_2-t_1) \qquad \text{for } t_1 < t_2,\end{aligned} \tag{5.32}$$

where we have made use of the sawtooth wave $\mathrm{S}(t) = t/T - \lfloor t/T \rfloor$. Note that the average is an ensemble average or average over the noise for fixed t_1, t_2. Since motor jumps are deterministic, the VACF according to Eq. (5.2) depends explicitly on t_1, t_2. Choosing a specific starting point t_1, the next motor jump occurs at the same time for every trajectory that contributes to the average. Therefore, the velocity autocorrelation as a function of the time difference $t_2 - t_1$ can be obtained by averaging Eq. (5.32) over all starting points t_1 within a time interval T keeping $\tau = t_2 - t_1$ fixed,

$$C_{\dot{x}}^{\mathrm{det}}(\tau) = \overline{\langle \dot{x}(t_2)\dot{x}(t_1)\rangle} \equiv \frac{1}{T}\int_0^T \langle \dot{x}(t_2)\dot{x}(t_1)\rangle \,\mathrm{d}t_1 = \frac{1}{T}\int_0^T \langle \dot{x}(t_1+\tau)\dot{x}(t_1)\rangle \,\mathrm{d}t_1 \tag{5.33}$$

which yields

$$C_{\dot{x}}^{\mathrm{det}}(\tau) = \frac{d^2\kappa^2 \exp[2\kappa T/\gamma]}{\gamma^2 T(1-\exp[\kappa T/\gamma])^2} \int_0^T \exp[-\kappa T(\mathrm{S}(t_1+\tau)+\mathrm{S}(t_1))/\gamma]\,\mathrm{d}t_1 - \frac{\kappa}{\gamma^2}\exp[-\kappa\tau/\gamma] + \frac{2}{\gamma}\delta(\tau). \tag{5.34}$$

The last two terms of the VACF correspond to the velocity autocorrelation of an overdamped harmonic oscillator and represent the interaction of the probe particle with the spring. The influence of the motor jumps enters via the first term. Since motor jumps are deterministic, the first term is a periodic function in T and does not decay to zero for $\tau \to \infty$. In contrast to the previous sections, the VACF assuming deterministic discrete motor jumps now shows significantly more structure than the single exponential decay obtained so far.

Response function

The response function for deterministic motor dynamics is calculated using Eq. (5.11) which yields

$$R_{\dot{x}}^{\mathrm{det}}(\tau) = -\frac{\kappa}{\gamma^2}\exp[-\kappa\tau/\gamma] + \frac{1}{\gamma}\delta(\tau). \tag{5.35}$$

This result is equivalent to the response function for independent motor dynamics since in both scenarios the motor is not coupled to the dynamics of the probe and is therefore not influenced by the external perturbation.

5.2.5. Simulation results and comparison with theoretical scenarios

We apply the one-state hybrid model used in the previous chapter to perform simulations of the full motor and probe dynamics. We then compare the outcomes of the simplified models developed in the previous section to the results from these simulations.

The VACF of the probe particle and the response of its velocity to an external perturbation are shown in Figs. 5.1 and 5.2, respectively. For better comparison, the squared average velocity v^2 is subtracted from all VACFs in the following sections. The parameters w^+, w^-, η and T appearing in the simplified models are chosen such that the average velocity of the simplified models matches the average velocity of the simulation. Specifically, we choose $w^+ = \langle w^+(y)\rangle$, $w^- = \langle w^-(y)\rangle$, $\eta = \Delta\mu/(vd) - \gamma$, and $T = d/v$. Note that with this choice for the rates w^+, w^-, the diffusion coefficient according to the independent motor dynamics, $d^2(w^+ + w^-)/2$,

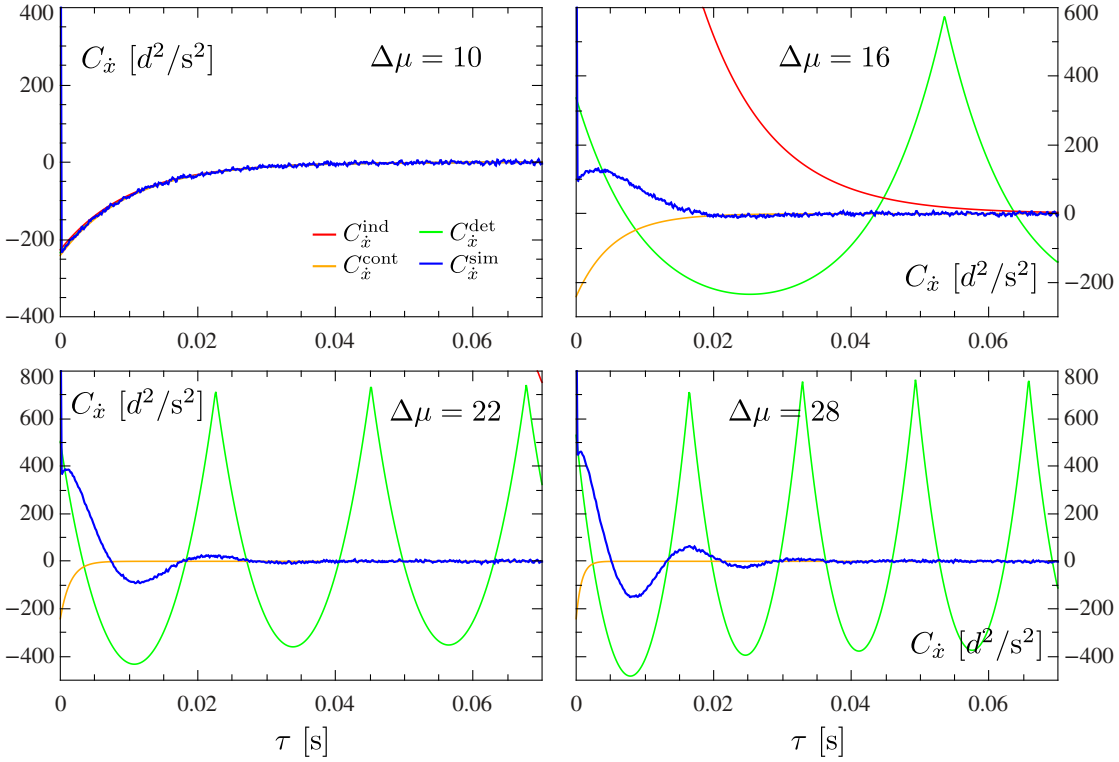

Figure 5.1.: VACF obtained from the simulations (blue) compared to the VACF using the simplified models (red, orange, green). Parameters: $\kappa = 40d^{-2}$, $\gamma = 0.407\,\mathrm{s}/d^2$, $\theta^+ = 0.1$, $w^{\mathrm{eq}} = 10^{-5}\mathrm{s}^{-1}$, $\Delta\mu = 10$, $w^+ = 0.219\mathrm{s}^{-1}$, $w^- = 0.077\mathrm{s}^{-1}$, $\eta = 7.00\mathrm{s}/d^2$, $T = 7.04\mathrm{s}$ (top left), $\Delta\mu = 16$, $w^+ = 49.29\mathrm{s}^{-1}$, $w^- = 30.61\mathrm{s}^{-1}$, $\eta = 0.449\mathrm{s}/d^2$, $T = 0.054\mathrm{s}$ (top right), $\Delta\mu = 22$ $w^+ = 7430\mathrm{s}^{-1}$, $w^- = 7383\mathrm{s}^{-1}$, $\eta = 0.068\mathrm{s}/d^2$, $T = 0.023\mathrm{s}$ (bottom left) and $\Delta\mu = 28$, $w^+ = 1.61354 \times 10^6\mathrm{s}^{-1}$, $w^- = 1.61348 \times 10^6\mathrm{s}^{-1}$, $\eta = 0.034\mathrm{s}/d^2$, $T = 0.016\mathrm{s}$ (bottom right).

is much larger than the actual effective diffusion coefficient of the motor-probe complex. Thus, the corresponding VACF is beyond the range shown in the bottom panels of Fig. 5.1.

Depending on the nucleotide concentrations, the VACF and the response function obtained from simulations exhibit two regimes [163]. Starting with small overall concentrations and small $\Delta\mu$ (top left panels in Figs. 5.1, 5.2), the VACF and the response function show an almost single exponential decay and resemble the corresponding functions of an overdamped harmonic oscillator. The physical interpretation is the same as for the model with independent motor dynamics: If jumps are rare, they hardly influence the probe dynamics which is then dominated by the restoring force of the linker. Hence, in this regime the simulation and the

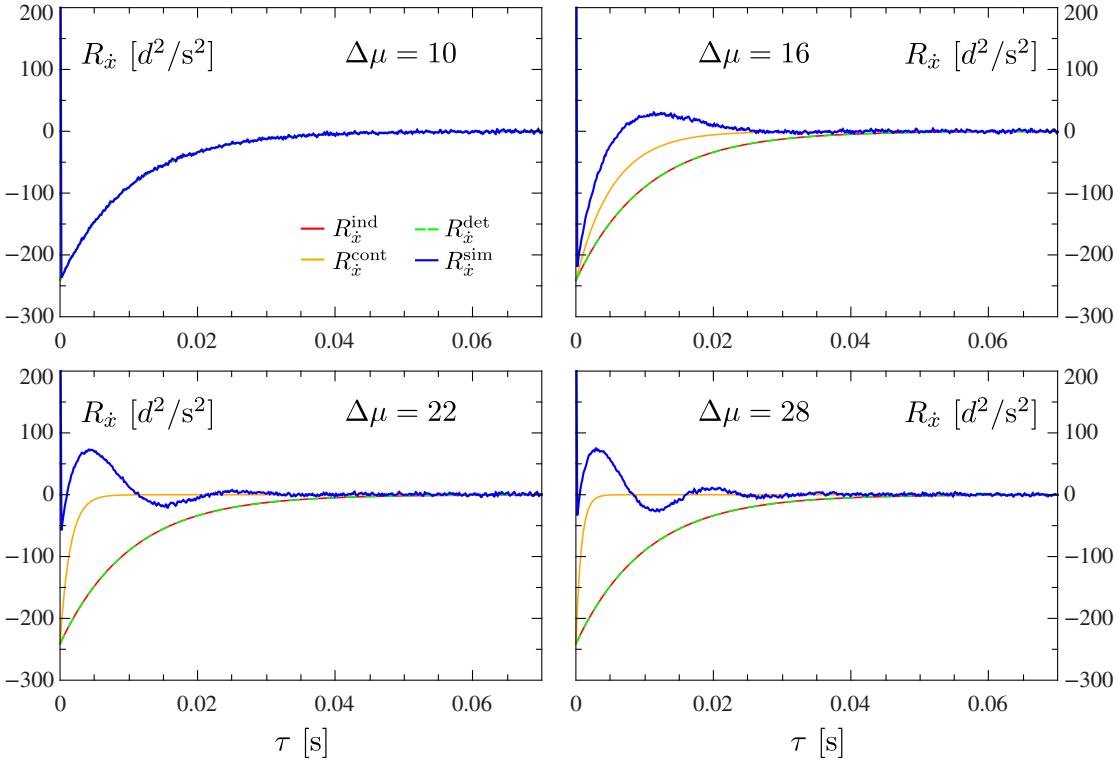

Figure 5.2.: Response function obtained from the simulation (blue) in comparison to the response functions of the simplified models (red, orange,green). Parameters as given in Fig. 5.1.

analytical results almost coincide.

Increasing the ATP concentration, i.e., increasing $\Delta\mu$ yields more forward (but also backward, induced by the stretched linker) jumps of the motor. We observe an emerging peak and finally pronounced oscillatory behavior in the VACF. For the largest $\Delta\mu$, the VACF is reminiscent of the velocity autocorrelation of an underdamped harmonic oscillator although the dynamics of the probe is purely overdamped. The oscillations result from the dynamics of the motor. If a motor jump induces a large velocity of the probe, the velocity will still be larger than its average shortly after due to the relaxation of the linker. Additionally, fluctuation-induced large velocities of the probe stretch the linker which increases the probability of a corresponding motor jump. Those induced motor jumps suddenly switch the direction of the force acting on the probe resulting in an assisting instead of a restoring force which maintains a velocity larger than the average [163]. Such interaction effects contribute to a positive correlation in the VACF for small τ. The following anticorrelation in the VACF is mostly attributed to the relaxation of the

linker. If the process starts off at $\tau = 0$ with a large velocity and stretched linker, the linker tends to relax until the velocity of the probe is smaller than its average. With decreasing y, the probability for chemically induced (forward) motor jumps rises, hence the motor is most likely to perform a successful forward jump that is not immediately followed by a backward jump when the linker has (on average) relaxed. This subsequent jump event again increases the probe velocity above its average and yields a positive correlation with the velocity compared to $\tau = 0$. These "successful subsequent events" manifest in the second peak of the VACF, which occurs at τ equal to the average time $\langle t^+ \rangle \equiv d/v$ between two successful forward jumps. The same reasoning applies if the process starts off with relaxed linker and velocity smaller than the average, then the anticorrelation is due to a jump event that increases the velocity above the average. Compared to the analytical results, the emerging oscillations follow the structure of the deterministic VACF with $T = \langle t^+ \rangle$ representing a motor dynamics that is not purely random.

The response function develops damped oscillations with increasing $\Delta\mu$ as well. In comparison to the VACF, the oscillations are less pronounced and phase-shifted but have the same frequency. Assuming a δ-like perturbation at $\tau = 0$ that shifts the probe in positive x-direction, the response function represents the deviation of the actual average velocity from the average velocity without perturbation. For larger ATP concentrations, the perturbation of the probe induces forward motor jumps resulting in a positive response of the velocity. The second peak then results from subsequent successful motor jumps after relaxation of the probe. According to the theoretical analysis in the preceding sections, a deviation from the pure relaxation process in the response function implies a coupling of the motor to the linker. For sufficiently large ATP concentrations, the additional structure is clearly visible in the simulation data.

Concerning the response function, the original perturbation applied to the probe acts on the motor only via the linker. Hence, there might be an additional "transmission time" until the perturbation causes a motor jump yielding a positive response and the onset of a subsequent relaxation process. In contrast, the occurence of motor jumps does not depend on the starting point $\tau = 0$ of the correlation function. Thus, the second peak arises at $\langle t^+ \rangle$ in the VACF whereas the response function is slightly phase-shifted.

5.2.6. Experimental observations and comparison to simulation data

The VACF of the probe as well as its response function are experimentally accessible quantities. In Fig. 5.3, we show the VACF and the response functions obtained from single-molecule experiments of the F_1-ATPase motor [15].

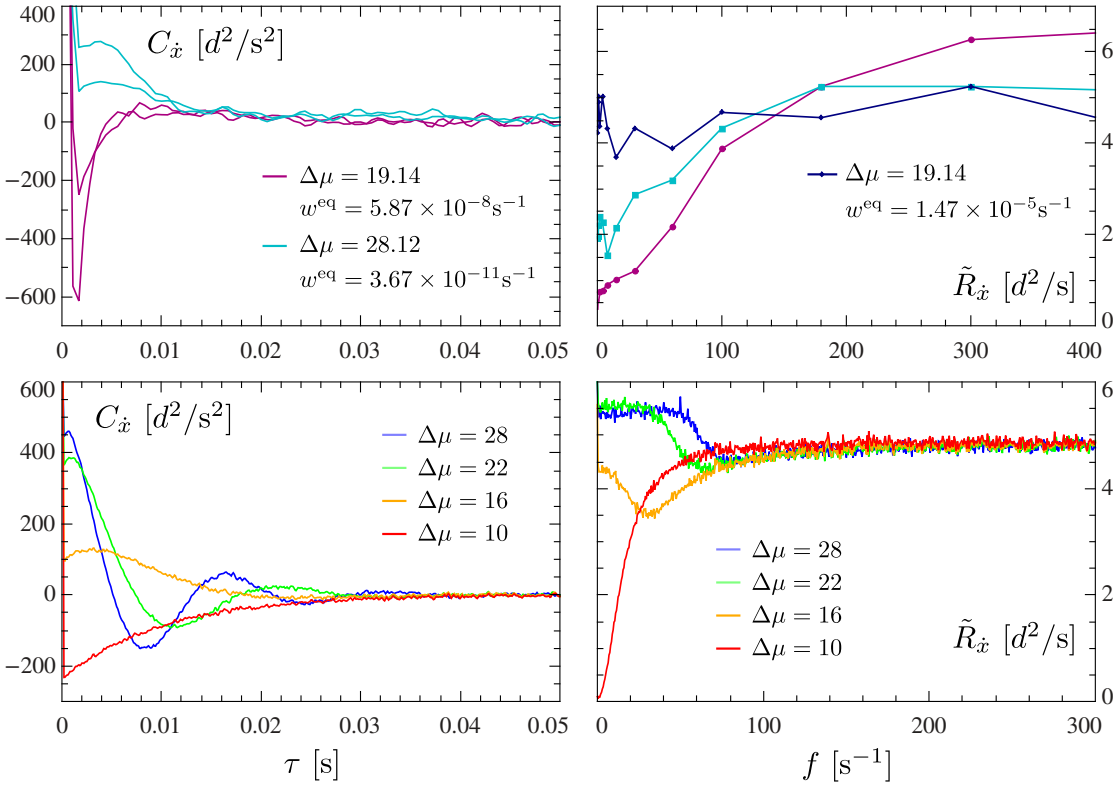

Figure 5.3.: VACF (left) and response function (right) obtained from experiments on the F_1-ATPase [15] (top) compared to simulation data (bottom). For each nucleotide concentration, the upper left panel contains the VACFs of two individual motors. The response functions are shown in the frequency domain. The correlation and response functions obtained from simulations are the same as shown in Figs. 5.1, 5.2.

Both the experimentally measured VACF and the response function show an emerging structure with increasing $\Delta\mu$ or increasing nucleotide concentrations that qualitatively agrees very well with the structure of the corresponding simulation results.

For large $\Delta\mu$ the experimentally obtained VACF clearly shows the positive correlation indicating the less random motor dynamics caused by the probe. For technical reasons, experimental data concerning the response function is available only in the frequency domain. A single exponential decay corresponds to a Lorentzian function in the frequency domain. The slight deviation of the Fourier transformed response function $\tilde{R}_{\dot{x}}$ from the Lorentzian function for small f present in the experimental data is similar to the structure observed in the simulation results. Thus, this deviation might be interpreted as sign of the coupling of the

motor to the probe.

While the structure of the experimental data agrees very well with the simulation results, it emerges at rather different nucleotide concentrations and is, in general, less pronounced than in the simulation. Two effects might contribute to the weaker oscillatory behavior of the VACF and the response function in the experiments. First, the steep decay of the VACF at $\Delta\mu = 19.14$ indicates a larger spring constant κ than previously attained from fitting the average velocity. For large spring constants, the VACF is dominated by the restoring force of the linker. Second, the one-state motor with a harmonic linker is obviously not sufficient to cover the complexity of a real motor protein as already mentioned in the previous chapter. Since a one-step motor has a single fixed step length, its simulation results might appear much more deterministic than for a motor with substeps of different length whose contributions would superpose in the VACF.

In the experimental setup, the explicit linker potential is not known. The potential generated by streptavidin and biotin bonds is presumably more complex than a harmonic potential. One has to take into account that the shape of the experimentally obtained VACF and response function strongly depends on the actual linker potential.

5.3. Dwell-time distribution

As mentioned in the introduction of this chapter, the distribution of dwell times between consecutive (forward) motor jumps is not just a single exponential decay when the motor is coupled to a probe particle. Typically, the dwell-time distribution of a motor-probe complex exhibits a distinct peak [135, 159]. Such a distribution belongs to a non-Markovian process and is usually attributed to hidden intermediate states of the motor [74, 87, 164, 165]. In the case of a motor-probe complex, a peaked distribution can be obtained even for a one-state motor model with (for fixed y) Poissonian rates, see Fig. 5.4. The non-Markovian structure emerges since the motor rates depend on the position of the probe. Right after a jump, the linker is elongated and hence consecutive jumps in the same direction are suppressed. For large dwell times, when the probe has relaxed, the transition rate of the motor $w^+(y)$ becomes nearly constant and one observes a Poissonian process. Consequently, in the intermediate regime, the dwell-time distribution exhibits a peak. Here, the usually assumed intermediate states correspond to the relaxation process of the probe. Note that since jumps can occur for any y, the number of "intermediate states" is not fixed for the motor-probe complex. While the full motor-probe model is truly Markovian, the dwell-time distribution as obtained in experiments and shown in Fig. 5.4, is implicitly averaged over y and constitutes a coarse-grained view on the motor dynamics. Such coarse-graining

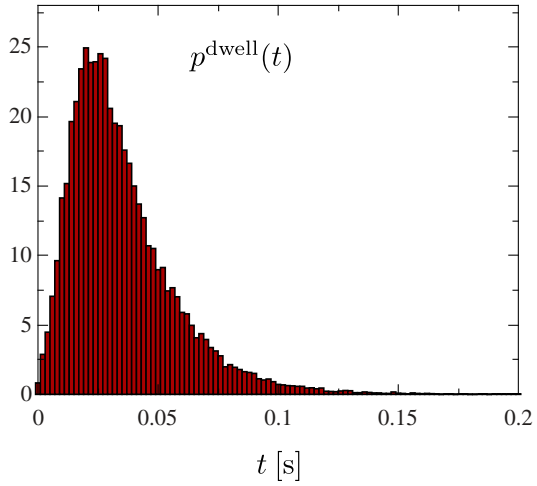

Figure 5.4: Dwell-time distribution for forward jumps of the motor obtained from the simulation of the one-state motor-probe model for the F_1-ATPase. For this histogram, 26328 forward jumps following forward or backward jumps were evaluated. Parameters: $\kappa = 40$, $\gamma = 0.407\,\mathrm{s}/d^2$, $\theta^+ = 0.1$, $\Delta\mu = 28.12$, $w^{\mathrm{eq}} = 3.67 \times 10^{-11}\,\mathrm{s}^{-1}$.

typically yields a non-Markovian dynamics.

A dwell-time distribution with a distinct peak represents a dynamics that is less random than a pure random walk. Concerning the motor-probe complex, this observation is consistent with the results from the analysis of the VACF and response function.

Extracting information from experimentally measured dwell-time distributions is a delicate issue. The dwell-time distribution of the motor jumps is typically reconstructed from the trajectory of the probe which can miss many fast forward and backward motor jumps. If one observes differently shaped dwell-time distributions for different motor steps [74, 87, 166], one has to consider that dwells following large steps are presumably more influenced by the probe than dwells following short steps. For dwells following steps with similar step size, the influence of the probe compared to intermediate motor states can be estimated from the distribution that is most similar to a single exponential decay since then the influence of the probe on the dwell time is the same.

5.4. Conclusion

In this chapter, we have investigated the influence of the probe on the dynamics of the motor on the basis of the VACF and the response function of the velocity of the probe and the dwell-time distribution of the motor jumps. We find that for small nucleotide concentrations the VACF and the response function obtained from simulations of the hybrid model resemble the VACF and response of a harmonic oscillator. With increasing ATP concentration, the VACF as well as the response function develop pronounced oscillatory behavior.

We have introduced three simplified analytically tractable hybrid models providing insights into the origin of the oscillatory structure observed in the simulations. Regarding these simplified models, we find that any physical model that fulfills the FDT in equilibrium must comprise symmetric coupling between motor and probe.

For a harmonic linker potential, the analytical analysis clearly shows that neither discrete motor jumps at random times nor coupling of the (continuously moving) motor to the probe alone are sufficient to generate velocity correlations of the probe particle that exhibit more structure than a purely exponential decay. Only a motor model that comprises discrete motor jumps that are not purely random leads to a periodic structure in the VACF of the probe particle. Since the periodic structure also emerges in the simulation data, we can conclude that coupling to the probe causes the motor to move less randomly. The analysis of the response function provides insight about the coupling of the motor to the linker. Additional structure beyond the restoring force of the linker emerges only if the perturbation originally applied to the probe is transmitted to the motor. Our simulation results illustrate that such effects are clearly visible in the response function of the probe particle.

The analysis has been performed using a harmonic linker potential, whereas the actual linker potential in the experiments is presumably more complex. We do not expect, however, that any convex potential can mimic positive correlation or even oscillatory behavior of the VACF and the response function.

Analyzing the structure of experimentally obtained VACFs of the probe particle therefore allows to infer properties of the underlying dynamics of the motor and its coupling with the probe particle. We find that experimentally obtained VACFs and response functions of the F_1-ATPase qualitatively agree with the simulation results. Quantitative discrepancies are most likely due to the complexity of the actual motor and the linker protein as well as additional effects from the setup that are not captured in our simple motor-probe model.

Investigation of the waiting-time distribution provides additional insight concerning the origin of the deterministic characteristics of the motor dynamics. Subsequent motor jumps in the same direction are suppressed by the delayed relaxation of the probe yielding a peaked dwell-time distribution. Ignoring the influence of the probe, the non-Markovian structure could be mistaken as signature of hidden intermediate motor states thus leading to an overly complex motor model.

6. Energy transduction mechanism and stall force anomaly

6.1. Introduction

While the preceding chapters focused on the effects of the probe on the dynamics of the motor, we will now address the energy transduction mechanism of the motor. Experimentally, information about the energy transduction is obtained from applying external forces to the probe and investigating the resulting average velocity [77, 99]. The system reaches stall conditions when the average velocity is zero. Hence, the stall force corresponds to the maximum work per motor step that can be extracted from the system on average. Properties of the energy transduction mechanism of the motor are then usually inferred by comparing the work corresponding to the stall force with the available chemical energy per hydrolysis event [77, 99].

In this chapter, we investigate to what extend the probe particle influences the energy conversion of the motor. Specifically, we investigate the stall conditions and compare the cases when an external force is applied to the probe or directly to the motor in the absence of a probe particle. We find that the stall conditions depend on the relaxation time of the probe. Since the stall force is a quantity determined in many single-molecule measurements, it is important to be aware of the modifications caused by the probe.

The effects of the probe particle on the energy transduction under NESS conditions can be nicely presented using elements of network theory. Network theory is a powerful tool for investigating stochastic biophysical processes. Basic information and applications can be found in, e.g., [29, 47, 167–169]. Therefore, we will first present the network representation of the hybrid model introduced in section 3.3. We then discuss the modification of the energy transduction mechanism on the basis of a very simple motor-probe network. Finally, we provide numerical results for specific hybrid models with continuous state space of the probe.

6.2. Network representation

For some purposes, it is instructive to discretize the state space of the probe yielding a fully discrete model. The probe particle then moves on a set of states separated by $\delta \leq d$ with transition rates $\gamma^{\pm}(n, x)$. The transition rates of the probe obey

$$\frac{\gamma^{+}(y)}{\gamma^{-}(y-\delta)} = \exp[-V(y-\delta) + V(y) - f_{\mathrm{ex}}\delta] \tag{6.1}$$

with the external force f_{ex} acting on the probe. The corresponding master equation of such a discrete model is given by the discretized version of (3.12),

$$\begin{aligned}\partial_t p_i(y) = {} & p_i(y-\delta)\gamma^{-}(y-\delta) + p_i(y+\delta)\gamma^{+}(y+\delta) - p_i(y)(\gamma^{+}(y) + \gamma^{-}(y)) \\ & + \sum_{j,\alpha} \left(p_j(y + d_{ij}^{\alpha}) w_{ji}^{\alpha}(y + d_{ij}^{\alpha}) - p_i(y) w_{ij}^{\alpha}(y) \right).\end{aligned} \tag{6.2}$$

If we keep δ finite and allow a maximal distance y between motor and probe, we get a a finite number of states which are characterized by the motor state i and the distance y between motor and probe. The state space of these (i, y)-states is represented by a network where the nodes are the states and the edges correspond to the transition rates. An example for the network of such a discretized system comprising motor and probe particle is shown in Fig. 6.1.

In general, such motor-probe networks comprise several cycles. A cycle is a sequence of transitions that ends in its starting state and passes each intermediate

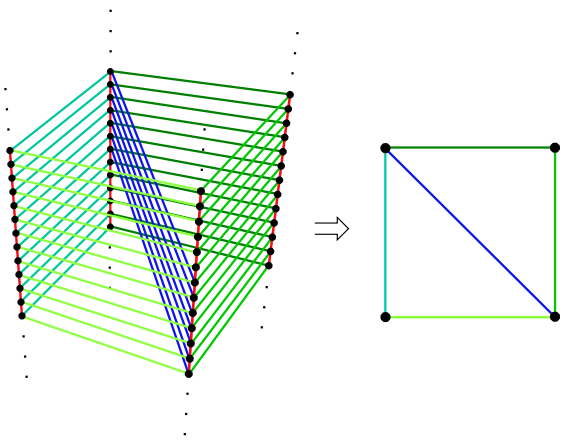

Figure 6.1: Network representation of a motor-bead model with four internal motor states and discretized state space of the probe particle (left) [137]. Each row of black dots represents one motor state while the dots themselves represent specific distances y accessible to the probe particle (via the red lines) within the same motor state. Transitions between motor states either leave y the same (green lines) or can advance the motor by d and change y (blue lines). The top view of this network corresponds to the bare motor network (right). ©2015 American Physical Society.

state only once. The cycles a of the full system on the $z \equiv (i, y)$ state space can comprise various combinations of motor cycles. Each cycle a is assigned a reference orientation. Then, in the NESS, the average current passing a cycle in forward $(+)$ or backward $(-)$ direction is given by [47]

$$J_a^{\pm} = \frac{\sigma_a}{\Sigma} \left[\prod_{z \in a} k_a^{\pm}(z) \right], \tag{6.3}$$

where $k_a^{\pm}(z)$ represents either $w_{ij}^{\alpha}(y)$ or $\gamma^{\pm}(y)$, the explicit sequence depends on the cycle a and the direction. The sum of all directional diagrams [47] of all states in the network is called Σ and the sum of influx into the cycle a is denoted by σ_a. The net current flowing through the cycle a is given by

$$J_a = J_a^+ - J_a^-. \tag{6.4}$$

The directed cycle currents obey

$$\frac{J_a^+}{J_a^-} = \prod_{z \in a} \frac{k_a^+(z)}{k_a^-(z+1)} = \exp[\Delta S_a] = \exp[\Delta \mu_a - f_{\mathrm{ex}} d_a], \tag{6.5}$$

where ΔS_a, $\Delta \mu_a$ and d_a are the entropy change or cycle affinity [168], free-energy change of the solvent and the motor step associated with a cycle passage. Contributions of the potential $V(y)$ cancel since the cycles start and end at the same y.

The average current that is defined along an individual edge between two neighboring states is called transition current [47], see also Eq. (2.7). In the NESS, each transition current can be expressed as a sum of cycle currents passing through the respective edge, e.g.,

$$j_{ij}^{\alpha}(y) \equiv p_i(y) w_{ij}^{\alpha}(y) - p_j(y + d_{ij}^{\alpha}) w_{ji}^{\alpha}(y + d_{ij}^{\alpha}) = \sum_{a \ni (i,j,\alpha,y)} \pm J_a, \tag{6.6}$$

where the sign of J_a depends on the orientation of the cycle a relative to the transition (i, j, α, y). Hence, any current observable can be expressed in terms of transition currents or cycle currents.

The least detailed view of the dynamics on a network is provided by operational currents which typically correspond to the change of a (macroscopic) observable [47]. Several transition currents can contribute to an operational current. In the context of motor-probe networks, the operational current between motor state i and motor state j is the sum of all y-dependent net transition currents that contribute to the transition $i \to j$,

$$j_{ij}^{\alpha} \equiv \sum_y j_{ij}^{\alpha}(y) = \sum_y \sum_{a \ni (i,j,\alpha,y)} \pm J_a. \tag{6.7}$$

The average velocity can then be calculated by summing over all mechanical transitions with $d_{ij}^{\alpha} \neq 0$,

$$v = \sum_{i,j,\alpha,y} \left(p_i(y) w_{ij}^{\alpha}(y) - p_j(y + d_{ij}^{\alpha}) w_{ji}^{\alpha}(y + d_{ij}^{\alpha}) \right) d_{ij}^{\alpha} = \sum_{i,j,\alpha} j_{ij}^{\alpha} d_{ij}^{\alpha}. \tag{6.8}$$

Considering the specific example in Fig. 6.1, all transition currents along the blue edges contribute to the velocity. Thus, the velocity is simply given by $v = j_{ij}^{\text{blue}} d = d \sum_y j_{ij}^{\text{blue}}(y)$.

6.3. Stall conditions of the motor-probe complex

6.3.1. Bare motor models

As mentioned above, the stall force corresponds to the maximum work per step that can be extracted from a molecular motor on average and is limited by the chemical energy input. If one considers only the motor without probe and assumes that the force is applied directly to the motor, one can distinguish two classes of motor networks. For networks that contain only one cycle (unicyclic motors) the stall force equals the chemical free-energy input $f_{\text{ex}}^{\text{st}} = \Delta\mu_{\text{cycle}}/d_{\text{cycle}}$ which can be seen easily using Eq. (6.5) [38]. Hence, unicyclic motors can convert the full $\Delta\mu_{\text{cycle}}$ into extractable work, however, only at vanishing average velocity.

For networks comprising several cycles (multicyclic motors), the chemical input and the mechanical output transitions are often only loosely coupled. Hence, as soon as there are cycles that waste chemical energy but do not contribute to a forward step, the output power will be smaller than the input power.

6.3.2. Unicyclic motors

The network of a motor-probe system with a unicyclic motor as sketched in Fig. 6.2 typically comprises several cycles on the z state space. Each such system cycle includes either the complete motor cycle or is a so-called zero-cycle, a cycle that involves an even number of $i, i+1$ transitions with opposite directions for all involved motor states i and $i+1$. Thus, a zero-cycle leads neither to net displacement nor to net consumption of energy. According to Eqs. (6.4, 6.5), every zero-cycle has zero entropy production (or affinity) and zero net current. Due to the topology of the network, there are no system cycles that include the motor cycle more than once.

In order to obtain the stall force, one has to determine the zeros of the operational currents corresponding to the mechanical transitions, which are the sum of

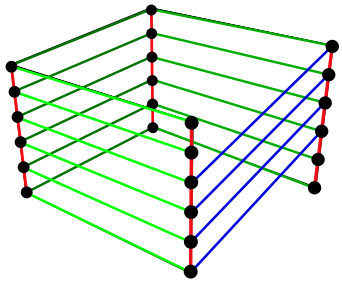

Figure 6.2: Network representation of a motor-probe model with a unicyclic motor. The motor has four internal states, three chemical/conformational transitions (green) and one mechanical transition (blue). The motor network of unicyclic motors with more than two states has only one single link between states i, $i+1$.

all transition currents of the involved transitions (see (6.8)). Each transition current is the sum of all cycle currents passing through the transition, see (6.6). Cycles that include several forward and backward jumps or zero-cycles use one transition pathway from i to $i+1$ in forward direction and another one in backward direction from $i+1$ to i. Therefore, their cycle currents appear in the corresponding transition currents with opposite sign. By summing all transition currents, at most one contribution per cycle remains (the contributions from the zero-cycles cancel out). Since every remaining cycle has to pass every i, after the summation each operational current $j^{\alpha}_{i,i+1}$ contains exactly one contribution from each cycle current whose cycle includes the complete motor cycle and can be written as [1]

$$j^{\alpha}_{i,i+1} = j^{\beta}_{i+1,i+2} = \sum_a \pm J_a \qquad \forall i. \tag{6.9}$$

Using Eq. (6.5), we find that the zero of all remaining J_a occurs for $f_{\rm ex} d_{\rm cycle} = \Delta\mu_{\rm cycle}$ which determines the stall force. Thus, for unicyclic motors, the stall force corresponding to the motor-probe complex equals the stall force of the bare motor.

The fact that each cycle current J_a is zero at the stall force $f^{\rm st}_{\rm ex} = \Delta\mu_{\rm cycle}/d_{\rm cycle}$ implies that each transition current in the network is zero at stall individually. The solution of Eq. (6.2) at stall is then given by a "shifted" Boltzmann distribution

$$p^{\rm st}_i(y) = P^{\rm st}_i \exp[-V(y) + f^{\rm st}_{\rm ex} y]/\mathcal{N} \tag{6.10}$$

with $\mathcal{N} = \sum_y \exp[-V(y) + f^{\rm st}_{\rm ex} y]$ and marginal distributions $P^{\rm st}_i$ that are uniquely determined by

$$\frac{P^{\rm st}_{i+1}}{P^{\rm st}_i} = \exp[-\Delta F^{\alpha}_{i,i+1} - f^{\rm st}_{\rm ex} d^{\alpha}_{i,i+1}] \tag{6.11}$$

with $\Delta F^{\alpha}_{i,i+1}$ as defined in Eq. (3.8). For unicyclic motors, the probability distribution at stall conditions is given by the shifted Boltzmann distribution (6.10) irrespective of the specific form of the function $\phi^{\alpha}_{ij}(y)$ (3.10, 3.11) that accounts for a possible y-dependence of the chemical/configurational rates.

[1] For unicyclic motors, the index α is redundant unless the motor has only two internal states linked via two transitions to form the cycle.

6.3.3. Multicyclic motors

For multicyclic motors, cycles on the state space of the full system may involve several motor cycles. An example for such a situation is shown in Fig. 6.3. While the motor network (right panel) consists of two separate cycles, the motor-probe network contains cycles that include both motor cycles (center).

Since the two motor cycles are separate, the stall force of the bare motor is given by $f_{\mathrm{ex}}^{\mathrm{st}} = \Delta\mu/d$ where the cycle current corresponding to the cycle (I II I) vanishes. Considering the system with probe particle, one has to obtain the zero of the operational current $j_{\mathrm{I,II}}$ along the blue edge, which is equal to the transition current j_{15} in this network. The system cycles (1521), (1561), (15b43b21), (15f43f21), (15b43f21) (purple) and (15f43b21) (cyan) contribute to j_{15} where b and f indicate that the pathway in the background (dark green) or in the foreground (light green) is used. The first four cycles have the affinity $\Delta\mu - f_{\mathrm{ex}}d$ while the latter two have affinity $-f_{\mathrm{ex}}d$ and $2\Delta\mu - f_{\mathrm{ex}}d$, respectively. Thus, at $f_{\mathrm{ex}} = \Delta\mu/d$, the current j_{15} has a positive contribution from the cyan cycle in Fig. 6.3 and a negative one from the purple cycle. Depending on the explicit values of the transition rates, the stall force this model can be smaller, equal to or even larger than $\Delta\mu$. Numerical investigation indicates an "optimal" probe size where the deviation of the stall force from the stall force of the bare motor is maximal.

For such motor models with separate cycles, the stall force of the motor-probe complex can deviate from and even exceed the stall force of the bare motor if additional chemical energy is accessible via, e.g., an idle cycle of the motor. In that case, the idle cycle is no longer idle but takes part in the energy transduction since it can be accessed by system cycles. Thus, applying the external force at

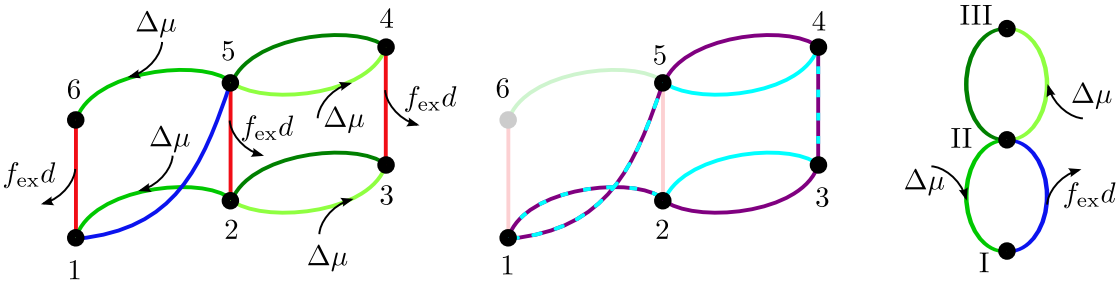

Figure 6.3.: Network representation of a motor-probe complex with three motor states and only two admissible linker configurations y, i.e., $\delta = d$. The horizontal (and diagonal) edges correspond to motor transitions, vertical edges indicate transitions of the probe. Left panel: motor-probe network with corresponding chemical input and work output. Center: Two distinct system cycles spanning both motor cycles. Right: Network of the bare motor assuming the force acts directly on the motor.

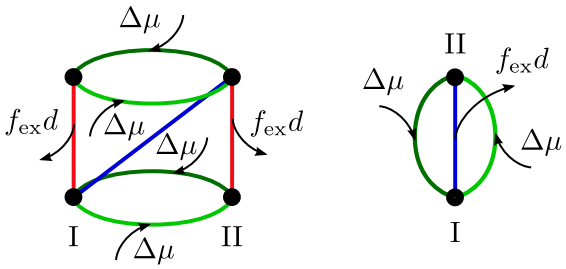

Figure 6.4: Network representation of a motor-probe model with two motor states and two accessible linker configurations, i.e., $\delta = d$. The motor network involves three cycles. Each cycle on the network of the full system comprises only one of the motor cycles.

the probe can be used to increase the maximum extractable work from the motor compared to the situation where the force is applied directly to the motor.

For the model discussed above, the modification of the stall force is caused by system cycles that include several motor cycles. Note that for multicyclic motor models, a variation of the stall force can also occur if system cycles contain only one motor cycle but the transition current(s) corresponding to the velocity have contributions from several motor cycles. Such a network in shown in Fig. 6.4.

A more detailed analysis of the two models shown in Figs. 6.3 and 6.4 reveals that for both networks the distribution at stall conditions, $p_i^{\rm st}(y)$, takes the form of (6.10) only if there is a specific symmetry in the y-dependence of the chemical/conformational rates. In particular, $\phi^f_{\rm II,III}(y) = \phi^b_{\rm II,III}(y)$ for the model in Fig. 6.3 and $\phi^f_{\rm I,II}(y) = \phi^b_{\rm I,II}(y)$ for the model in Fig. 6.4. The stall force of the motor-probe complex is then given by

$$f_{\rm ex}^{\rm st} = \Delta\mu/d \qquad \text{and} \qquad f_{\rm ex}^{\rm st} = \left(\Delta\mu + \ln\frac{k^f_{\rm I,II}\exp[-\Delta\mu] + k^b_{\rm I,II}}{k^f_{\rm I,II}\exp[\Delta\mu] + k^b_{\rm I,II}}\right)/d, \tag{6.12}$$

respectively. The attempt frequencies $k^{f,b}_{\rm I,II}$ of the model in Fig. 6.4 correspond to transitions from motor state I to II using the horizontal links in the background (b) or in the foreground (f). With this choice of $\phi^\alpha_{ij}(y)$, the stall force becomes independent of the friction coefficient γ and the linker potential $V(y)$ and equal to the stall force of the bare motor for both models.

The same reasoning presented above for the variation of the stall force with probe size also applies for the rate of chemical energy consumption. The augmented motor-probe network will in general also comprise cycles that contribute to the overall hydrolysis rate and make the rate of chemical energy consumption a function of the probe.

In general, the results obtained in this section are not restricted to the case $\delta = d$ but apply to any discretization of the dynamics of the probe. The next section provides two examples in the continuum limit.

6.4. Examples: F_1-ATPase and kinesin

The general findings discussed in the previous section can be illustrated with numerical results obtained from hybrid models with continuous state space of the probe as introduced in chapter 3. The two-state model for the F_1-ATPase introduced in section 3.3, see Fig. 3.3, serves as an example for a unicyclic motor model. A multicyclic motor is represented by the well-studied 6-state-model for kinesin introduced in [28], see Fig. 6.5. Implementing the probe particle and an elastic linker $V(y)$, we adopt the transition rates of the motor from [28] and replace the dependence on the external force by the dependence on the elongation of the linker,

$$w^+_{25}(y) = k_{25}\exp[-V(y+d\theta^+)+V(y)], \tag{6.13}$$
$$w^-_{52}(y) = k_{52}\exp[-V(y-d\theta^-)+V(y)], \tag{6.14}$$
$$w^+_{ij,\mathrm{chem}} = k_{ij}\phi_{ij}(y)\exp[\mu^+_{ij}], \tag{6.15}$$
$$w^-_{ji,\mathrm{chem}} = k_{ji}\phi_{ij}(y)\exp[\mu^-_{ij}], \tag{6.16}$$

with $\phi_{ij}(y) = 2/(1+\exp[\partial_y V(y)\chi_{ij}])$. The first two rates belong to the mechanical transition, the lower two rates represent the chemical transitions which depend on the instantaneous force exerted by the linker with a chemical load-sharing factor χ_{ij}, see [28]. The change of chemical free energy $\mu^\pm_{ij} = \mu_\mathrm{T}, \mu_\mathrm{D}, \mu_\mathrm{P}$ depends on which transition involves binding of the corresponding nucleotide. We choose again $V(y) = \kappa y^2/2$.

The average velocity as a function of the external force is shown in Fig. 6.6. From red to blue/violet, the size of the probe decreases yielding a faster relaxation.

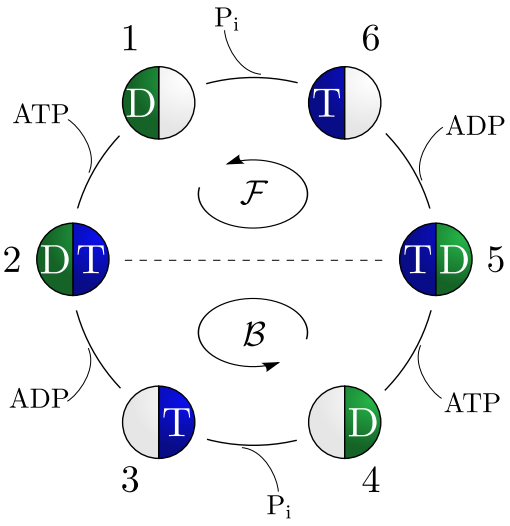

Figure 6.5: 6-state-model representing a kinesin motor adapted from [28]. The transition between states 2 and 5 is purely mechanical and corresponds to a step of length d whereas all other transitions are pure chemical transitions. The motor model includes three cycles: $\mathcal{F}$, which, in the + direction, includes ATP hydrolysis and forward stepping; $\mathcal{B}$, which includes ATP hydrolysis and backward stepping in its + direction; and a pure chemical cycle (around the circle) that includes hydrolysis or synthesis of two ATP [137]. ©2015 American Physical Society.

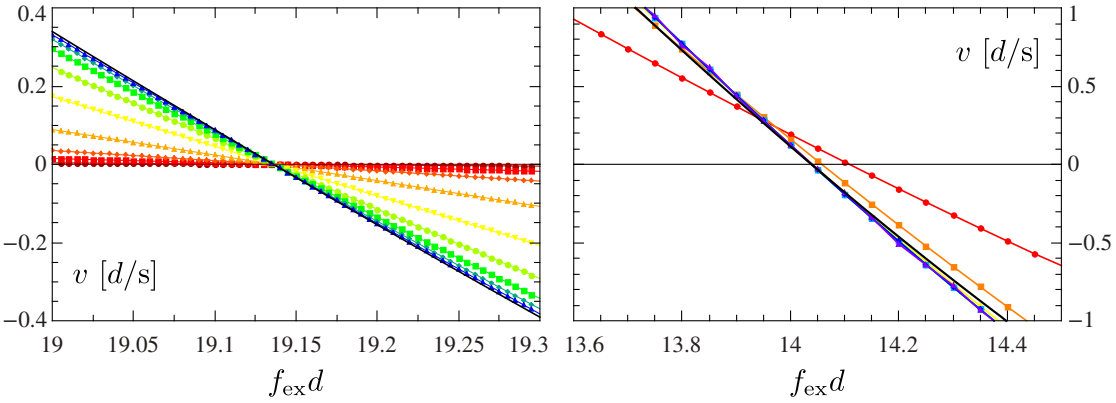

Figure 6.6.: Average velocity as a function of the external force applied at the probe. Left: Data obtained from the F_1-ATPase model for various friction coefficients γ in the range $5\text{s}/d^2 \geq \gamma \geq 5 \times 10^{-8}\text{s}/d^2$ (from red to blue) Parameters: $c_\text{T} = c_\text{D} = 2\mu\text{M}$, $c_\text{P} = 1\text{mM}$, $\theta^+_{90,30} = 0.1$, $k^{90}_{12} \exp[\mu^{\text{eq}}_\text{T}]/c^{\text{eq}}_\text{T} = 3 \times 10^7(\text{Ms})^{-1}$, $k^{90}_{21} \exp[\mu^{\text{eq}}_D]/c^{\text{eq}}_\text{D} = 3667.5(\text{Ms})^{-1}$, $k^{30}_{21} = 1000\text{s}^{-1}$, $k^{30}_{12} \exp[\mu^{\text{eq}}_P]/c^{\text{eq}}_\text{P} = 40(\text{Ms})^{-1}$. The attempt frequencies are chosen on the basis of [74, 87] where very small probe particles have been used. Right: Data obtained from the kinesin model for γ in the range $0.077\text{s}/d^2 \geq \gamma \geq 7.7 \times 10^{-10}\text{s}/d^2$ (from red to violet). Parameters: $\kappa = 10d^{-2}$ [99], $c_\text{T} = 1\text{mM}$, $c_\text{D} = c_\text{P} = 1\text{nM}$ (estimated), $\theta^+ = 0.65$, $\chi_{ij} = 0.25, 0.15$, $k_{12} \exp[\mu^{\text{eq}}_T]/c^{\text{eq}}_\text{T} = k_{45} \exp[\mu^{\text{eq}}_T]/c^{\text{eq}}_\text{T} = 2 \times 10^6(\text{Ms})^{-1}$, $k_{21} = k_{23} = k_{34} = k_{56} = k_{61} = 100\text{s}^{-1}$, $k_{32} \exp[\mu^{\text{eq}}_D]/c^{\text{eq}}_\text{D} = k_{65} \exp[\mu^{\text{eq}}_D]/c^{\text{eq}}_\text{D} = 2 \times 10^4(\text{Ms})^{-1}$, $k_{43} \exp[\mu^{\text{eq}}_\text{P}]/c^{\text{eq}}_\text{P} = k_{16} \exp[\mu^{\text{eq}}_\text{P}]/c^{\text{eq}}_\text{P} = 2\times10^4(\text{Ms})^{-1}$, $k_{25} = 3\times10^5\text{s}^{-1}$, $k_{52} = 0.24\text{s}^{-1}$, $k_{54} = (k_{52}/k_{25})^2 k_{21}$ [28]. In both cases, the solid black line corresponds to the bare motor with external force applied directly to it.

The black lines correspond to the bare motor model with force applied directly to the motor. For the F_1-ATPase, the stall force is the same for all sizes of the probe. The nucleotide concentrations have been chosen such that $\Delta\mu = 19.14$ which is precisely the observed stall force. With decreasing probe size, the velocity approaches the bare-motor solution.

The stall force of the kinesin model depends on the size of the probe and is much smaller than $\Delta\mu = 46.8$. Varying the size of the probe, the relative weight of the cycles in the full system and hence their contribution to an operational current can change yielding a varying stall force. Thus, the experimentally obtained stall force corresponds to the stall conditions of the motor-probe complex but does not necessarily represent the stall conditions of the bare motor. If one is interested in the latter one should use very small probe particles since the limit of vanishing friction coefficient γ is equivalent to applying the force directly to the motor (see sections 7.2.3 and 7.3.2). Note that the actual stall force of the kinesin-probe

complex is indeed larger than the stall force of the bare kinesin motor.

Since the stall force is independent of γ for all unicyclic motors, an experimentally observed variation of the stall force with probe size can be used as proof that the motor is indeed multicyclic.

6.5. Stall force and thermodynamic efficiency

In the context of multicyclic motors, inferring properties of the energy transduction mechanism of the motor from the stall force is a delicate issue. In the previous section we have focused on the dependence of the stall force on the size of the probe particle. In this section, we discuss an aspect that applies also for bare motor models with external force applied directly to the motor.

The genuine thermodynamic efficiency is defined as [132, 155]

$$\eta_{\mathrm{T}} \equiv \frac{\dot{W}_{\mathrm{out}}}{\dot{\Delta\mu}} \tag{6.17}$$

where the output power is given by $f_{\mathrm{ex}} v$ while the rate of chemical energy consumption constitutes the input power $\dot{\Delta\mu} = \sum_{i<j,\alpha} j_{ij}^{\alpha} \Delta\mu_{ij}^{\alpha} = \sum_a J_a \Delta\mu_a$. Since each cycle comprises complete hydrolysis or synthesis events, the rate of chemical energy consumption is denoted by $\dot{\Delta\mu} = r\Delta\mu$ with the hydrolysis rate r.

At stall conditions, the average velocity vanishes. If the hydrolysis rate equals the velocity, which is the case for tightly coupled motors, the thermodynamic efficiency reaches 1 at stall. However, multicyclic motors typically comprise idle cycles yielding a non-zero r at stall and vanishing thermodynamic efficiency [132]. It is essential to always compare the rate of extracted work with the actual rate of chemical energy consumption instead of the extracted work per step, $f_{\mathrm{ex}} d$, and the available energy per hydrolysis event, $\Delta\mu$. Considering the bare motor model shown in Fig. 6.3, right panel, the maximum extracted work is given by $f_{\mathrm{ex}}^{\mathrm{st}} d = \Delta\mu$. However, there is an idle cycle wasting additional $\Delta\mu$ which does not contribute to the cycle involving the mechanical transition. The thermodynamic efficiency of this model is zero at stall instead of 1 what one would have naively expected from $f_{\mathrm{ex}}^{\mathrm{st}} d = \Delta\mu$. Hence, measuring $f_{\mathrm{ex}}^{\mathrm{st}} d = \Delta\mu$ neither implies that the full chemical energy is converted nor that the motor has no idle cycles.

Moreover, depending on how many ATPs are used to perform a forward step (on average), the stall force, even of the bare motor, can easily exceed $\Delta\mu/d$. Thus, the observation of $f_{\mathrm{ex}}^{\mathrm{st}} d > \Delta\mu$ is not in conflict with the second law since a single $\Delta\mu$ does not necessarily represent the complete energy input.

Related to this issue is a result from [128], where idle cycles have to be present if the discretized slope in the fluctuation theorem representation deviates from

$\Delta\mu - f_{\mathrm{ex}}d$ but not vice versa. Hence, the motor can have idle cycles that do not show up in the fluctuation theorem for an effective displacement by d.

6.6. Conclusion

In this chapter, we have analyzed the influence of the probe particle on the energy transduction mechanism of the motor. We have introduced the network description of the hybrid models and have applied tools from network theory to investigate especially the stall conditions of the motor-probe complex.

We find that for unicyclic motors, the energy conversion process is not altered by the probe and the extracted work per step under stall conditions is always equal to the total chemical energy input like for the bare motor. At stall conditions, the stationary distribution of hybrid models with unicyclic motors is given by a shifted Boltzmann distribution. In contrast, hybrid models with a multicyclic motor can exhibit stall forces that are smaller, equal to or even larger than the stall force of the bare motor. The modification of the stall force occurs since the motor-probe network contains more cycles that contribute to the mechanical transitions than the bare motor network. Varying the size of the probe, the relative weight of the cycles in the full system and hence their contribution to an operational current can change yielding a varying stall force.

The most striking result of our analysis is the finding that applying a probe particle can be used to increase the maximum extractable work from the motor. Note that typically also the energy consumption rate changes with the size of the probe yielding a higher energy conversion rate but not necessarily a higher efficiency.

Considering experiments, it is crucial to keep in mind that the observed stall force corresponds to the motor-probe complex rather than to the bare motor. Applying naively a one-particle model to such an experimental setup would not allow us to determine the energy transduction mechanism of the motor correctly. The stall force of the bare motor can be best approximated by using probe particles that are as small as possible. The analysis of the stall force as a function of the probe size provides the useful application that observing a varying stall force with the size of the probe serves as a proof that the investigated motor is multicyclic.

Note that stall forces $f_{\mathrm{ex}}^{\mathrm{st}} = \Delta\mu/d$ neither imply that the motor can convert the full chemical energy nor that it has no idle cycles. The total input power can be much larger running idle cycles that are separate from the step cycle and hence not “visible”. Thus, a stall force larger than $\Delta\mu$ is not in conflict with the second law.

7. Thermodynamically consistent coarse-graining method

7.1. Introduction

While multiparticle models are more precise and better represent the actual experimental setup, one-particle models are widely used toy models often applied to illustrate basic ideas.

Simplifying the description of systems consisting of many degrees of freedom with a concomitant large state space while still maintaining important properties is commonly known as coarse-graining. In the context of stochastic thermodynamics [6], various coarse-graining methods have been applied, e.g., lumping together states of a discrete state space among which transitions are fast [170–173], averaging over states for discrete [174] or continuous processes [173, 175], eliminating single states from a network description [176–178], or eliminating slow (invisible) degrees of freedom [179–181]. It was found that, in general, coarse-graining has implications on the entropy production and, in particular [182], dissipation. In the context of biological systems and especially molecular motors, coarse-graining procedures mostly focus on eliminating selected states of the motor [178, 183] or on reducing continuous (ratchet) models to discrete-state models [76, 129, 184–186].

In the present chapter, we introduce a coarse-graining procedure that allows us to reduce molecular motor-bead models to effective one-particle models with discrete motor states with the external force acting directly on the effective motor particle. We eliminate the explicit dynamics of the probe particle completely still maintaining the correct local detailed balance condition for the effective motor transition rates and preserving the average currents of the system. As a main result, we find that the coarse-grained rates show a more complex force dependence than the usually assumed exponential behavior and a more complex concentration dependence than mass action law kinetics. The results presented in this chapter have been published in [137].

7.2. General one-state motor model

7.2.1. Coarse-graining procedure

The general model for motor proteins with a single internal state coupled to a probe particle has been introduced in chapter 3. Starting from such a generic hybrid model, we will now develop a thermodynamically consistent coarse-graining procedure. In the coarse-grained description of the model we want to map the motor-bead system to one effective motor particle hopping between states separated by d. We thus have to eliminate the x-coordinate from the (n,x)-description resulting in a system characterized only by n.

For the coarse-grained model, we impose the following conditions. The coarse-grained transition rates $\Omega^{\pm}$ which advance the effective particle by d should obey a LDB condition

$$\frac{\Omega^{+}}{\Omega^{-}} = \exp[\Delta\mu - f_{\mathrm{ex}}d] \tag{7.1}$$

as the force is now assumed to act directly on the effective motor particle. Furthermore, we require that the coarse-grained particle moves with the same average velocity in the steady state as the motor and the probe in the original model, i.e.,

$$v = d(\Omega^{+} - \Omega^{-}). \tag{7.2}$$

Solving the linear system of equations (7.1, 7.2) yields the coarse-grained rates

$$\Omega^{+} = \frac{v\exp[\Delta\mu - f_{\mathrm{ex}}d]/d}{\exp[\Delta\mu - f_{\mathrm{ex}}d] - 1} \tag{7.3}$$

$$\Omega^{-} = \frac{v/d}{\exp[\Delta\mu - f_{\mathrm{ex}}d] - 1}. \tag{7.4}$$

In general, the coarse-grained rates depend (via v) on all model parameters, including the friction coefficient of the probe particle and the specific potential of the linker. If one had chosen coarse-grained rates by just averaging over the positions of the probe particle, i.e., by

$$\langle w^{\pm}\rangle = \int_{-\infty}^{\infty} p^{s}(y)w^{\pm}(y)\,\mathrm{d}y, \tag{7.5}$$

one would have obtained rates that yield the correct average velocity but do not fulfill the LDB condition, as discussed in section 7.2.6.

7.2.2. Interpretation in terms of cycle currents

The coarse-grained rates can be interpreted as effective transition rates that correspond to a transition process after which both particles, motor and probe, have advanced a distance $\pm d$. Using the network description, this can easily be seen since the coarse-grained rates can be derived from cycle currents corresponding to such a process. The following procedure is illustrated in Fig. 7.1.

The network of a one-state motor-probe complex contains cycles that advance both particles by d while ending in the same (y)-state on the network. The flux of these cycles is given by Eqs. (6.3, 6.4). The directed cycle fluxes obey

$$\frac{J_a^+}{J_a^-} = \exp[\Delta\mu - f_{\mathrm{ex}} d] \tag{7.6}$$

and their sum constitutes the average velocity $v = d \sum_\alpha (J_\alpha^+ - J_\alpha^-)$. As we require exactly these conditions for the coarse-grained rates, we identify a pair of coarse-grained rates for each cycle with the directed cycle fluxes

$$\omega_a^+ \equiv J_a^+, \quad \omega_a^- \equiv J_a^- . \tag{7.7}$$

Each of these rates corresponds to one of the several possible displacement processes (for any y) to advance both particles by d, including ones with l forward and $l-1$ backward motor jumps.

This description can be further simplified to result in the coarse-grained description introduced in the previous section. If one has two sets of states, A and B, a possible definition of the average rate to jump from one set to the other is given by [172]

$$\Omega^+ \equiv \sum_{k\in A} \sum_{l\in B} p(k|A)\omega_{kl}. \tag{7.8}$$

Since our motor model has only one state, the above formula yields

$$\Omega^+ = \sum_a \omega_a^+, \quad \Omega^- = \sum_a \omega_a^- \tag{7.9}$$

with $v = d(\Omega^+ - \Omega^-)$ and

$$\frac{\Omega^+}{\Omega^-} = \frac{\sum \omega_a^+}{\sum \omega_a^-} = \frac{\sum \omega_a^- \exp[\Delta\mu - f_{\mathrm{ex}} d]}{\sum \omega_a^-} = \exp[\Delta\mu - f_{\mathrm{ex}} d]. \tag{7.10}$$

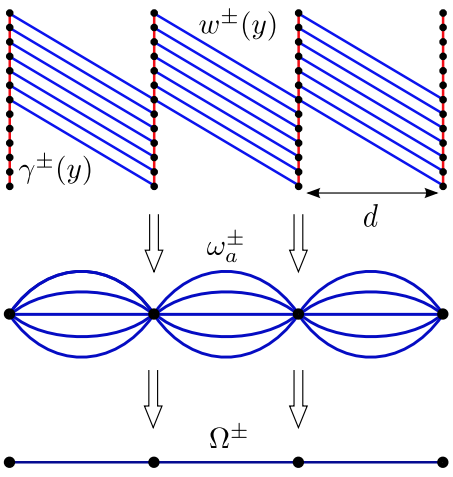

Figure 7.1: Coarse-graining procedure for a hybrid model with a one-state motor. Top: Unfolded illustration of the original network of the motor-probe complex with transitions of the motor along the blue lines with rates $w^{\pm}(y)$ and transitions of the probe along the red lines with rates $\gamma^{\pm}(y)$. Center: Reduced network after eliminating the dynamics of the probe. The effective motor particle can jump via several transition pathways with rates $\omega_a^{\pm}$. Bottom: Coarse-grained network with a single transition with rates $\Omega^{\pm}$ connecting adjacent positions.

The coarse-grained rates (7.9) can also be expressed as

$$\Omega^{+} = \sum_a \omega_a^{+} = \sum_a \omega_a^{+} \frac{1-\exp[-\Delta\mu + f_{\mathrm{ex}} d]}{1-\exp[-\Delta\mu + f_{\mathrm{ex}} d]} = \frac{\sum_a (\omega_a^{+} - \omega_a^{-})}{1-\exp[-\Delta\mu + f_{\mathrm{ex}} d]}$$
$$= \frac{v \exp[\Delta\mu - f_{\mathrm{ex}} d]/d}{\exp[\Delta\mu - f_{\mathrm{ex}} d] - 1}, \tag{7.11}$$

$$\Omega^{-} = \sum_a \omega_a^{-} = \sum_a \omega_a^{-} \frac{\exp[\Delta\mu - f_{\mathrm{ex}} d] - 1}{\exp[\Delta\mu - f_{\mathrm{ex}} d] - 1} = \frac{v/d}{\exp[\Delta\mu - f_{\mathrm{ex}} d] - 1}, \tag{7.12}$$

which is precisely (7.3, 7.4). Hence, the coarse-grained rate corresponds to the rate with which one effective displacement will happen.

7.2.3. Time-scale separation

In this section, we will investigate under which conditions the coarse-grained rates (7.3, 7.4) can be expressed using a single exponential dependence on the external force as typically assumed for mechanical transitions within one-particle models [26, 28].

Inserting Eqs. (3.3, 3.4) in Eq. (3.6) in the NESS shows that the contribution due to motor jumps is weighted with a (dimensionless) prefactor

$$\varepsilon \equiv w_0 \exp[\mu_{\mathrm{T}}^{\mathrm{eq}}] d^2 \gamma. \tag{7.13}$$

Here $w_0 \exp[\mu_{\mathrm{T}}^{\mathrm{eq}}]$ determines the time scale of the transitions of the motor while γd^2 determines the timescale of the dynamics of the probe particle. The latter is mainly governed by the size of the bead and the step size of the motor, whereas $w_0 \exp[\mu_{\mathrm{T}}^{\mathrm{eq}}]$ is determined by the attempt frequency and also by the absolute nucleotide concentrations.

If the dynamics of the bead is much faster than the transitions of the motor, time-scale separation holds with $\varepsilon \to 0$ [172, 187]. In this limit of fast bead relaxation, denoted throughout by a caret, the stationary solution of Eq. (3.6) in the NESS becomes

$$\hat{p}^s(y) = \exp[-V(y) + f_{\mathrm{ex}} y]/\mathcal{N} \tag{7.14}$$

with $\mathcal{N} \equiv \int_{-\infty}^{\infty} \exp[-V(y) + f_{\mathrm{ex}} y]\,\mathrm{d}y$. The average velocity is then given by

$$\begin{aligned}\hat{v} =& d \int_{-\infty}^{\infty} \hat{p}^s(y)(w^+(y) - w^-(y))\,\mathrm{d}y \\ =& d w_0 \left(e^{\mu_{\mathrm{T}} - f_{\mathrm{ex}} d\theta^+} - e^{\mu_{\mathrm{D}} + \mu_{\mathrm{P}} + f_{\mathrm{ex}} d\theta^-} \right).\end{aligned} \tag{7.15}$$

This expression inserted into Eqs. (7.3, 7.4) yields

$$\hat{\Omega}^+ = w_0 e^{\mu_{\mathrm{T}} - f_{\mathrm{ex}} d\theta^+}, \tag{7.16}$$

$$\hat{\Omega}^- = w_0 e^{\mu_{\mathrm{D}} + \mu_{\mathrm{P}} + f_{\mathrm{ex}} d\theta^-} \tag{7.17}$$

independent of any specific linker potential $V(y)$. Since this force dependence is purely exponential with the correct load-sharing factor, these expressions represent exactly the rates typically used in one-particle models. We notice that within this approximation $\Omega^+ = \langle w^+(y) \rangle$ and $\Omega^- = \langle w^-(y) \rangle$ holds true, which is in agreement with other coarse-graining procedures in the time-scale separation limit, e.g., [172–174].

Note that only transition rates of the motor whose dependence on the linker potential is chosen accordingly in the Kramers form (Eqs. (3.3, 3.4)) lead generically to consistent coarse-grained and averaged rates when using the fast-bead limit of $p^s(y)$.

7.2.4. Example: F_1-ATPase

In general, a strong time-scale separation between motor and probe is not necessarily realistic. In this case, Eq. (3.6) must be solved numerically. We will use the model introduced in section 3.2 and used in chapters 4, 5, see Fig. 3.1, with a harmonic potential $V(y) = \kappa y^2/2$ as a simple example to illustrate our coarse-graining procedure.

In Fig. 7.2, the results for Ω^+ and Ω^- are shown for various values of the friction coefficient γ. With decreasing γ, the rates approach their corresponding fast-bead limits, $\hat{\Omega}^+$ and $\hat{\Omega}^-$. These values are upper bounds because decreasing γ implies smaller probe particles which exert less drag on the motor. For finite γ, the coarse-grained rates do not show a single exponential dependence on f_{ex} over the whole range of external forces. Such a dependence, however, is usually assumed to hold

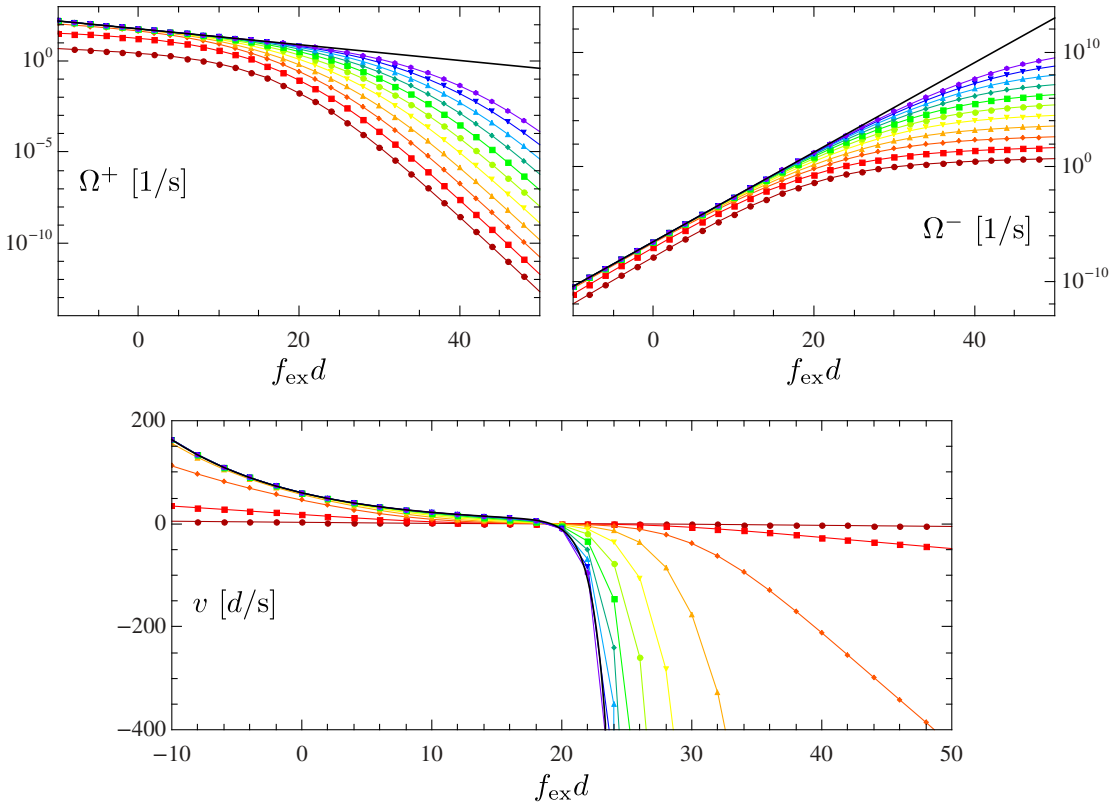

Figure 7.2.: Coarse-grained rates Ω^+ and Ω^- (top) and average velocity (bottom) as functions of $f_{\mathrm{ex}}d$ for various friction coefficients γ in the range $5\,\mathrm{s}/d^2 \geq \gamma \geq 5\times10^{-10}\,\mathrm{s}/d^2$ (from bottom to top). With decreasing γ, the rates and the velocity approach the corresponding fast-bead limit (black lines). Parameters: $\kappa = 40\,d^{-2}$, $c_{\mathrm{T}} = c_{\mathrm{D}} = 2\,\mu\mathrm{M}$, $c_{\mathrm{P}} = 1\,\mathrm{mM}$, $\Delta\mu = 19$, $\theta^+ = 0.1$, $w_0 \exp[\mu_{\mathrm{T}}^{\mathrm{eq}}]/c_{\mathrm{T}}^{\mathrm{eq}} = 3\times10^7\,(\mathrm{Ms})^{-1}$.

within one-particle models. Moreover, the coarse-grained rates depend on γ, which is a parameter not incorporated explicitly in many one-particle models.

The experimentally accessible values of γ cover a wide range of the values chosen in Fig. 7.2. A dimer of polystyrene beads ($\simeq 280$ nm) as used in [15, 77, 119, 121] corresponds to $\gamma = 0.5\,\mathrm{s}/d^2$ (red line) while a 40 nm gold particle [74, 87, 121] corresponds to $\gamma = 5\times10^{-4}\,\mathrm{s}/d^2$ (yellow line). Especially for large external forces, the coarse-grained rates deviate strongly from their asymptotic values even for a probe as small as the gold particle.

The average velocity as shown in Fig. 7.2 also strongly depends on the friction coefficient of the probe particle, especially for large external forces. In this regime, for large γ, the velocity is dominated by the friction experienced by the probe while for small γ the probe relaxes almost immediately and the velocity is dominated by the time scale of the motor jumps.

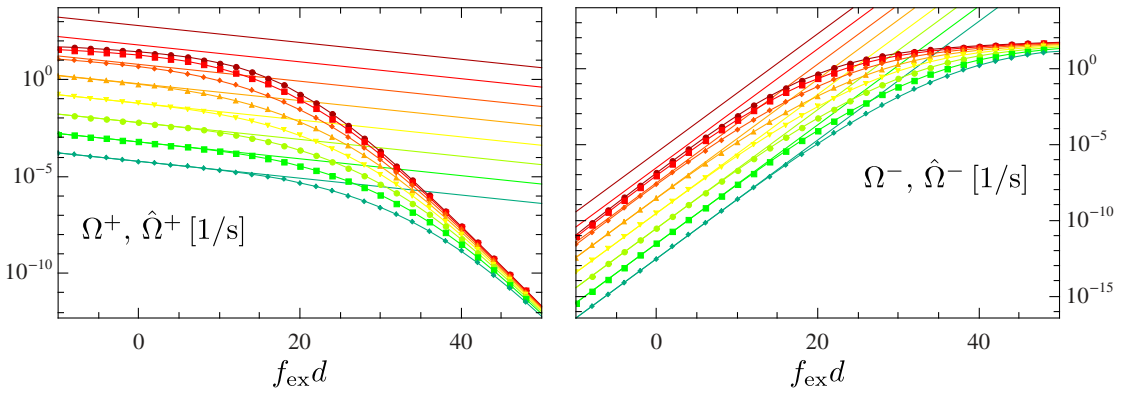

Figure 7.3.: Coarse-grained rates Ω^+ and Ω^- as functions of $f_{\rm ex}d$ for various $c_{\rm T}$, $c_{\rm D}$ in the range $2\times10^{-5}\,{\rm M} \geq c_{\rm T}, c_{\rm D} \geq 2\times10^{-12}\,{\rm M}$ (from top to bottom). With decreasing $c_{\rm T}, c_{\rm D}$, the rates approach the fast-bead limits $\hat{\Omega}^+$ and $\hat{\Omega}^-$ (straight lines). Parameters: $\kappa = 40\,d^{-2}$, $\gamma = 0.5\,{\rm s}/d^2$, $c_{\rm P} = 1\,{\rm mM}$, $\Delta\mu = 19$, $\theta^+ = 0.1$, $w_0 \exp[\mu_{\rm T}^{\rm eq}]/c_{\rm T}^{\rm eq} = 3\times10^7\,({\rm Ms})^{-1}$.

Another option to reach the fast-bead limit is to use very small nucleotide concentrations. In Fig. 7.3, we show the coarse-grained rates for various ATP and ADP concentrations. With decreasing nucleotide concentration (at fixed $\Delta\mu$), the rates approach the asymptotic $\hat{\Omega}^+$ and $\hat{\Omega}^-$. However, it is very hard to do experiments at concentrations smaller than $\simeq 10^{-7}$M as jumps of the motor are then very rare.

In Fig. 7.2 and in Fig. 7.3 the dependence of the coarse-grained rates on the external force exhibits two different regimes. Up to values of the external force of roughly $15/d$, the coarse-grained rates can be well approximated by a single exponential dependence on $f_{\rm ex}$ with the same slope as in the fast-bead limit, $d\theta^+$ or $d\theta^-$, respectively. However, for large γ and large $c_{\rm T}$, even in this regime, the absolute values of the coarse-grained rates deviate up to two orders of magnitude from their fast-bead approximation. For such parameters, assuming a monoexponential dependence on $f_{\rm ex}$ with the above slope would not be appropriate either.

For large external forces, all coarse-grained rates deviate significantly from their fast-bead limits. We find again a monoexponential decay for Ω^+ but now with slope $-d$ whereas Ω^- grows only linearly with increasing $f_{\rm ex}$. This so far unaccounted for behavior can be understood by considering the limit $f_{\rm ex} \to \infty$ as discussed below. The crossover from one regime to the other occurs beyond the stall force $f_{\rm ex} = \Delta\mu/d$.

7.2.5. Limiting case: Large applied force

In the limit of large external forces, $f_{\mathrm{ex}} \to \infty$, the coarse-grained rates (7.3, 7.4) can be expressed as

$$\Omega^+ \approx -v \exp[\Delta\mu - f_{\mathrm{ex}} d]/d \tag{7.18}$$
$$\Omega^- \approx -v/d. \tag{7.19}$$

While $\Delta\mu$ is independent of the external force, the average velocity is a function of the external force,

$$v = \langle \partial_y V(y) - f_{\mathrm{ex}} \rangle / \gamma = \kappa \langle y \rangle / \gamma - f_{\mathrm{ex}}/\gamma. \tag{7.20}$$

It becomes negative for forces larger than the stall force $\Delta\mu/d$, which ensures that both Ω^+ and Ω^- are positive. If there is no time-scale separation between the dynamics of motor and probe, $\langle y \rangle$ grows linearly in f_{ex} for $f_{\mathrm{ex}} \to \infty$ with a smaller slope than $1/\kappa$. On the other hand, with time-scale separation, we have $\langle y \rangle = f_{\mathrm{ex}}/\kappa$. Note that within time-scale separation, the average velocity has to be calculated using the average velocity of the motor, Eq. (3.7), since the "average velocity" of the probe $\langle \partial_y V(y) - f_{\mathrm{ex}} \rangle / \gamma$ is zero as a result of the fast-bead limit of Eq. (3.6). Due to the linear dependence of $\langle y \rangle$ on f_{ex}, the average velocity, and therefore also Ω^-, are then proportional to the external force, whereas the exponential factor dominates for Ω^+,

$$\Omega^+ \sim f_{\mathrm{ex}} \exp[\Delta\mu - f_{\mathrm{ex}} d]/(\gamma d) \tag{7.21}$$
$$\Omega^- \sim f_{\mathrm{ex}}/(\gamma d). \tag{7.22}$$

In the opposite limit of a large assisting force $f_{\mathrm{ex}} \to -\infty$, the coarse-grained rates (7.3, 7.4) become

$$\Omega^+ \approx v/d \tag{7.23}$$
$$\Omega^- \approx v \exp[-\Delta\mu + f_{\mathrm{ex}} d]/d \tag{7.24}$$

As above, the average y grows linearly and the velocity is proportional to f_{ex} if there is no time-scale separation which leads to

$$\Omega^+ \sim |f_{\mathrm{ex}}|/(\gamma d) \tag{7.25}$$
$$\Omega^- \sim |f_{\mathrm{ex}}| \exp[-\Delta\mu + f_{\mathrm{ex}} d]/(\gamma d). \tag{7.26}$$

This simple analysis clearly shows that the coarse-grained rates do not coincide with the often *a priori* assumed single exponential force dependence of one-particle rates. Within our numerical analysis, the asymptotic behavior appears for $|f_{\mathrm{ex}}| \gtrsim 500/d$. The regime for large forces shown in Figs. 7.2 and 7.3 is not the asymptotics

yet. However, since $\langle y \rangle$ is also linear in f_{ex} in this region yet with different slope, v is still proportional to f_{ex}.

In summary, we find that for the F_1-ATPase under realistic experimental conditions the rates in a coarse-grained description comprising only one effective particle that satisfy the LDB condition Eq. (7.1) and reproduce the correct average velocity v cannot be written in the form of a single exponential dependence on the external force.

7.2.6. Comparison of coarse-grained with averaged rates

Instead of defining the coarse-grained rates according to Eqs. (7.3, 7.4), one might be tempted to use the averaged rates (7.5) as a definition for the coarse-grained rates. In Fig. 7.4, we show the averaged rates of our F_1-ATPase model as well

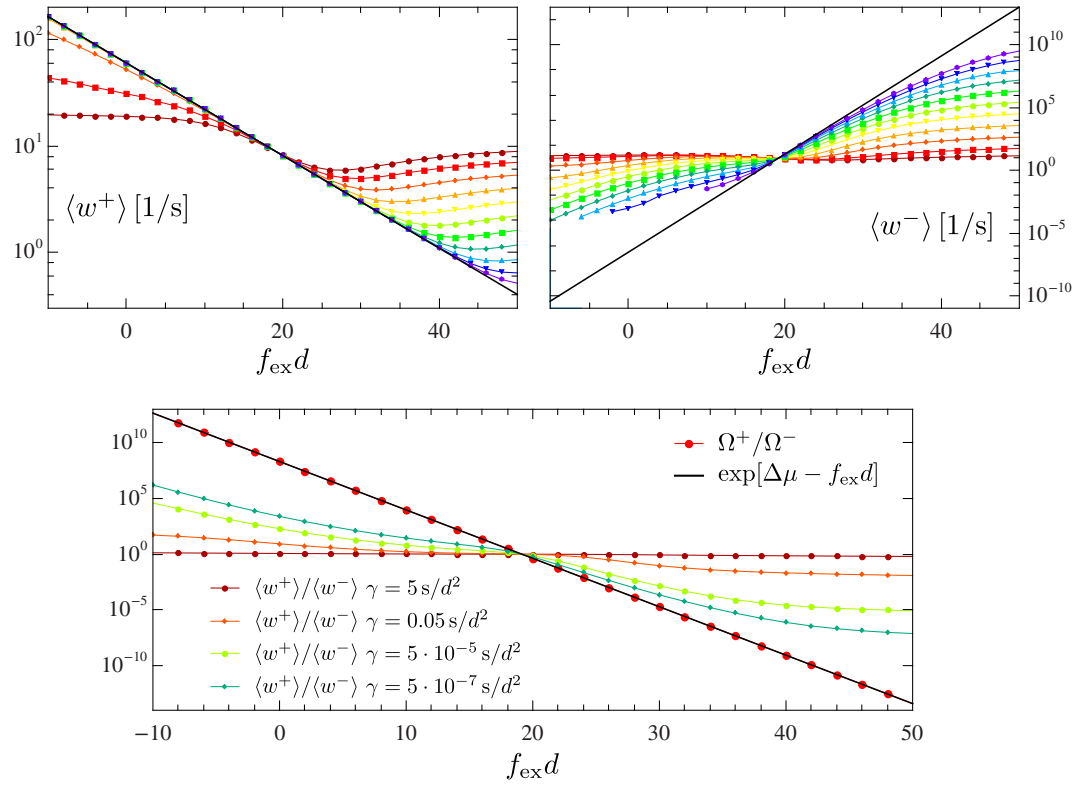

Figure 7.4.: Top: Average rates $\langle w^+ \rangle$ and $\langle w^- \rangle$ as functions of $f_{\mathrm{ex}}d$ for various γ in the range $5\,\mathrm{s}/d^2 \geq \gamma \geq 5 \times 10^{-9}\,\mathrm{s}/d^2$. With decreasing γ, the rates approach $\hat{\Omega}^+$, $\hat{\Omega}^-$ (black lines). Bottom: Ratio of + and − rates. In contrast to Ω^+, Ω^- (red), the averaged motor rates do not fulfill the LDB condition (black line). The parameters are the same as in Fig. 7.2.

as their ratio corresponding to the LDB condition. We find that both $\langle w^+ \rangle$ and $\langle w^- \rangle$ (for the latter less visible in the plot) exhibit nonmonotonic dependence on the external force. For external forces slightly larger than the stall force, $\langle w^+ \rangle$ increases with increasing f_{ex} since in this region the system moves backward with motor jumps following the probe which leads to a peak at small y in $p^s(y)$. On the other hand, $\langle w^- \rangle$ exhibits a minimum around stall conditions for large γ since in this region, $p^s(y)$ misses a peak at large $y \simeq 1$.

A severe issue appears regarding the LDB condition. The corresponding ratio of the averaged rates is also plotted in Fig. 7.4 where it can be clearly seen that the LDB condition is not fulfilled (except in the fast-bead limit).

7.2.7. Without external force

Even though we have motivated this chapter by emphasizing that external forces are typically applied to probe particles, it should be obvious that our approach holds true for molecular motors transporting cargo subject to Stokes friction in the absence of external forces.

For one-particle models, the friction coefficient of the probe cannot be taken into account explicitly. One rather has to incorporate the drag effect of the bead into the motor rates [76]. If one wants to analyze experimental data obtained from probe particles of different sizes, one then has to use different values of the motor rates for each data set.

For the rather dilute solutions used in experiments [15, 77, 99] one generally assumes that the motor dynamics is subject to mass action law kinetics, i.e., that the transition rates depend linearly on the corresponding concentration of nucleotides. Obviously, this linear dependence holds for all concentrations and beads of all sizes for one-particle models. When keeping c_{D} and c_{P} fixed, the average velocity of a one-state motor will show a purely linear dependence on c_{T}.

The experimental analysis of the average velocity of the F_1-ATPase as function of c_{T} (for fixed c_{D}, c_{P}) reveals a saturation of the velocity for large ATP concentrations which sets in earlier for large beads [74]. While such a saturation is usually attributed to the hydrolysis step, we find that a sublinear dependence of the velocity can also be caused by the drag of the probe particle.

In Fig. 7.5, the coarse-grained rates as well as the velocity are shown as a function of the ATP concentration. With decreasing γ, the coarse-grained rates approach the fast-bead limit and the mass action law kinetics. The velocity is then linear in c_{T} as in a one-particle model. For large γ, eliminating the cargo by coarse-graining yields coarse-grained rates that are not linear in the concentrations although the motor rates are still subject to mass action law kinetics. Moreover, the velocity then exhibits a sublinear dependence reminiscent of the typical saturation effect for large c_{T}.

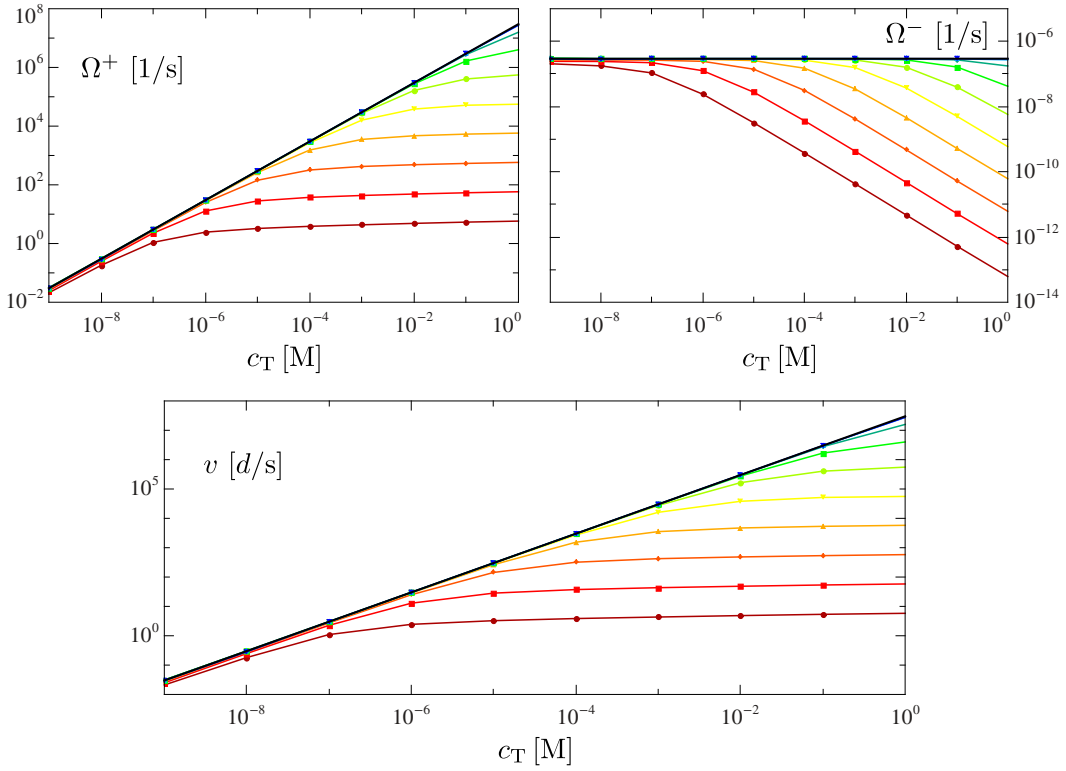

Figure 7.5.: Coarse-grained rates Ω^+ and Ω^- (top) and average velocity (bottom) for various γ and $f_{ex} = 0$ as functions of c_T. Since c_D and c_P are fixed, $\Delta\mu$ also increases with c_T. The rates and the velocity approach the fast-bead approximation (black lines). Parameters: $c_D = 2\,\mu M$, $c_P = 1\,mM$, $\kappa = 40\,d^{-2}$, $\theta^+ = 0.1$, $w_0 \exp[\mu_T^{eq}]/c_T^{eq} = 3 \times 10^7\,(Ms)^{-1}$, γ in the range $5\,s/d^2 \geq \gamma \geq 5 \times 10^{-9}\,s/d^2$ (from bottom to top).

7.2.8. Comparison of full and coarse-grained trajectories

Trajectories of motor and probe generated by a simulation of the complete model of the F_1-ATPase are shown in Fig. 7.6.

Additionally, Fig. 7.6 contains a trajectory obtained from simulating the corresponding coarse-grained model. The average velocity of both models is the same (by definition, see Eq. (7.2)), whereas the coarse-grained model produces trajectories that are "more random". This behavior occurs since the coarse-grained rates are constant (for fixed parameters) and produce a simple biased random walk. The motor transition rates of the complete model, however, depend on the actual position of the probe and are therefore implicitly time dependent. Since fast successive motor jumps are suppressed, the trajectory of the complete model is less random [135, 159].

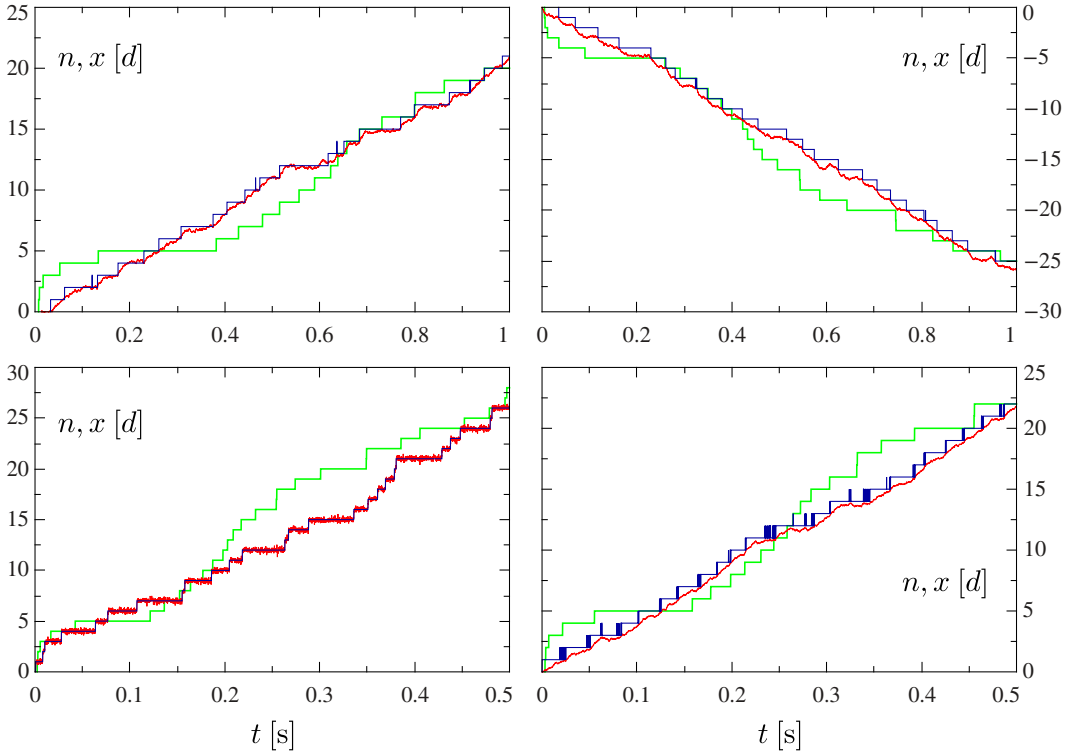

Figure 7.6.: Trajectories of the one-state model for the F_1-ATPase for several parameter sets obtained from simulations. The trajectory of the detailed model (motor: blue, probe: red) is shown together with a trajectory of its corresponding coarse-grained model (green). Parameters: $\kappa = 40\,d^{-2}$, $\theta^+ = 0.1$, $w_0 \exp[\mu_T^{eq}]/c_T^{eq} = 3 \times 10^7\,(\mathrm{Ms})^{-1}$, $\gamma = 0.5\,\mathrm{s}/d^2$, $f_{ex} = 0$, $c_T = c_D = 2\,\mu\mathrm{M}$, $c_P = 1\,\mathrm{mM}$ (top left); $\gamma = 0.5\,\mathrm{s}/d^2$, $f_{ex} = 40\,d^{-1}$, $c_T = c_D = 2\,\mu\mathrm{M}$, $c_P = 1\,\mathrm{mM}$ (top right); $\gamma = 0.005\,\mathrm{s}/d^2$, $f_{ex} = 0$, $c_T = c_D = 2\,\mu\mathrm{M}$, $c_P = 1\,\mathrm{mM}$ (bottom left); $\gamma = 0.5\,\mathrm{s}/d^2$, $f_{ex} = 0$, $c_T = 1\,\mathrm{mM}$, $c_D = 2\,\mu\mathrm{M}$, $c_P = 1\,\mathrm{mM}$ (bottom right).

A quantitative measure of this phenomenon is provided by the diffusion coefficient. Applying the most simple network model for a one-state motor with only two accessible configurations of the linker ($y = 0$ and $y = d$), the diffusion coefficient of the full model is given by [26, 188]

$$D_w = \frac{d^2(w^+\gamma^+ + w^-\gamma^-)}{2(w^+ + w^- + \gamma^+ + \gamma^-)} - \frac{v^2}{w^+ + w^- + \gamma^+ + \gamma^-} \tag{7.27}$$

$$= \frac{d^2(\Omega^+ + \Omega^-)}{2} - \frac{v^2}{w^+ + w^- + \gamma^+ + \gamma^-} \tag{7.28}$$

$$= \frac{d^2}{2} D_\Omega - \frac{v^2}{w^+ + w^- + \gamma^+ + \gamma^-}, \tag{7.29}$$

which is obviously smaller than the diffusion coefficient of the coarse-grained model, D_Ω. Hence, trajectories of the coarse-grained description show more diffusion than the original ones. For continuous y, one would have to calculate the diffusion coefficient of the full model using a Green-Kubo-formula which yields the effective diffusion coefficient of the probe as integral over the VACF (minus v^2) [50, 153].

The influence of parameters like the probe size or the ATP concentration on the dynamics is visible in the bottom panels of Fig. 7.6. While the average velocity is almost the same, the trajectories of the complete model differ significantly. Using a small probe with a small friction coefficient, the probe relaxes to the potential minimum of the linker before the next motor jump occurs, whereas the large probe cannot relax [136]. Large ATP concentrations induce many forward and successive backward motor jumps that are absent at lower ATP concentrations. These details are not captured in the coarse-grained trajectories.

7.3. Motor models with several internal states

7.3.1. Coarse-graining procedure

Considering a generic hybrid model with a multistate motor as introduced in section 3.3, the coarse-grained version of such a model should take into account the different states of the motor as well as the several possible α transitions between i and j. Thus, the motor network (including all motor cycles) should be conserved under coarse-graining. In Fig. 6.1, the top view of the full network, which represents the bare motor network, also corresponds to the coarse-grained version of this model. To account for the several internal states, we require that the coarse-grained rates should obey a LDB condition and the operational current from motor state i to motor state j via edge α, Eq. (6.7), should be conserved. Conserving the operational currents corresponds to the condition of reproducing the correct mean velocity for the one-state model. The above conditions read

$$\frac{\Omega_{ij}^{\alpha}}{\Omega_{ji}^{\alpha}} = \exp[-\Delta F_{ij}^{\alpha} - f_{\mathrm{ex}} d_{ij}^{\alpha}] \tag{7.30}$$

and

$$P_i \Omega_{ij}^{\alpha} - P_j \Omega_{ji}^{\alpha} = j_{ij}^{\alpha} \tag{7.31}$$

with the operational current

$$j_{ij}^{\alpha} \equiv \int_{-\infty}^{\infty} \left(p_i(y) w_{ij}^{\alpha}(y) - p_j(y + d_{ij}^{\alpha}) w_{ji}^{\alpha}(y + d_{ij}^{\alpha}) \right) \mathrm{d}y = -j_{ji}^{\alpha} \tag{7.32}$$

and the marginal distribution

$$P_i = \int_{-\infty}^{\infty} p_i(y)\,\mathrm{d}y. \tag{7.33}$$

These equations can be solved for Ω_{ij}^{α} and Ω_{ji}^{α} using simple algebra which yields the rates

$$\Omega_{ij}^{\alpha} = j_{ij}^{\alpha}\,\frac{\exp[-\Delta F_{ij}^{\alpha} - f_{\mathrm{ex}} d_{ij}^{\alpha}]}{P_i \exp[-\Delta F_{ij}^{\alpha} - f_{\mathrm{ex}} d_{ij}^{\alpha}] - P_j} \tag{7.34}$$

$$\Omega_{ji}^{\alpha} = j_{ij}^{\alpha}\,\frac{1}{P_i \exp[-\Delta F_{ij}^{\alpha} - f_{\mathrm{ex}} d_{ij}^{\alpha}] - P_j}. \tag{7.35}$$

In principle, it is sufficient to use only Eq. (7.34), since Ω_{ji}^{α} takes exactly this form with $j_{ij}^{\alpha} = -j_{ji}^{\alpha}, \Delta F_{ij}^{\alpha} = -\Delta F_{ji}^{\alpha}$ and $d_{ij}^{\alpha} = -d_{ji}^{\alpha}$. This equivalent procedure would be more symmetric and treat all transition rates on an equal footing but the LDB condition is then less obvious. Note that without the LDB condition (7.30), the stated conditions of P_i and j_{ij}^{α} would also be compatible with coarse-grained rates like the ones in, e.g., [172, 174].

Transitions whose rates are independent of the linker elongation y and hence have $d_{ij}^{\alpha} = 0$ retrieve their original rate constants through this coarse-graining procedure. For such a transition, j_{ij}^{α} is given by

$$j_{ij}^{\alpha} = P_i w_{ij}^{\alpha} - P_j w_{ji}^{\alpha} \tag{7.36}$$

with rates fulfilling the LDB condition $w_{ij}^{\alpha}/w_{ji}^{\alpha} = \exp[-\Delta F_{ij}^{\alpha}]$. Inserting j_{ij}^{α} in Eqs. (7.34, 7.35) and using the LDB condition and $d_{ij}^{\alpha} = 0$ immediately yields

$$\Omega_{ij}^{\alpha} = w_{ij}^{\alpha}, \quad \Omega_{ji}^{\alpha} = w_{ji}^{\alpha}. \tag{7.37}$$

Transitions with rates depending on y but with $d_{ij}^{\alpha} = 0$ have coarse-grained rates that depend on f_{ex} only implicitly via j_{ij}^{α} and $P_{i,j}$ as will be discussed below in section 7.3.4 for the chemical transition rates of kinesin.

The rates determined from the LDB condition Eq. (7.30), the populations P_i and the operational currents are algebraically consistent with the fact that a full set of rates Ω_{ij}^{α} will uniquely determine the populations P_i on the coarse-grained network. Consistency can be seen by integrating the Fokker-Planck equation (3.12) over y, yielding the coarse-grained master equation

$$\partial_t P_i = \sum_{j,\alpha} j_{ji}^{\alpha} = \sum_{j,\alpha} P_j \Omega_{ji}^{\alpha} - P_i \Omega_{ij}^{\alpha}, \tag{7.38}$$

whose stationary solution in the NESS can be expressed as a function of the rates Ω_{ij}^{α} [47, 167]. Thus, the expression of any current observable in terms of the operational currents is consistent with its expression in terms of cycle currents on the coarse-grained network.

7.3.2. Time-scale separation

Similarly to the one-state model, we explore the consequences of a putative time-scale separation between the dynamics of motor and probe for each motor transition. In the limit $\gamma \to 0$ (formally equivalent to $\varepsilon \to 0$ but here one would have several ε_{ij} within the Fokker-Planck equation and all go to 0) the solution of Eq. (3.12) in the NESS becomes, analogously to [170, 173],

$$\hat{p}_i^s(y) = \hat{P}_i \exp[-V(y) + f_{\mathrm{ex}} y]/\mathcal{N}. \tag{7.39}$$

The marginal distribution can be obtained using Eq. (3.12) with its solution for fast bead relaxation

$$\begin{aligned} \partial_t \hat{P}_i &= \int_{-\infty}^{\infty} \partial_t \hat{p}_i^s(y)\, \mathrm{d}y \\ &= \sum_{j,\alpha} \left(\hat{P}_j \langle w_{ji}^\alpha \rangle_y - \hat{P}_i \langle w_{ij}^\alpha \rangle_y \right) = \sum_{j,\alpha} \hat{j}_{ji}^\alpha = 0. \end{aligned} \tag{7.40}$$

For Kramers-type transition rates like Eqs. (3.10, 3.11), the y-averaged rates $\langle w_{ij}^\alpha \rangle_y$ and $\langle w_{ji}^\alpha \rangle_y$ become

$$\langle w_{ij}^\alpha \rangle_y = k_{ij}^\alpha \exp[\mu_{ij}^{\alpha,+} - f_{\mathrm{ex}} d_{ij}^\alpha \theta_{ij}^{\alpha,+}] \tag{7.41}$$

$$\langle w_{ji}^\alpha \rangle_y = k_{ji}^\alpha \exp[\mu_{ij}^{\alpha,-} + f_{\mathrm{ex}} d_{ij}^\alpha \theta_{ij}^{\alpha,-}]. \tag{7.42}$$

The change of chemical free energy $\Delta\mu_{ij}^\alpha$ is split into $\mu_{ij}^{\alpha,+}$ and $\mu_{ij}^{\alpha,-}$, indicating that both directions of the transition can involve binding and release of the chemical species that account for $\Delta\mu_{ij}^\alpha$. The free-energy change arising from changing the motor state, $F_j - F_i$, is incorporated in the attempt frequencies k_{ij}^α of the corresponding states. Inserting the operational current in the form of Eq. (7.40) with these averaged rates, simple calculus shows that the coarse-grained rates (7.34) and (7.35) reduce to

$$\hat{\Omega}_{ij}^\alpha = k_{ij}^\alpha \exp[\mu_{ij}^{\alpha,+} - f_{\mathrm{ex}} d_{ij}^\alpha \theta_{ij}^{\alpha,+}] \tag{7.43}$$

$$\hat{\Omega}_{ji}^\alpha = k_{ji}^\alpha \exp[\mu_{ij}^{\alpha,-} + f_{\mathrm{ex}} d_{ij}^\alpha \theta_{ij}^{\alpha,-}] \tag{7.44}$$

which is again consistent with transition rates of one-particle models that assume a purely exponential dependence on the external force.

7.3.3. Example: F_1-ATPase with intermediate step

With external force

A schematic representation of hybrid model for the F_1-ATPase with two internal states of the motor is shown in Fig. 3.3. The two different pathways for transitions

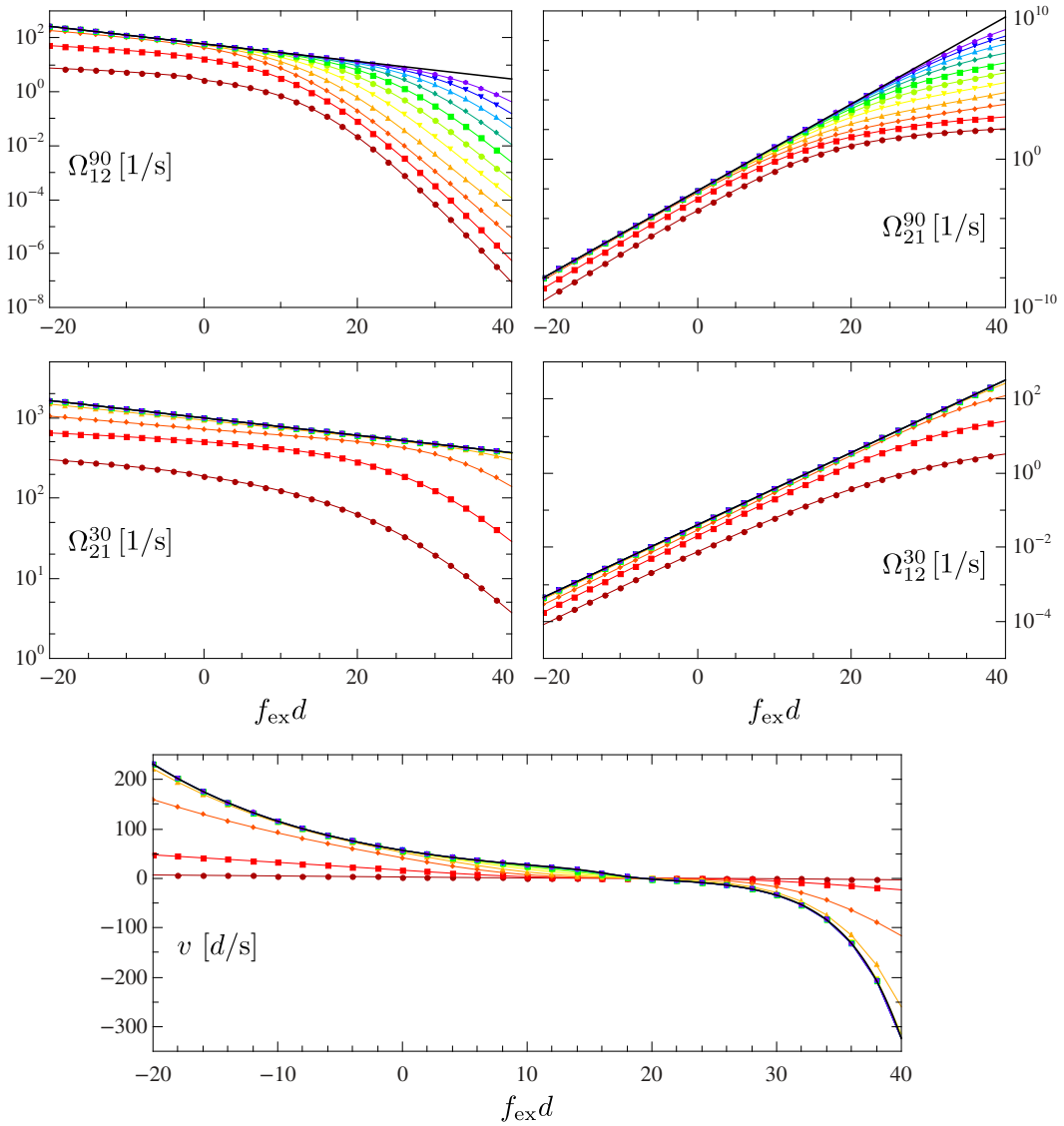

Figure 7.7.: Coarse-grained rates for the 90° (top) and the 30° (center) substep and average velocity (bottom) as functions of $f_{\mathrm{ex}}d$ for various γ in the range $5\,\mathrm{s}/d^2 \geq \gamma \geq 5\times10^{-10}\,\mathrm{s}/d^2$ (from bottom to top). With decreasing γ, the rates and the velocity approach their corresponding fast-bead limit. Parameters: $\kappa = 40\,d^{-2}$, $c_{\mathrm{T}} = c_{\mathrm{D}} = 2\,\mu\mathrm{M}$, $c_{\mathrm{P}} = 1\,\mathrm{mM}$, $\theta^{+}_{90,30} = 0.1$, $k_{12}^{90}\exp[\mu_{\mathrm{T}}^{\mathrm{eq}}]/c_{\mathrm{T}}^{\mathrm{eq}} = 3\times10^{7}\,(\mathrm{Ms})^{-1}$, $k_{21}^{90}\exp[\mu_{D}^{\mathrm{eq}}]/c_{\mathrm{D}}^{\mathrm{eq}} = 3667.5\,(\mathrm{Ms})^{-1}$, $k_{21}^{30} = 1000\,\mathrm{s}^{-1}$, $k_{12}^{30}\exp[\mu_{P}^{\mathrm{eq}}]/c_{\mathrm{P}}^{\mathrm{eq}} = 40\,(\mathrm{Ms})^{-1}$. The attempt frequencies are chosen on the basis of [74, 87] where very small probe particles have been used.

between the states 1 and 2 correspond to the 90° and 30° substeps of the F_1-ATPase, respectively.

Like in section 7.2.4 for the one-state model, we examine the coarse-grained rates for the 90° and 30° steps and the velocity which are shown in Fig. 7.7. Similarly to the 120°-scenario, the rates approach their fast-bead limit with decreasing γ.

As in the one-step model, the dependence of the coarse-grained rates on the external force shows two regimes. For small external forces, the rates can be well approximated by a single exponential dependence on f_{ex} with slope $\pm d_{ij}^{\alpha}\theta_{ij}^{\alpha,\pm}$ in most cases. For large probe particles, however, the rates neither match the absolute value nor show monoexponential dependence on f_{ex} with the above slope. For large forces, the forward rates decay faster, whereas the backward rates grow more slowly than in the fast-bead limit.

Concerning the average velocity, strong deviations from the fast-bead limit occur only for the largest friction coefficients. Using small beads, the force-velocity relation resulting from our coarse-graining procedure coincides well with the one obtained from a one-particle model due to the fact that the velocity involves only differences of the rates multiplied with the marginal distribution rather than the rates themselves. For large external forces and small γ, the velocity is significantly smaller than in the one-state model since the motor has to take two successive steps to cover the full d. The force-velocity relations for the two-state as well as for the one-state model reproduce very well the experimentally determined force-velocity relation from [77] for the corresponding value of the friction coefficient γ.

The limiting cases $f_{\mathrm{ex}} \to \pm\infty$ are more involved here than in the one-state model since one has to account for the dependence of the P_i's on the external force. However, as long as the P_j's do not decay faster than $\exp[-f_{\mathrm{ex}}d_{ij}^{\alpha}]$, it is still possible to approximate the rates (7.34, 7.35) by

$$\Omega_{ij}^{\alpha} \approx -j_{ij}^{\alpha}\exp[-\Delta F_{ij}^{\alpha} - f_{\mathrm{ex}}d_{ij}^{\alpha}]/P_j, \tag{7.45}$$

$$\Omega_{ji}^{\alpha} \approx -j_{ij}^{\alpha}/P_j \tag{7.46}$$

since P_i is bounded by 1.

For the F_1-ATPase model, the numerical analysis in the $f_{\mathrm{ex}} \to \infty$ limit yields a linear dependence of $\langle y\rangle$ and j_{ij}^{α} on f_{ex}. We also find that P_2 decays exponentially while P_1 approaches 1. Hence, Ω_{12}^{90} and Ω_{21}^{30} decay exponentially with slope $-d_{12}^{90} = -0.75\,d$ and $-d_{21}^{30} = -0.25\,d$, respectively, like in the one-state model but Ω_{21}^{90} now grows exponentially with a smaller exponent while Ω_{12}^{30} still grows linearly.

Without external force

Just as for the one-state model, we examine the dependence of the coarse-grained rates on the ATP concentration in the absence of external forces.

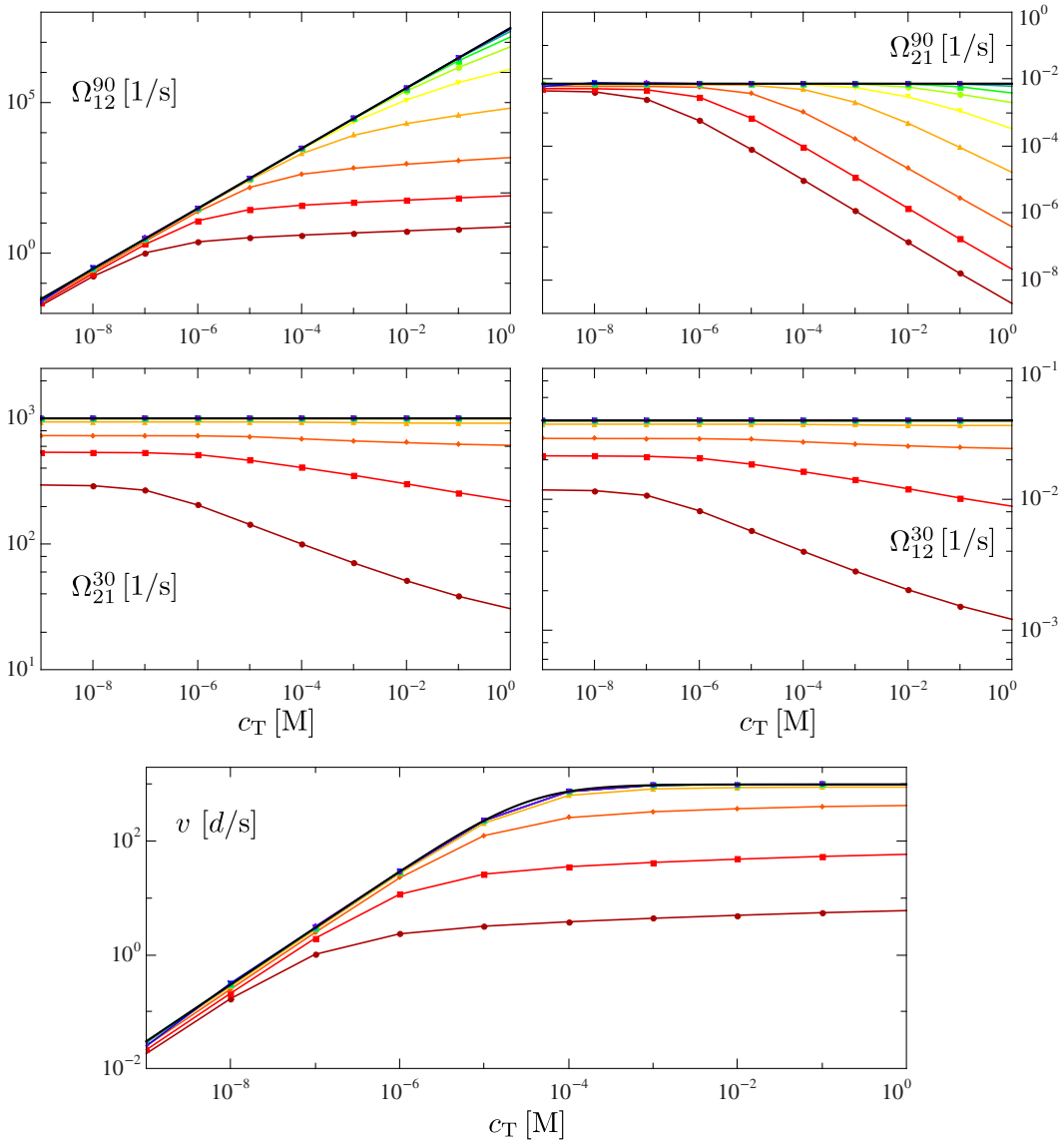

Figure 7.8.: Coarse-grained rates for the 90° (top) and the 30° (center) substep and average velocity (bottom) for various γ and $f_{ex} = 0$ as functions of c_T. Since c_D and c_P are fixed, $\Delta\mu$ also increases with c_T. The rates and the velocity approach the fast-bead approximation (black lines). Parameters: $c_D = 2\,\mu M$, $c_P = 1\,mM$, $\kappa = 40\,d^{-2}$, $\theta^{+}_{90,30} = 0.1$, γ in the range $5\,s/d^2 \geq \gamma \geq 5 \times 10^{-10}\,s/d^2$ (from bottom to top).

Fig. 7.8 shows the coarse-grained rates for the 90° and the 30° substeps as well as the aver age velocity. With decreasing γ, the coarse-grained rates approach the mass action law kinetics for the corresponding one-particle rates. In contrast to

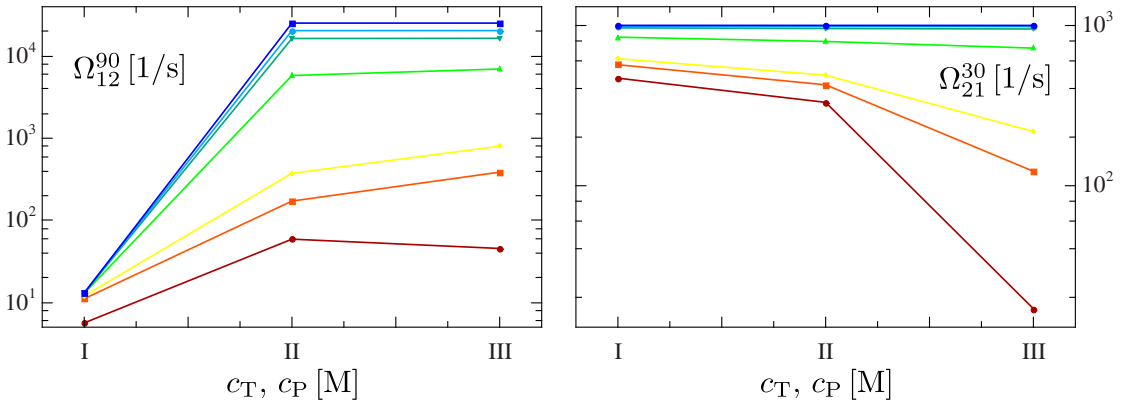

Figure 7.9.: Coarse-grained forward rates for various $\gamma = 2.1\text{s}/d^2$, $0.26\text{s}/d^2$, $0.14\text{s}/d^2$, $0.017\text{s}/d^2$, $0.003\text{s}/d^2$, $0.001\text{s}/d^2$, $3.8 \times 10^{-4}\text{s}/d^2$ (from bottom to top) for the parameter sets I: $c_T = 430\text{nM}$, $c_P = 1\text{nM}$; II: $c_T = 1\text{mM}$, $c_P = 1\text{nM}$; III: $c_T = 1\text{mM}$, $c_P = 200\text{mM}$ as used in [121]. Parameters that are the same for all sets I-III: $c_D = 1\text{nM}$, $\kappa = 40d^{-2}$, $\theta^+_{90,30} = 0.1$ and the attempt frequencies k^α_{ij} as given in Fig 7.7. The values of $c_D = c_P = 1\text{nM}$ are a rough estimate because there is no information about these concentrations in [121].

the one-state model, even in this limit, the velocity shows saturation. This is due to the fact that the time scale of the hydrolysis reaction is independent of the ATP concentration and represents the limiting effect for the velocity. The dependence of the average velocity on the ATP concentration is reminiscent of a Michaelis-Menten kinetics and coincides well with experimental results for several different probe particles as shown in [74].

For large beads, the coarse-graining process yields rates that are no longer linear in the corresponding concentrations. In this regime, the sublinear dependence of the velocity on the ATP concentration appears already for smaller ATP concentrations. Comparing the velocity curves of the two-state model with the one-state model, we find that for large beads the velocity curves almost coincide since in this regime the limiting effect for the velocity is the friction experienced by the bead. Thus, using large probe particles, it is not possible to infer the underlying motor dynamics from the characteristics of the velocity as a function of the ATP concentration [136].

Fig. 7.9 shows the coarse-grained forward rates for three different nucleotide concentrations and for various γ chosen as in the experiment [121]. We find that the 90° rate depends only weakly on γ for small ATP concentrations which is reminiscent of the experimental observation that the ATP binding rate to the motor depends only weakly on the size of the probe [121]. However, for large ATP concentrations that were not investigated in the experiment, the 90° rate shows a

strong dependence on γ. This is due to the fact that for small ATP concentrations the relaxation times of all probe particles are in the order of, or even faster than, the motor jump rates. The results for the 30° rate are consistent with experimental results for the hydrolysis rate [121]. Increasing c_{P} decreases the $\mathrm{P_i}$ release rate in the experiment as it decreases the 30° rate here.

7.3.4. Example: Kinesin

As a final more complex example, we apply our coarse-graining method to a model with a multistate motor. We choose the well-studied 6-state-model representing a kinesin motor introduced in [28], and applied in chapter 6.6 to investigate the stall conditions, see Fig. 6.5.

The coarse-grained rates for the mechanical transition are shown in Fig. 7.10. With decreasing γ, the rates approach their fast-bead limit which corresponds to the rates used in [28] while strong deviations occur for finite γ especially for assisting external forces. The friction coefficient of a probe of size 500 nm as in [99] can be calculated using Stokes's law yielding $\gamma \simeq 7.7 \times 10^{-5} d^2/\mathrm{s}$. For friction coefficients in this range (light green line), our coarse-grained rates show a distinct deviation from the one-particle rates (black line). However, the average velocity (obtained from our coarse-grained rates) as function of the external force coincides

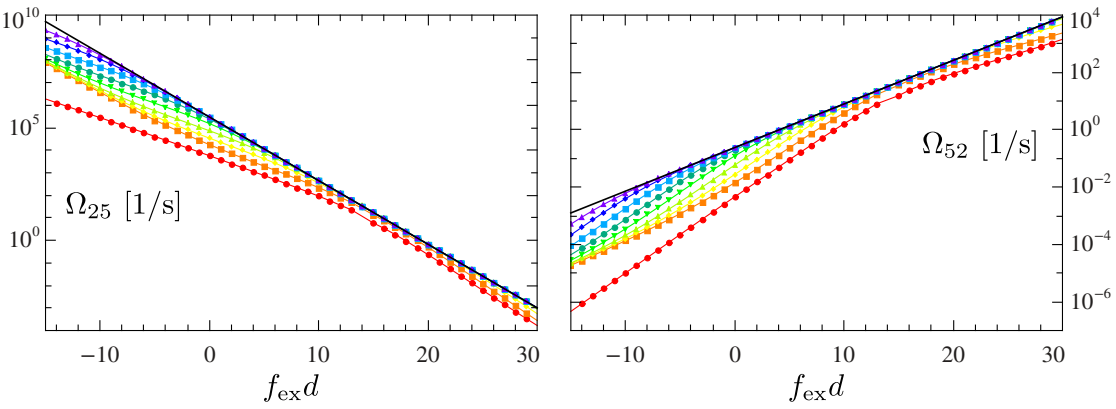

Figure 7.10.: Coarse-grained rates for the mechanical transitions (with y-dependence) for various γ in the range $0.077\,\mathrm{s}/d^2 \geq \gamma \geq 7.7 \times 10^{-10}\,\mathrm{s}/d^2$ (from bottom to top). The rates approach the one-particle rates from [28] (black lines). Parameters: $\kappa = 10\,d^{-2}$ [99], $c_{\mathrm{T}} = 1\,\mathrm{mM}$, $c_{\mathrm{D}} = c_{\mathrm{P}} = 1\,\mathrm{nM}$ (estimated), $\theta^+ = 0.65$, $\chi_{ij} = 0.25, 0.15$, $k_{12}\exp[\mu_T^{\mathrm{eq}}]/c_{\mathrm{T}}^{\mathrm{eq}} = k_{45}\exp[\mu_T^{\mathrm{eq}}]/c_{\mathrm{T}}^{\mathrm{eq}} = 2 \times 10^6\,(\mathrm{Ms})^{-1}$, $k_{21} = k_{23} = k_{34} = k_{56} = k_{61} = 100\,\mathrm{s}^{-1}$, $k_{32}\exp[\mu_D^{\mathrm{eq}}]/c_{\mathrm{D}}^{\mathrm{eq}} = k_{65}\exp[\mu_D^{\mathrm{eq}}]/c_{\mathrm{D}}^{\mathrm{eq}} = 2 \times 10^4\,(\mathrm{Ms})^{-1}$, $k_{43}\exp[\mu_{\mathrm{P}}^{\mathrm{eq}}]/c_{\mathrm{P}}^{\mathrm{eq}} = k_{16}\exp[\mu_{\mathrm{P}}^{\mathrm{eq}}]/c_{\mathrm{P}}^{\mathrm{eq}} = 2 \times 10^4\,(\mathrm{Ms})^{-1}$, $k_{25} = 3 \times 10^5\,\mathrm{s}^{-1}$, $k_{52} = 0.24\,\mathrm{s}^{-1}$, $k_{54} = (k_{52}/k_{25})^2 k_{21}$.

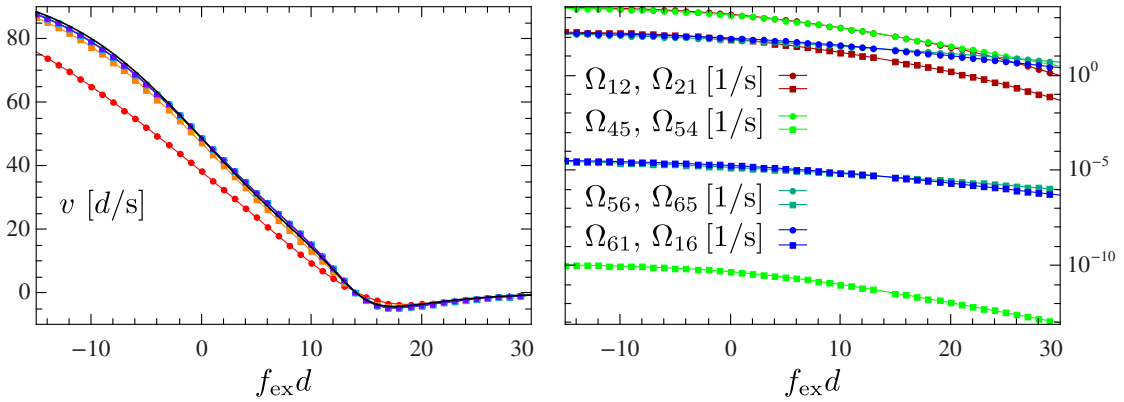

Figure 7.11.: Left: Average velocity for the model with probe particle (colored lines) an the one-particle model from [28] (black). Right: Coarse-grained rates for chemical transitions (with y-dependence) for $\gamma = 0.077\,\mathrm{s}/d^2$. Other parameters as given in Fig. 7.10.

very well for almost all γ with the velocity curve obtained from the bare motor model, see Fig. 7.11. Like for the F_1-ATPase model discussed in section 7.3.3, this agreement is due to the fact that the velocity involves only the difference of the rates multiplied with the marginal distribution. If one investigates only force-velocity curves, the discrepancies between the coarse-grained rates and the one-particle rates are hardly visible.

In contrast to the coarse-grained rates of the F_1-ATPase models, the coarse-grained rates for the mechanical transition of the kinesin model show more structure especially for negative, i.e., assisting external forces. Since the kinesin model contains several internal motor cycles, depending on the external force the dominant cycle can change, leading to crossover regimes with changing weight of the probabilities P_i.

The dependence of the coarse-grained rates for chemical transitions on the external force is visible in Fig. 7.11. Although there is no explicit dependence on external forces for pure chemical rates since $d_{ij}^{\alpha} = 0$, j_{ij}^{α} and P_i depend on f_{ex} via y. The operational current for transitions within the $\mathcal{F}$-cycle in + direction decreases with increasing f_{ex} whereas the operational currents within the $\mathcal{B}$-cycle in + direction slightly increase with f_{ex}, which can be explained intuitively since the motor prefers "backward" cycles for large opposing forces. However, all coarse-grained rates decrease with increasing f_{ex} similarly to the bare motor rates (6.15, 6.16) which decrease with larger y, a situation that is more likely to appear for large external forces.

7.4. Experimental implementation

In order to practically apply the coarse-grained description, one has to determine the marginal distributions P_i, the operational currents j_{ij}^{α}, and the free-energy differences ΔF_{ij}^{α}. For multistate motors, this is a rather challenging task since only a few quantities can be extracted reliably from the experimentally measured trajectory of the probe. Note, however, that this problem does not happen exclusively in our approach but is inevitable whatever method is used to infer motor properties from such trajectories.

In the following, using the 90-30 model for the F_1-ATPase, we will illustrate how these quantities can be estimated. If all motor transitions involve mechanical transitions with different step sizes, the plateaus in the probe trajectory can be assigned to specific corresponding motor states. Since after a large enough time interval all possible transitions will have occurred, one is also able to reconstruct the links connecting the states. The marginal distributions P_i are then given as the fraction of time that the corresponding motor state is occupied. For the two-state model of the F_1-ATPase, we assign plateaus in the probe trajectory that are followed by a fast 90° forward or 30° backward displacement to motor state $i = 1$ and plateaus that are followed by fast 90° backward or 30° forward displacement to $i = 2$. In principle, there are several possibilities to reconstruct hidden variables from partially visible trajectories [189–191]. Here we will use a simple algorithm which sets $i = 2$ if four consecutive data points are within a specific range around 90° and otherwise $i = 1$. The marginal distributions P_1, P_2 are then represented by the fraction of data points with assigned $i = 1, 2$.

If the motor is not very complex, the operational currents j_{ij}^{α} can be obtained rather easily since they are precisely the net currents between two motor states. For unicyclic motors, all operational currents are equal to the average velocity divided by d, the operational current of an ATP binding transition is the net disappearance rate of ATP in the solution (given that there are no other ATP binding reactions), and so on. If all motor transitions involve mechanical transitions with different step sizes, the operational currents between any two states can be obtained by counting the number of transitions of a specific step size from $i \to j$, n_{ij}^{α}, and $j \to i$, n_{ji}^{α}. The instantaneous (operational) current between i and j using α (for any y) is given by

$$j_{ij}^{\alpha}(t) = \sum_k \delta(t - \tau_k) r_{l_k m_k}^{\beta} \tag{7.47}$$

with $r_{l_k m_k}^{\beta} = 1$ if $\beta = \alpha$, $l_k = i$, $m_k = j$ and $r_{l_k m_k}^{\beta} = -1$ if $\beta = \alpha$, $l_k = j$, $m_k = i$ and jump times τ_k. The (time) average of this current using one long trajectory of length t_{tot} is then given by

$$j_{ij}^{\alpha} = (n_{ij}^{\alpha} - n_{ji}^{\alpha})/t_{\mathrm{tot}}. \tag{7.48}$$

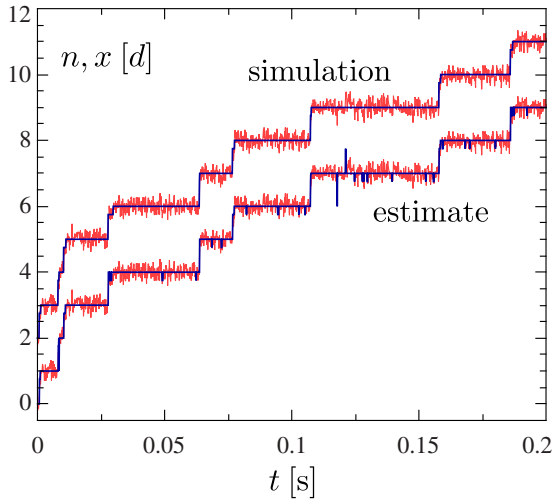

Figure 7.12: Comparison of the simulated trajectory of motor and probe with a trajectory of the probe and the estimated motor position that was reconstructed using the simulated trajectory of the probe. The trajectories are shifted for better visibility. Parameters: $\kappa = 40\,d^{-2}$, $\gamma = 0.005\,\mathrm{s}/d^2$, $c_\mathrm{T} = c_\mathrm{D} = 2\,\mu\mathrm{M}$, $c_\mathrm{P} = 1\,\mathrm{mM}$, $c_\mathrm{T}^\mathrm{eq} = 0.333\,\mu\mathrm{M}$, $c_\mathrm{D}^\mathrm{eq} = 0.0682\,\mathrm{M}$, $c_\mathrm{P}^\mathrm{eq} = 1\,\mathrm{M}$, $f_\mathrm{ex} = 0$, lower boundary to set $i = 2$: $x - \lfloor x \rfloor = 0.375\,d$, upper boundary to set $i = 2$: $x - \lfloor x \rfloor = 0.89\,d$.

In our example, in order to estimate j_{12}^{90} we have to count the number of sudden displacements of "size" 90° either from the trajectory of the probe directly or from the reconstructed trajectory of the motor using the assignment rule mentioned above. If the time resolution of the trajectory is very coarse or if the reconstruction method is rather inaccurate, jumps that consist of fast consecutive 90 and 30 jumps with apparent step size 120° will appear which have to be included in the number of 90° (and also 30°) jumps. Fig. 7.12 shows a reconstructed motor trajectory obtained with the algorithm mentioned above. We have used a trajectory of the probe from our simulations as "experimental data". Compared to the original motor trajectory, this reconstruction captures the average dynamics quite well. Large fluctuations of the probe can generate additional apparent motor jumps in the reconstructed trajectory that are absent in the original one.

Finally, the estimation of the free-energy difference $\Delta F_{ij}^\alpha = F_j - F_i - \Delta\mu_{ij}^\alpha$ is slightly more involved. In equilibrium ($\Delta\mu = 0$, $f_\mathrm{ex} = 0$), detailed balance holds,

$$\frac{w_{ij}^\alpha(y)}{w_{ji}^\alpha(y + d_{ij}^\alpha)} = \frac{p_j^\mathrm{eq}(y + d_{ij}^\alpha)}{p_i^\mathrm{eq}(y)}, \tag{7.49}$$

with the Boltzmann distribution $p_i^\mathrm{eq}(y) = P_i^\mathrm{eq} \exp[-V(y)]/\mathcal{N}$. Inserting this expression yields

$$P_j^\mathrm{eq}/P_i^\mathrm{eq} = \exp[-F_j + F_i + \Delta\mu_{ij}^{\alpha,\mathrm{eq}}] \equiv \exp[-\Delta\mathcal{F}_{ij}^\alpha] \tag{7.50}$$

for the marginal distributions in equilibrium. Note that $\Delta\mu_{ij}^{\alpha,\mathrm{eq}} \neq 0$ if the corresponding transition comprises only binding or release of nucleotides. Thus, the equilibrium free-energy difference $\Delta\mathcal{F}_{ij}^\alpha$ (which explicitly depends on the equilibrium concentrations) can be obtained from the ratio of the marginal distributions

Table 7.1.: Comparison of the coarse-grained rates and other relevant quantities obtained from the simulation of the full model with the ones estimated using the reconstructed motor trajectory. The trajectory used to obtain these values is shown in Fig. 7.12.

	simulation	estimate
P_1	0.944	0.952
P_2	0.056	0.048
j_{12}^{90} [1/s]	52.292	52.246
$\Delta\mathcal{F}_{12}$	3.216	3.140
Ω_{12}^{90} [1/s]	55.325	54.899
Ω_{21}^{90} [1/s]	0.00676	0.00620
Ω_{21}^{30} [1/s]	937.1	1082.37
Ω_{12}^{30} [1/s]	0.037	0.046

under equilibrium conditions. Using $\mu_i = \mu_i^{\mathrm{eq}} + \ln(c_i/c_i^{\mathrm{eq}})$, we find that

$$\Delta F_{ij}^{\alpha} = \Delta\mathcal{F}_{ij}^{\alpha} \pm \sum_k \ln \frac{c_k}{c_k^{\mathrm{eq}}} \tag{7.51}$$

with $k = \mathrm{T}, \mathrm{D}, \mathrm{P}$ and the sign depending on which binding or release event corresponds to the transition ij, α [51]. Hence, the free-energy difference ΔF_{ij}^{α} needed for the coarse-grained rates can be expressed by the equilibrium free-energy difference $\Delta\mathcal{F}_{ij}^{\alpha}$ obtained from experimental data at equilibrium conditions and the nucleotide concentrations with respect to the equilibrium concentrations corresponding to the conditions used to obtain $\Delta\mathcal{F}_{ij}^{\alpha}$. For the 90-30 model, we have $P_2^{\mathrm{eq}}/P_1^{\mathrm{eq}} = \exp[-\Delta\mathcal{F}_{12}^{90}] = \exp[-\Delta\mathcal{F}_{12}^{30}]$ with $-\Delta\mathcal{F}_{12}^{90} = -F_2 + F_1 + \mu_{\mathrm{T}}^{\mathrm{eq}} - \mu_{\mathrm{D}}^{\mathrm{eq}} = -F_2 + F_1 + \mu_{\mathrm{P}}^{\mathrm{eq}} = -\Delta\mathcal{F}_{12}^{30}$ since $\Delta\mu = 0$ in equilibrium.

Once these quantities have been estimated, there are no additional fit parameters needed or left. All concentrations as well as the external force are usually known from the experimental setup. To obtain the coarse-grained rates from the probe trajectory of our 90-30 model, we then proceed as follows. First, we choose equilibrium conditions and obtain $\Delta\mathcal{F}_{12}$ from the ratio of marginal distributions. Then we change to non-equilibrium concentrations and estimate P_1, P_2 and the operational current j_{12}^{90}. The coarse-grained rates, according to Eqs. (7.34, 7.35),

are then given by

$$\Omega_{12}^{90} = j_{12}^{90} \frac{c_{\mathrm{T}} c_{\mathrm{D}}^{\mathrm{eq}} \exp[-\Delta\mathcal{F}_{12} - f_{\mathrm{ex}} d_{12}^{90}]/(c_{\mathrm{T}}^{\mathrm{eq}} c_{\mathrm{D}})}{P_1 c_{\mathrm{T}} c_{\mathrm{D}}^{\mathrm{eq}} \exp[-\Delta\mathcal{F}_{12} - f_{\mathrm{ex}} d_{12}^{90}]/(c_{\mathrm{T}}^{\mathrm{eq}} c_{\mathrm{D}}) - P_2}, \tag{7.52}$$

$$\Omega_{21}^{90} = j_{12}^{90} \frac{1}{P_1 c_{\mathrm{T}} c_{\mathrm{D}}^{\mathrm{eq}} \exp[-\Delta\mathcal{F}_{12} - f_{\mathrm{ex}} d_{12}^{90}]/(c_{\mathrm{T}}^{\mathrm{eq}} c_{\mathrm{D}}) - P_2}, \tag{7.53}$$

$$\Omega_{21}^{30} = j_{12}^{90} \frac{c_{\mathrm{P}}^{\mathrm{eq}} \exp[\Delta\mathcal{F}_{12} - f_{\mathrm{ex}} d_{21}^{30}]/c_{\mathrm{P}}}{P_2 c_{\mathrm{P}}^{eq} \exp[\Delta\mathcal{F}_{12} - f_{\mathrm{ex}} d_{21}^{30}]/c_{\mathrm{P}} - P_1}, \tag{7.54}$$

$$\Omega_{12}^{30} = j_{12}^{90} \frac{1}{P_2 c_{\mathrm{P}}^{\mathrm{eq}} \exp[\Delta\mathcal{F}_{12} - f_{\mathrm{ex}} d_{21}^{30}]/c_{\mathrm{P}} - P_1}. \tag{7.55}$$

A comparison of the coarse-grained rates and related quantities obtained from the full theoretical model and from the reconstructed one estimated using the probe trajectory is shown in table 7.1. We find quite good agreement between the original and the reconstructed quantities with a maximum error of 14% except for the Ω_{ij}^{30} rates which have a maximum error of 24%.

The 90-30 model thus provides a useful demonstration of the experimental applicability of the coarse-graining method showing that it is possible to estimate the coarse-grained rates from experimental accessible data if the underlying motor network is not too complex. Considering the simplicity of the applied reconstruction method, the accuracy of the estimates is rather encouraging.

7.5. Invariance of entropy production and efficiency

An important question for any coarse-graining method concerns its effect on entropy production. In general, a coarse-grained description without imposed time-scale separation or detailed balance for the eliminated variables often underestimates the entropy production of the system [170–173, 181]. In this section, we show that for the type of models considered here, our coarse-graining method conserves the entropy production even if there is no time-scale separation between the eliminated and remaining degree of freedom.

Since transitions can be uniquely attributed to motor or probe particle, the total entropy production of the system [6] can be split in two parts, analogously to bipartite or partially masked systems [192, 193],

$$\begin{aligned}\dot{S}^{\mathrm{tot}} &= \sum_i \int_{-\infty}^{\infty} \frac{\gamma j_i^{x2}(y)}{p_i(y)} \mathrm{d}y \\ &+ \sum_{i,j,\alpha} \int_{-\infty}^{\infty} p_i(y) w_{ij}^{\alpha}(y) \ln \frac{p_i(y) w_{ij}^{\alpha}(y)}{p_j(y + d_{ij}^{\alpha}) w_{ji}^{\alpha}(y + d_{ij}^{\alpha})} \mathrm{d}y \\ &\equiv \dot{S}_{\mathrm{p}}^{\mathrm{tot}} + \dot{S}_{\mathrm{m}}^{\mathrm{tot}}\end{aligned} \tag{7.56}$$

where $j_i^x(y) = ((\partial_y V(y) - f_{\mathrm{ex}})p_i(y) + \partial_y p_i(y))/\gamma$ is the current due to the motion of only the bead for fixed i. Obviously, both $\dot{S}_{\mathrm{p}}^{\mathrm{tot}}$ and $\dot{S}_{\mathrm{m}}^{\mathrm{tot}}$ are non-negative.

The total entropy production (7.56) can be calculated using the LDB condition (3.9) as

$$\begin{aligned}\dot{S}^{\mathrm{tot}} =& \sum_i \int_{-\infty}^{\infty} (\partial_y V(y) - f_{\mathrm{ex}}) j_i^x(y) \mathrm{d}y \\ &+ \sum_{i,j,\alpha} \int_{-\infty}^{\infty} p_i(y) w_{ij}^{\alpha}(y) \left(\Delta\mu_{ij}^{\alpha} - F_j + F_i - V(y + d_{ij}^{\alpha}) + V(y)\right) \mathrm{d}y \\ =& \sum_{i<j,\alpha} \Delta\mu_{ij}^{\alpha} j_{ij}^{\alpha} - f_{\mathrm{ex}} v \geq 0. \end{aligned} \tag{7.57}$$

Using partial integration, it can be easily seen that the parts involving $V(y)$ cancel, i.e., the energy of the linker is constant on average. The total entropy production is then given by the chemical free-energy consumption that is not transformed into mechanical power.

For the coarse-grained description, the total entropy production contains only contributions from the effective jump process,

$$\dot{S}_{\mathrm{cg}}^{\mathrm{tot}} = \sum_{i,j,\alpha} P_i \Omega_{ij}^{\alpha} \ln \frac{P_i \Omega_{ij}^{\alpha}}{P_j \Omega_{ji}^{\alpha}} = \sum_{i,j,\alpha} P_i \Omega_{ij}^{\alpha} \ln \frac{\Omega_{ij}^{\alpha}}{\Omega_{ji}^{\alpha}}. \tag{7.58}$$

Using the LDB condition for the coarse-grained rates (7.30) and the condition on the operational current (7.31) yields

$$\dot{S}_{\mathrm{cg}}^{\mathrm{tot}} = \sum_{i<j,\alpha} \Delta\mu_{ij}^{\alpha} j_{ij}^{\alpha} - f_{\mathrm{ex}} v \tag{7.59}$$

which is precisely (7.57). For these models for which the state space of the eliminated degree of freedom does not contain entropy producing internal cycles, the average total entropy production in the NESS remains invariant under our coarse-graining procedure.

It is also instructive to apply the entropy-splitting scheme introduced in [172] to our coarse-graining procedure. In [172], it was shown that the total entropy production can be written as a sum of the coarse-grained entropy production (7.58) plus a contribution of the microstates corresponding to a mesostate (which are eliminated during coarse-graining) plus a contribution due to the fact that jumps between mesostates can occur involving different microstates. In our framework, the total entropy production is already recovered by the coarse-grained entropy production. The two additional contributions which correspond to the total entropy production of the probe particle and the average total entropy production of the motor minus the coarse-grained entropy production cancel each other.

We finally show that our coarse-graining procedure also preserves the energy transduction, or thermodynamic, efficiency η_T defined as the ratio of the extractable power $\dot{W}_{\text{out}}$ and the rate of chemical energy input $\dot{\Delta}\mu$ [132, 155],

$$\eta_T \equiv \frac{\dot{W}_{\text{out}}}{\dot{\Delta}\mu}. \tag{7.60}$$

For the systems we have studied so far, as long as the external force is smaller than the stall force, the power output is given by $\dot{W}_{\text{out}} = f_{\text{ex}} v$ and the power input by $\sum_{i<j,\alpha} \Delta\mu_{ij}^{\alpha} j_{ij}^{\alpha}$ which leads to the efficiency

$$\eta_T = \frac{f_{\text{ex}} v}{\sum_{i<j,\alpha} \Delta\mu_{ij}^{\alpha} j_{ij}^{\alpha}}, \tag{7.61}$$

which is the same in the coarse-grained description since v, j_{ij}^{α}, and $\Delta\mu_{ij}^{\alpha}$ are conserved.

For motor models with tight coupling or multistate models with a single motor cycle, the rate of chemical energy input equals the velocity $\dot{\Delta}\mu = v\Delta\mu/d$ and the efficiency reduces to $\eta_T = f_{\text{ex}}/\Delta\mu$. In general, however, any idle cycles of the motor increases the rate of chemical input over the velocity and therefore reduces the efficiency (see section 6.5).

7.6. Stall force and rate anomaly

In chapter 6 we have shown that for multicyclic motors, the stall force becomes a function of the attached probe particle. The varying stall force has also implications on the coarse-grained transition rates. In Fig. 7.10, a close look around $f_{\text{ex}} d = 14$ shows that these data points are missing for the following reason. For all investigated models, we find that if, as a function of the external force, the sign change of an operational current depends on the friction coefficient γ, the coarse-grained rates corresponding to this transitions can become piecewise negative. This phenomenon occurs when the affinity of the affected transitions, $\ln\left[P_i \Omega_{ij}^{\alpha}/(P_j \Omega_{ji}^{\alpha})\right]$, has the opposite sign of j_{ij}^{α}. An isolated sign change in the denominator of Eqs. (7.34, 7.35) leads to a pole in the corresponding rate. Such an anomaly in Ω_{ij}^{α} necessarily implies a corresponding one in Ω_{ji}^{α} since the ratio of the effective rates obeys the local detailed balance condition which enforces the same sign for both rates. In this range, the coarse-graining scheme introduced here fails to produce physically acceptable rates. In practice, one should discard the results at least when either a rate is negative or becomes larger than the rate for vanishing bead size. In Fig. 7.13, where we zoom into the range around the stall force, this range is shaded grey. Taken at face value, this phenomenon looks like a shortcoming of

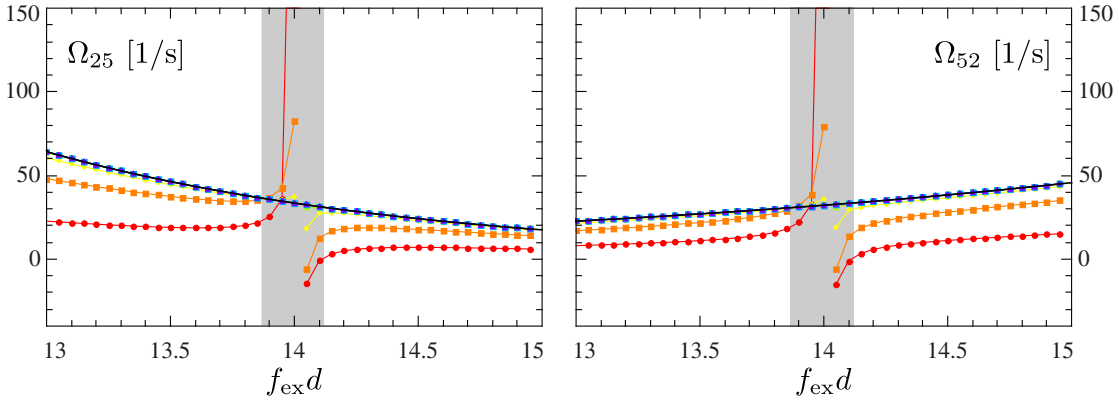

Figure 7.13.: Detail of the coarse-grained mechanical transition rates of the kinesin model as shown in Fig. 7.10. Near the stall force at $f_{\mathrm{ex}}d \simeq 14$ these rates exhibit a pole. In the grey shaded range, they should not be interpreted as physical transition rates.

our approach. It is the price to pay for requiring over the full parameter range both the local detailed balance condition and the correct net currents from any one motor state to any other. While the negative rates do not allow for a sensible physical interpretation, they nevertheless can be used to calculate average quantities and yield, e.g., the correct entropy production as shown in section 7.5.

This rate anomaly does not occur for one-state motor models since their coarse-grained rates can be expressed in terms of directed cycle currents of the full network, which are always positive (see section 7.2.2). Concerning multistate motor models, we have shown in section 6.3 that for unicyclic as well as for specific multicyclic motors the probability distribution at stall conditions is given by a shifted Boltzmann distribution (6.10). Then, in the limit of continuous y, the zero of the operational current (7.32) implies

$$0 = \ln\left[\frac{\int_{-\infty}^{\infty} p_i(y) w_{ij}^{\alpha}(y)\,\mathrm{d}y}{\int_{-\infty}^{\infty} p_j(y+d_{ij}^{\alpha}) w_{ji}^{\alpha}(y+d_{ij}^{\alpha})\,\mathrm{d}y}\right] \tag{7.62}$$

$$= \ln\left[\frac{P_i^{\mathrm{st}} \int_{-\infty}^{\infty} w_{ij}^{\alpha}(y) \exp[-V(y) + f_{\mathrm{ex}}^{\mathrm{st}} y]}{P_j^{\mathrm{st}} \int_{-\infty}^{\infty} w_{ji}^{\alpha}(y+d_{ij}^{\alpha}) \exp[-V(y+d_{ij}^{\alpha}) + f_{\mathrm{ex}}^{\mathrm{st}}(y+d_{ij}^{\alpha})]}\right] \tag{7.63}$$

$$= \ln\left[\frac{P_i^{\mathrm{st}}}{P_j^{\mathrm{st}}} \exp[-\Delta F_{ij}^{\alpha} - f_{\mathrm{ex}}^{\mathrm{st}} d_{ij}^{\alpha}]\right] \tag{7.64}$$

$$= \ln\left[\frac{P_i^{\mathrm{st}} \Omega_{ij}^{\alpha}}{P_j^{\mathrm{st}} \Omega_{ji}^{\alpha}}\right], \tag{7.65}$$

where we have used the transition rates in the form of (3.10, 3.11). Thus, for models that exhibit a shifted Boltzmann distribution at stall, the sign change of

the current j_{ij}^{α} and the affinity $\ln\left[P_i\Omega_{ij}^{\alpha}/(P_j\Omega_{ji}^{\alpha})\right]$ around stall conditions occurs for the same f_{ex}. For those models, the coarse-grained rates are well-defined and positive around the stall force.

Note that the stall force of models showing a shifted Boltzmann distribution, as investigated in section 6.3, is independent of the friction coefficient γ. This finding is consistent with the observation mentioned above that negative rates occur when the stall force depends on γ. Based on these results, one might conjecture that if the stall force is independent of the properties of the probe, the coarse-grained rates are positive. However, a derivation of the precise conditions under which for multistate motor models a pair of effective rates is well-defined and positive over the complete range of f_{ex} must be left to future work. We stress, however, that in all examples shown in this study, this anomaly occurs only in the narrow range shown in Fig. 7.13. From a practical point of view, it therefore may not be as relevant as it is intriguing from a theoretical perspective.

7.7. Conclusion

In this chapter, we have introduced a systematic coarse-graining method that allows us to reduce motor-bead models to effective one-particle motor models. This coarse-graining procedure provides a compromise between a one-particle description that is simple to handle and a detailed model comprising the dynamics of the full system. It yields an effective one-particle model maintaining the true motor network, where the influence of the probe is naturally incorporated without any additional assumptions since the simplification of the description takes place *a posteriori*. Any external force acting on the probe is then acting on the effective motor directly. The coarse-grained rates obey a LDB condition and yield the correct net currents. Fixing the marginal distribution and the average currents, there is still freedom on how to choose the rates. Only with the LDB condition the effective rates are determined uniquely.

Applying the coarse-graining procedure to motor-bead models, we find that in general the coarse-grained rates do not show a single exponential dependence on the external force in contrast to what is often assumed for mechanical transition rates in one-particle models. Only in the often unrealistic limit of fast bead relaxation, the coarse-grained rates reduce to the corresponding one-particle rates.

In the absence of external forces, in general the coarse-grained rates are not proportional to the ATP concentration even if the motor rates obey mass action law kinetics. This feature originates from the drag effect of probe (due to friction) that is incorporated in the coarse-grained rates. For the same reason, the average velocity shows a sublinear dependence on the ATP concentration even for a one-state motor model. Assuming an *a priori* one-particle model with external force

acting directly on the motor, one would have either to use a rather counterintuitive complex force-dependence of the transition rates or to introduce additional motor states in order to obtain a sublinearly growing velocity caused by the drag of the probe.

Considering the influence of the coarse-graining procedure on the stochastic thermodynamics of the system, we show that the total entropy production remains invariant under coarse-graining. This is due to the fact that, on the one hand, the state space of the eliminated degree of freedom contains no entropy producing cycles. On the other hand the design of the coarse-graining procedure is also important. It has to conserve the motor network as well as the net currents and provide transition rates fulfilling a LDB condition. Likewise, the thermodynamic efficiency remains invariant in our scheme.

Our coarse-graining method conserves average quantities like the entropy production or operational currents although eliminating the dynamics of the probe particle strongly affects the cycle structure of the full system. In order to preserve also fluctuations of current observables in the long-time limit it was found that coarse-graining methods should conserve the cycle structure of the full system [177, 178].

From the experimental point of view, in order to obtain the simpler effective model, the underlying mesoscopic modeling need not to be known since all these quantities enter the coarse-grained description via the net currents and the marginal distributions which, in principle, can be extracted from the experimental data as we have demonstrated using a two-step model for the F_1-ATPase.

The main advantage of the coarse-graining procedure introduced here is that once the rates have been obtained from experimentally accessible quantities, they automatically fulfill a LDB condition and provide the correct average currents, i.e., velocity, entropy production, hydrolysis rate, and so on.

For multicyclic motors, the coarse-graining procedure can yield rates that can have poles and become (piecewise) negative. If this scenario occurs, the coarse-grained rates lack a physical interpretation as transition probabilities in this range but they can still be used to calculate average quantities. For this class of motors the stall force typically depends on the size of the probe particle, i.e., the friction coefficient. For one-state motors, the coarse-grained rates are always positive.

So far, we have discussed coarse-graining only under NESS conditions. In principle, the coarse-graining procedure as introduced in sections 7.2.1 and 7.3.1 can also be applied to non-stationary states, e.g., if the nucleotide concentrations are not constant and $\Delta\mu$ decreases with time [51, 194]. Such a scenario would yield time-dependent P_i's, net currents, LDB conditions, and therefore also time-dependent coarse-grained rates.

Further generalizations might include other types of models representing the

full system. While developed here for discrete motor models, the coarse-graining procedure should be also applicable to continuous motors moving in a tilted periodic potential where the potential minima will become the discrete states of the coarse-grained effective motor. The introduction of the index α in principle also accounts for more involved potentials or free-energy surfaces that depend on both the motor and the probe state.

8. Concluding perspective

Most single molecule experiments with molecular motors comprise some kind of probe particle that is attached to the motor. Thus, any theoretical modeling with parameters estimated from experimental data will explicitly or implicitly contain characteristics of the probe particle.

In this thesis, we have studied the influence of an attached probe particle on the dynamics and energetics of a single motor. In particular, we find that specific features in experimental data can result from attaching probe particles and do not necessarily represent characteristics of the motor itself.

Our analysis is based on a so-called hybrid model as introduced in chapter 3. Within the hybrid model, the motor and the probe are modeled as two coupled degrees of freedom. Such modeling is suitable to investigate the interaction effects between motor and probe since it treats both constituents on an equal footing.

We have applied this hybrid model to explore three different definitions of efficiency applicable to molecular motor-probe setups in chapter 4. We find that the pseudo efficiency which represents a measure of how much chemical energy can be transferred to the linker can indeed exceed 1. This result was later affirmed by [17]. The pseudo efficiency is not bounded by 1 since it involves heat dissipated by the probe rather than work that is extracted from the system. The genuine thermodynamic efficiency η_{T}, which is bounded by 1 due to the second law, reaches 1 at stall conditions since our model comprises a tightly coupled one-state motor. Experiments on the F_1-ATPase indicate that this specific motor is indeed tightly coupled and reaches $\eta_{\mathrm{T}} = 1$ at stall consistent with our modeling.

Information about the influence of the probe on the dynamics of the motor can be obtained from the velocity autocorrelation function (VACF) and the response function of the velocity of the probe. Both quantities have also been measured in experiments with the F_1-ATPase. Simulations reveal that the VACF and the response function of the hybrid model can show pronounced oscillatory behavior. Analyzing three simplified versions of our hybrid model, we find that these oscillations emerge if the motor advances with discrete jumps that are not purely random in time and if its dynamics is affected by the external force. The observed regularity in the dynamics of the motor can be induced by a symmetric coupling between motor and probe even if the motor jumps are *a priori* purely random. Moreover, the linker transmits any external perturbation that was originally applied only to the probe to the motor. A structure similar to the oscillations in the

simulation data, however less pronounced, also occurs in the experimental data. The dwell-time distribution of the motor jumps can exhibit non-Markovian characteristics due to the delayed relaxation of the probe which could be mistaken as signature of additional motor states.

More general aspects concerning generic unicyclic and multicyclic motors are addressed in the remaining chapters. After introducing the network representation of the hybrid models, we show that the presence of a probe particle augments the network of the motor such that it comprises more cycles than the bare motor network. Due to these additional cycles, the stall force of motor-probe complexes with multicyclic motors can depend on the size of the probe. In particular, the stall force of the motor-probe complex can be smaller, equal to or even larger than the stall force of the bare motor. Hence, it is possible to increase the maximum extractable work from the motor by applying a probe particle. Since unicyclic motors do not show a varying stall force with probe size, this feature can serve as proof for a multicyclic motor. Concerning experiments, one has to keep in mind that the measured stall force corresponds to the motor-probe complex and does not necessarily represent characteristics of the energy transduction in the bare motor.

While the previous chapters involved hybrid-models with explicit dynamics of the probe particle, the last chapter provides a dynamically and thermodynamically consistent coarse-graining procedure which allows to map the motor-probe complex to an effective one-particle motor model. The so-obtained effective motor model can then be compared to the traditionally used *a priori* one-particle motor models as briefly mentioned in the chapters 1 and 2. The rates of the effective motor model exhibit a more complex dependence on external parameters like force or ATP concentration than the rates of the *a priori* one-particle models. Since the coarse-grained network equals the bare motor network, the coarse-graining method provides a link between the detailed hybrid models and findings that have been obtained using one-particle models. Any net current observable can be calculated directly on the coarse-grained network yielding the correct result of the underlying detailed dynamics.

After summarizing our main results, we will now briefly address remaining open issues. In the first place, it is unknown which features in the experimental data can be attributed to the interactions between motor and probe. Thus, we started our analysis in chapters 4 and 5 with a simple, well-defined model to identify the implications of attaching a probe particle to the motor. Since any extension of the model comes along with additional fit parameters and a much more complicated analysis, we have remained with the simple one-state model and the harmonic linker for the most part. The basic properties of motor-bead interaction are already captured by this simple setup, which provides deeper insights into the origin of

the observed effects. However, as we have seen in chapters 4 and 5, quantitative comparison with experimental data requires more sophisticated models including, e.g., additional internal motor states or a more complex linker potential. In a next step, once the contributions of the probe have been identified, the hybrid model can be extended to better represent the complex structure of the actual molecular motor.

Besides adjusting or improving the hybrid model, our analysis has revealed more general issues that could provide a starting point for further studies. One of these issues is the regularity that the probe induces in the dynamics of the motor. Following [164, 165] it would be interesting to further investigate the shape of the dwell-time distribution of the motor-probe complex. Here, the additional internal states belong to the probe particle. One might envisage a chain of states with a random number of intermediate states representing y that could serve as a simplified test model to gain deeper insight into the suppression of subsequent motor jumps. Since the diffusion coefficient provides a measure of the "randomness" of the dynamics, one can expect that the randomness parameter, a quantity comparing the diffusion coefficient with the average velocity of the motor, will also be affected by the presence of a probe particle.

The observed stall force variation for multicyclic motors involves several additional open questions. Our numerical investigations indicate an optimal probe size where the deviation of the stall force from the stall force of the bare motor is maximal. Here, additional work is required to find out whether this is a generic effect and whether the extracted work can be maximized as a function of the probe size. We also found that the occurrence of negative coarse-grained rates with poles is connected with the stall force anomaly. We have shown that for specific models, the coarse-grained rates do not have poles at the stall force. However, we cannot exclude additional poles in the coarse-grained rates away from the stall force. Furthermore, it would be interesting to know whether a stall force that is independent of the friction coefficient γ implies positive coarse-grained rates as suggested by our numerical results. Additionally, we have investigated the stall force only as a function of the probe size. Since the variation of the stall force is induced by the delayed relaxation of the probe, it is obvious that the stall force should be also a function of the coupling strength , i.e., the potential $V(y)$, or, especially the spring constant κ.

Further studies should address the efficiency at maximum power (EMP) for hybrid models, especially those with multicyclic motors. We have already seen that the maximum extractable work can be increased by adding a probe particle but that does not necessarily increase the efficiency or efficiency at maximum power. Hence, additional work is required to find out how the probe affects the EMP and whether there is an optimal probe size to maximize the EMP.

A. Simulation algorithm

Trajectories of the hybrid models introduced in chapter 3 are simulated using a Gillespie algorithm [195, 196] very similar to the one used in [41]. Therefore, we discretize the dynamics of the probe particle yielding a fully discrete two-dimensional (n, x) or, for multistate motors three-dimensional (i, n, x), state space, see Fig. A.1. For each state, jumps of the motor or the probe can occur changing i, n or x, respectively. The main advantage of using a fully discretized state space is that the transition rates for each state are independent of time or any previous transitions of the system. Hence, on the (i, n, x)-space, the process is a pure Markov process and can be simulated with the simple algorithm presented below.

The transition rates of the probe can be obtained by discretizing the corresponding part of the Fokker-Planck equation (3.6, 3.12) yielding

$$\gamma^+(y) = \frac{\partial_y V(y) - f_{\text{ex}}}{2\gamma\delta} + \frac{1}{\gamma\delta^2}, \tag{A.1}$$

$$\gamma^-(y) = -\frac{\partial_y V(y) - f_{\text{ex}}}{2\gamma\delta} + \frac{1}{\gamma\delta^2} \tag{A.2}$$

which corresponds to the first-order expansion of the rates

$$\gamma^+(y) = \frac{1}{\gamma\delta^2} \exp[-V(y - \delta/2) + V(y) - f_{\text{ex}}\delta/2], \tag{A.3}$$

$$\gamma^-(y) = \frac{1}{\gamma\delta^2} \exp[-V(y + \delta/2) + V(y) + f_{\text{ex}}\delta/2] \tag{A.4}$$

with $\partial_y V(y) \approx 2(V(y + \delta/2) - V(y))/\delta$. The step size δ of the probe is chosen as $\delta = d/1000$. We use the latter definition of the transition rates since these hold true also for larger δ and obey a LDB condition.

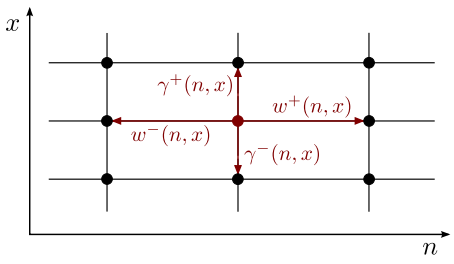

Figure A.1: Two-dimensional state space (n, x) for a hybrid model with a one-state motor. The actual state of the system (dark red) can be changed via four transitions in n or x direction, representing jumps of the motor or the probe, respectively.

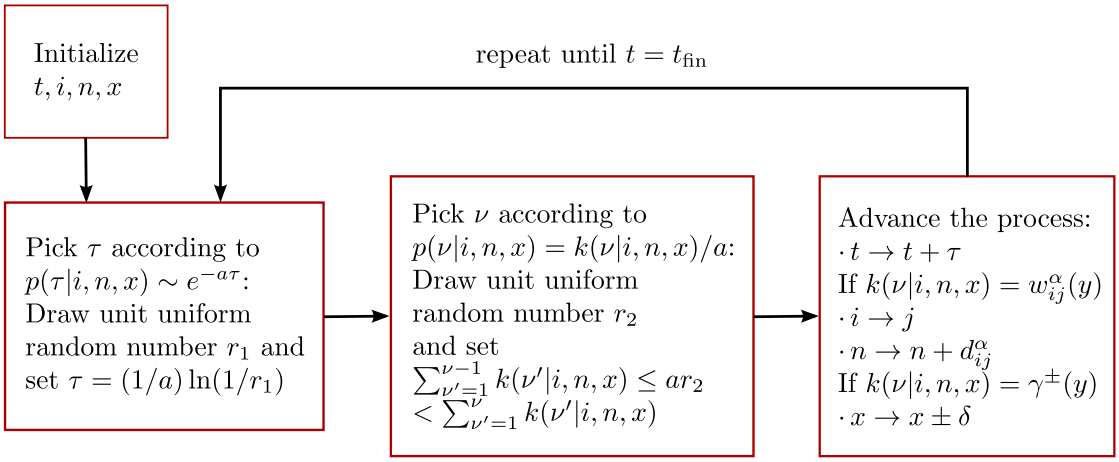

Figure A.2.: Schematic illustration of the Gillespie algorithm applied to generate stochastic trajectories of the hybrid models.

Fig. A.2 shows a flow chart of the simulation algorithm. We start with initializing $t = 0$, $n = 0$, $x = 0$ and then determine the next jump time. The jump times are exponentially distributed $p(\tau|i,n,x) \sim \exp[-a\tau]$ since all transition rates of the system are independent of t and depend only on the actual state (i,n,x). The exit rate from state i to all other states linked to i reads

$$a(i,n,x) = \sum_{\nu} k(\nu|i,n,x) \tag{A.5}$$

where $\nu = 1, 2, ...$ indicates the specific transition or direction and $k(\nu|i,n,x)$ represents $w_{ij}^{\alpha}(y)$ or $\gamma^{\pm}(y)$. Sample values of the jump times are obtained by drawing unit uniform random numbers r_1 and setting $\tau = (1/a)\ln(1/r_1)$ [196]. In the next step, one has to chose the direction ν of the jump. The specific transition can be chosen by drawing another unit uniform random number r_2 and setting ν according to

$$\sum_{\nu'=1}^{\nu-1} k(\nu|i,n,x) \leq ar_2 < \sum_{\nu=1}^{\nu} k(\nu|i,n,x). \tag{A.6}$$

Now, the process can be updated depending on whether ν represents a jump of the probe or of the motor and the next jump time can be picked. Depending on the later purpose of the trajectory, the data can be recorded at various points throughout the algorithm.

B. Equivalence of heat flow $\dot{Q}_{\mathrm{P}}$ with the one inferred from the Harada-Sasa relation

Experimentally, the heat flow caused by the probe has been inferred from measuring the autocorrelation function $C_{\dot{x}}(\tau) = \langle \dot{x}(t+\tau)\dot{x}(t)\rangle - v^2$ and the linear response function

$$R_{\dot{x}}(\tau) \equiv \frac{\delta\langle \dot{x}(t+\tau)\rangle}{\delta h(t)}\Big|_{h=0} \tag{B.1}$$

of the velocity of the probe to a small external perturbation $h(t)$ of the probe within the steady state [15]. The heat flow is then given by an equality derived by Harada and Sasa [156]

$$\begin{aligned} \dot{Q}^{\mathrm{HS}} &= \gamma v^2 + \gamma \textstyle\int_{-\infty}^{\infty} \frac{\mathrm{d}\omega}{2\pi}[\tilde{C}_{\dot{x}}(\omega) - 2\Re\left(\tilde{R}_{\dot{x}}(\omega)\right)] \\ &= \gamma v^2 + \gamma[C_{\dot{x}}(0) - 2R_{\dot{x}}(0)] \qquad \text{(B.2)} \\ &\equiv \dot{Q}_{\mathrm{S}} + \dot{Q}_{\mathrm{V}}, \qquad \text{(B.3)} \end{aligned}$$

with $\tilde{C}_{\dot{x}}$ and $\tilde{R}_{\dot{x}}$ being the Fourier transforms of $C_{\dot{x}}$ and $R_{\dot{x}}$. Using a path weight approach described in [160] applied to our system, the response function follows as

$$R_{\dot{x}}(\tau) = \frac{1}{2}\langle \dot{x}(t+\tau)[\dot{x}(t) - \frac{1}{\gamma}(\kappa y(t) - f_{\mathrm{ex}})]\rangle. \tag{B.4}$$

Inserting $C_{\dot{x}}$ and this $R_{\dot{x}}$ into (B.2), one immediately finds

$$\dot{Q}^{\mathrm{HS}} = \langle \dot{x}(\kappa y - f_{\mathrm{ex}})\rangle \tag{B.5}$$

which is equal to $\dot{Q}_{\mathrm{P}}$ in (4.9).

C. Efficiency of the hybrid model with continuous motor dynamics

For continuous motor dynamics as investigated in section 5.2.3, Eqs. (5.20, 5.21), the heat flow through the probe is given by

$$\dot{Q}_{\mathrm{P}} = \frac{\gamma \Delta\mu^2}{d^2(\eta+\gamma)^2} = \gamma v^2 \tag{C.1}$$

which is equal to the contribution appearing in the Stokes efficiency. Thus, the pseudo efficiency and the Stokes efficiency coincide and are given by

$$\eta_{\mathrm{Q,S}} = \frac{\gamma v^2 d}{\Delta\mu v} = \frac{\gamma}{\eta+\gamma}. \tag{C.2}$$

If the diffusion coefficient of the motor is much larger than the one of the probe,

$$\eta \ll \gamma \quad \Rightarrow \quad \eta_{\mathrm{Q,S}} \to 1 \tag{C.3}$$

and in the opposite case,

$$\eta \gg \gamma \quad \Rightarrow \quad \eta_{\mathrm{Q,S}} \to 0. \tag{C.4}$$

Thus, the limiting cases (for the Stokes efficiency) are reached when there is a time-scale separation between the dynamics of the motor and the probe.

One can now investigate the original model with discrete motor dynamics as used in chapter 4 in view of a time-scale separation between the dynamics of motor and probe. The diffusion coefficient of the bare motor which corresponds to η is given by

$$D_{\mathrm{m}}^{\mathrm{bare}} = d^2 \frac{w_0 \exp[\mu_{\mathrm{T}}] + w_0 \exp[\mu_{\mathrm{D}} + \mu_{\mathrm{P}}]}{2} = d^2 \frac{w^{\mathrm{eq}}(c_{\mathrm{T}}/c_{\mathrm{T}}^{\mathrm{eq}} + c_{\mathrm{D}} c_{\mathrm{P}}/(c_{\mathrm{D}}^{\mathrm{eq}} c_{\mathrm{P}}^{\mathrm{eq}}))}{2}, \tag{C.5}$$

which increases with $\Delta\mu$ for fixed w^{eq} since μ_{D} and μ_{P} are fixed in the setup of chapter 4 and also with w^{eq} for fixed $\Delta\mu$ since then the ratio of c_i/c_i^{eq} is fixed. Thus, in the setup with fixed w^{eq}, see Figs. 4.1, 4.3, the pseudo and the Stokes efficiency should approach 1 with increasing $\Delta\mu$ and 0 with decreasing $\Delta\mu$. For

fixed $\Delta\mu$, they should approach 1 with increasing w^{eq} and 0 with decreasing w^{eq}, see Fig. 4.1, 4.3. While the Stokes efficiency exhibits the predicted behavior, the pseudo-efficiency deviates for small $\Delta\mu$ except for $\theta^+ = 0.5$. Obviously, the specific characteristics for $\theta^+ = 0.5$ is related to the fact that discretizing continuous dynamics yield precisely $\theta^+ = \theta^- = 0.5$.

Bibliography

[1] R. Brown. XXVII. A brief account of microscopical observations made in the months of June, July and August 1827, on the particles contained in the pollen of plants; and on the general existence of active molecules in organic and inorganic bodies. *Philosophical Magazine Series 2*, 4(21):161–173, 1828.

[2] A. Einstein. Über die von der molekularkinetischen Theorie der Wärme geforderte Bewegung von in ruhenden Flüssigkeiten suspendierten Teilchen. *Ann. Phys.*, 17:549, 1905.

[3] M. von Smoluchowski. Zur kinetischen Theorie der Brownschen Molekularbewegung und der Suspensionen. *Ann. Phys.*, 326(14):756–780, 1906.

[4] M. P. Langevin. Sur la théorie du mouvement brownien. *Comptes Rend. Acad. Sci. (Paris)*, 146:530, 1908.

[5] C. Bustamante, J. Liphardt, and F. Ritort. The nonequilibrium thermodynamics of small systems. *Physics Today*, 58(7):43, 2005.

[6] U. Seifert. Stochastic thermodynamics, fluctuation theorems, and molecular machines. *Rep. Prog. Phys.*, 75:126001, 2012.

[7] K. Sekimoto. *Stochastic Energetics*. Springer, Berlin, Heidelberg, 2010.

[8] R. Klages, W. Just, and C. Jarzynski, editors. *Nonequilibrium Statistical Physics of Small Systems: Fluctuation relations and beyond*. Reviews of Nonlinear Dynamics and Complexity. Wiley-VCH, Weinheim, 2012.

[9] J. Howard. *Mechanics of Motor Proteins and the Cytoskeleton*. Sinauer, New York, 1 edition, 2001.

[10] M. Schliwa. *Molecular Motors*. Wiley-VCH, Weinheim, 2003.

[11] R. Phillips, J. Kondev, and J. Theriot. *Physical Biology of the Cell*. Garland Science, Taylor & Francis Group, LLC, 2009.

[12] The Nobel Prize in Chemistry 1997. *Nobelprize.org*. Nobel Media AB 2014. Web. 20 Jan 2015.

[13] P. Nelson. *Biological Physics: Energy, Information, Life*. W. H. Freeman and Company, 2004.

[14] F. Ritort. Single-molecule experiments in biological physics: methods and applications. *J. Phys.: Condens. Matter*, 18:R531, 2006.

[15] S. Toyabe, T. Okamoto, T. Watanabe-Nakayama, H. Taketani, S. Kudo, and E. Muneyuki. Nonequilibrium energetics of a single F_1-ATPase molecule. *Phys. Rev. Lett.*, 104:198103, 2010.

[16] E. Zimmermann and U. Seifert. Efficiency of a molecular motor: A generic hybrid model applied to the F_1-ATPase. *New J. Phys.*, 14:103023, 2012.

[17] K. Kawaguchi, S. Sasa, and T. Sagawa. Nonequilibrium dissipation-free transport

in F_1-ATPase and the thermodynamic role of asymmetric allosterism. *Biophys. J.*, 106:2450–2457, 2014.

[18] J. Howard, A. J. Hudspeth, and R. D. Vale. Movement of microtubules by single kinesin molecules. *Nature*, 342:154–158, 1989.

[19] R. D. Vale, T. Funatsu, D. W. Pierce, L. Romberg, Y. Harada, and T. Yanagida. Direct observation of single kinesin molecules moving along microtubules. *Nature*, 380:451–453, 1996.

[20] A. B. Kolomeisky. Motor proteins and molecular motors: how to operate machines at the nanoscale. *J. Phys.: Condens. Matter*, 25:463101, 2013.

[21] R. D. Vale, T. S. Reese, and M. P. Sheetz. Identification of a novel force-generating protein, kinesin, involved in microtubule-based motility. *Cell*, 42:39–50, 1985.

[22] P. D. Boyer. The ATP synthase - a splendid molecular machine. *Annu. Rev. Biochem.*, 66:717–749, 1997.

[23] P. V. Cornish and T. Ha. A survey of single-molecule techniques in chemical biology. *ACS Chemical Biology*, 2:53–61, 2007.

[24] P. R. Selvin and T. Ha. *Single Molecule Techniques: A Laboratory Manual*. Cold Spring Harbor Laboratory Press, New York, December 2007.

[25] C. Veigel and C. F. Schmidt. Moving into the cell: single-molecule studies of molecular motors in complex environments. *Nature Rev. Mol. Cell Biol.*, 12:163–176, 2011.

[26] A. B. Kolomeisky and M. E. Fisher. Molecular motors: A theorist's perspective. *Ann. Rev. Phys. Chem.*, 58:675–695, 2007.

[27] A. W. C. Lau, D. Lacoste, and K. Mallick. Non-equilibrium fluctuations and mechanochemical couplings of a molecular motor. *Phys. Rev. Lett.*, 99:158102, 2007.

[28] S. Liepelt and R. Lipowsky. Kinesin's network of chemomechanical motor cycles. *Phys. Rev. Lett.*, 98:258102, 2007.

[29] R. Lipowsky and S. Liepelt. Chemomechanical coupling of molecular motors: Thermodynamics, network representations, and balance conditions. *J. Stat. Phys.*, 130:39–67, 2008.

[30] R. Lipowsky, S. Liepelt, and A. Valleriani. Energy conversion by molecular motors coupled to nucleotide hydrolysis. *J. Stat. Phys.*, 135:951–975, 2009.

[31] R. D. Astumian. Thermodynamics and kinetics of molecular motors. *Biophys. J.*, 98:2401–2409, 2010.

[32] F. Jülicher, A. Ajdari, and J. Prost. Modeling molecular motors. *Rev. Mod. Phys.*, 69(4):1269–1282, 1997.

[33] P. Reimann. Brownian motors: noisy transport far from equilibrium. *Phys. Rep.*, 361:57, 2002.

[34] M. E. Fisher and A. B. Kolomeisky. The force exerted by a molecular motor. *Proc. Natl. Acad. Sci. U.S.A.*, 96:6597, 1999.

[35] H. Qian. A simple theory of motor protein kinetics and energetics. II. *Biophys. Chem.*, 83:35–43, 2000.

[36] Y. C. Kim and M. E. Fisher. Vectorial loading of processive motor proteins:

implementing a landscape picture. *J. Phys.: Condens. Matter*, 17:S3821, 2005.

[37] S. Liepelt and R. Lipowsky. Steady-state balance conditions for molecular motor cycles and stochastic nonequilibrium processes. *EPL*, 77:50002, 2007.

[38] U. Seifert. Efficiency of autonomous soft nano-machines at maximum power. *Phys. Rev. Lett.*, 106:020601, 2011.

[39] N. Golubeva and A. Imparato. Efficiency at maximum power of interacting molecular machines. *Phys. Rev. Lett.*, 109:190602, 2012.

[40] N. Golubeva and A. Imparato. Maximum power operation of interacting molecular motors. *Phys. Rev. E*, 88:012114, Jul 2013.

[41] P. Gaspard and E. Gerritsma. The stochastic chemomechanics of the F_1-ATPase molecular motor. *J. Theor. Biol.*, 247:672–686, 2007.

[42] N. Golubeva, A. Imparato, and L. Peliti. Efficiency of molecular machines with continuous phase space. *EPL*, 97:60005, 2012.

[43] N. G. van Kampen. *Stochastic Processes in Physics and Chemistry*. North-Holland, Amsterdam, 1981.

[44] H. Risken. *The Fokker-Planck Equation*. Springer-Verlag, Berlin, 2nd edition, 1989.

[45] C. W. Gardiner. *Handbook of Stochastic Methods*. Springer-Verlag, Berlin, 3rd edition, 2004.

[46] R. Kubo, M. Toda, and N. Hashitsume. *Statistical Physics II*. Springer-Verlag, Berlin, 2nd edition, 1991.

[47] T. L. Hill. *Free Energy Transduction and Biochemical Cycle Kinetics*. Dover, Mineola, New York, 2nd edition, 1989.

[48] S. Katz, J. L. Lebowitz, and H. Spohn. Nonequilibrium steady states of stochastic lattice gas models of fast ionic conductors. *J. Stat. Phys.*, 34:497–537, 1984.

[49] C. Maes and M. H. van Wieren. A Markov model for kinesin. *J. Stat. Phys.*, 112:329, 2003.

[50] U. Seifert. Generalized Einstein or Green-Kubo relations for active biomolecular transport. *Phys. Rev. Lett.*, 104:138101, 2010.

[51] U. Seifert. Stochastic thermodynamics of single enzymes and molecular motors. *Eur. Phys. J. E*, 34:26, 2011.

[52] M. Bauer and F. Cornu. Local detailed balance: a microscopic derivation. *J. Phys. A: Math. Theor.*, 48:015008, 2015.

[53] K. Sekimoto. Langevin equation and thermodynamics. *Prog. Theor. Phys. Supp.*, 130:17, 1998.

[54] U. Seifert. Entropy production along a stochastic trajectory and an integral fluctuation theorem. *Phys. Rev. Lett.*, 95:040602, 2005.

[55] B. Roux, editor. *Molecular Machines*. World Scientific, 2011.

[56] G. Oster and H. Wang. Rotary protein motors. *Trends in Cell Biology*, 13:114–121, 2003.

[57] D. Chowdhury. Stochastic mechano-chemical kinetics of molecular motors: A multidisciplinary enterprise from a physicist's perspective. *Phys. Rep.*, 529:1 – 197, 2013.

[58] S. X. Sun, H. Wang, and G. Oster. Asymmetry in the F_1-ATPase and its implications for the rotational cycle. *Biophys. J.*, 86:1373–1384, 2004.

[59] J. Xing, F. Bai, R. Berry, and G. Oster. Torque - speed relationship of the bacterial flagellar motor. *Proc. Natl. Acad. Sci. U.S.A.*, 103:1260–1265, 2006.

[60] L. Romberg and R. D. Vale. Chemomechanical cycle of kinesin differs from that of myosin. *Nature*, 361:168–170, 1993.

[61] N. R. Guydosh and S. M. Block. Backsteps induced by nucleotide analogs suggest the front head of kinesin is gated by strain. *Proc. Natl. Acad. Sci. U.S.A.*, 103:8054–8059, 2006.

[62] W. Junge, H. Sielaff, and S. Engelbrecht. Torque generation and elastic power transmission in the rotary F_oF_1-ATPase. *Nature*, 459:364–370, 2009.

[63] H.M. Berman, J. Westbrook, Z. Feng, G. Gilliland, T.N. Bhat, H. Weissig, I.N. Shindyalov, and P.E. Bourne. The Protein Data Bank. *Nucleic Acids Res.*, 28:235–242, 2000. www.rcsb.org.

[64] R. D. Vale. The molecular motor toolbox for intracellular transport. *Cell*, 112:467–480, 2003.

[65] P. D. Boyer. The binding change mechanism for ATP synthase - Some probabilities and possibilities. *Biochim. Biophys. Acta*, 1140:215–250, 1993.

[66] T. Elston, H. Wang, and G. Oster. Energy transduction in ATP synthase. *Nature*, 391:510–513, 1998.

[67] M. Yoshida, E. Muneyuki, and T. Hisabori. ATP synthase - a marvellous rotary engine of the cell. *Nat. Rev. Mol. Cell Biol.*, 2:669–677, 2001.

[68] D. Okuno, R. Iino, and H. Noji. Rotation and structure of F_oF_1-ATP synthase. *J Biochem*, 149:655–664, 2011.

[69] J. Czub and H. Grubmüller. Torsional elasticity and energetics of F_1-ATPase. *Proc. Natl. Acad. Sci. U.S.A.*, 108:7408–7413, 2011.

[70] H. Sielaff and M. Börsch. Twisting and subunit rotation in single F_oF_1-ATP synthase. *Phil Trans R Soc B*, 368:20120024, 2012.

[71] G. Oster and H. Wang. Reverse engineering a protein: the mechanochemistry of ATP synthase. *Biochim. Biophys. Acta*, 1458:482–510, 2000.

[72] S. Mukherjee and A. Warshel. Realistic simulations of the coupling between the protomotive force and the mechanical rotation of the F_o-ATPase. *Proc. Natl. Acad. Sci. U.S.A.*, 109:14876–14881, 2012.

[73] H. Noji, R. Yasuda, M. Yoshida, and K. Kinosita. Direct observation of the rotation of F_1-ATPase. *Nature*, 386:299–302, 1997.

[74] R. Yasuda, H. Noji, M. Yoshida, K. Kinosita Jr., and H. Itoh. Resolution of distinct rotational substeps by submillisedcond kinetic analysis of F_1-ATPase. *Nature*, 410:898, 2001.

[75] H. Wang and G. Oster. Energy transduction in the F_1 motor of ATP synthase. *Nature*, 396:279–282, 1998.

[76] E. Gerritsma and P. Gaspard. Chemomechanical coupling and stochastic thermodynamics of the F_1-ATPase molecuar motor with an applied external torque. *Biophys. Rev. Lett.*, 5:163–208, 2010.

[77] S. Toyabe, T. Watanabe-Nakayama, T. Okamoto, S. Kudo, and E. Muneyuki. Thermodynamic efficiency and mechanochemical coupling of F_1-ATPase. *Proc. Natl. Acad. Sci. U.S.A.*, 108:17951–17956, 2011.

[78] H. Noji, D. Okuno, and T. Ikeda. Mechanochemistry of F_1 motor protein. *Chem. Sci.*, 2:2086–2093, 2011.

[79] R. Watanabe and H. Noji. Chemomechanical coupling mechanism of F_1-ATPase: Catalysis and torque generation. *FEBS Letters*, 587:1030–1035, 2013.

[80] R. Watanabe, K. V. Tabata, R. Iina, H. Ueno, M. Iwamoto, S. Oiki, and H. Noji. Biased brownian stepping rotation of F_oF_1-ATP synthase driven by proton motive force. *Nat. Commun.*, 4:1631, 2013.

[81] H. Itoh, Takahashi A., K. Adachi, H. Noji, R. Yasuda, M. Yoshida, and K. Kinosita. Mechanically driven ATP synthesis by F_1-ATPase. *Nature*, 427:465–468, 2004.

[82] J. P. Abrahams, A. G. W. Leslie, R. Lutter, and J. E. Walker. Structure at 2.8 A resolution of F_1-ATPase from bovine heart mitochondria. *Nature*, 370:621–628, 1994.

[83] J. Weber and A. E. Senior. Catalytic mechanism of F_1-ATPase. *Biochim. Biophys. Acta*, 1319:19–58, 1997.

[84] K. Shimabukuro, R. Yasuda, E. Muneyuki, K. Y. Hara, K. Kinosita, and M. Yoshida. Catalysis and rotation of F_1 motor: Cleavage of ATP at the catalytic site occurs in 1 ms before 40° substep rotation. *Proc. Natl. Acad. Sci. U.S.A.*, 100:14713–14736, 2003.

[85] T Nishizaka, K Oiwa, H Noji, S Kimura, E Muneyuki, M Yoshida, and K Kinosita. Chemomechanical coupling in F_1-ATPase revealed by simultaneous observation of nucleotide kinetics and rotation. *Nat. Struct. Mol. Biol.*, 11(2):142–148, FEB 2004.

[86] Y Rondelez, G Tresset, T Nakashima, Y Kato-Yamada, H Fujita, S Takeuchi, and H Noji. Highly coupled ATP synthesis by F_1-ATPase single molecules. *Nature*, 433(7027):773–777, FEB 17 2005.

[87] K. Adachi, K. Oiwa, T. Nishizaka, S. Furuike, H. Noji, H. Itoh, M. Yoshida, and K. Kinosita. Coupling of rotation and catalysis in F_1-ATPase revealed by single-molecule imaging and manipulation. *Cell*, 130:309–321, 2007.

[88] D. Okunoa, R. Fujisawaa, R. Iinoa, Y. Hirono-Harab, H. Imamuraa, and H. Noji. Correlation between the conformational states of F_1-ATPase as determined from its crystal structure and single-molecule rotation. *Proc. Natl. Acad. Sci. U.S.A.*, 105:20722–20727, 2008.

[89] R. Watanabe, R. Iino, and H. Noji. Phosphate release in F_1-ATPase catalytic cycle follows ADP release. *Nat Chem Biol*, 6:814–820, 2010.

[90] K. Okazaki and G. Hummer. Phosphate release coupled to rotary motion of F_1-ATPase. *Proc. Natl. Acad. Sci. U.S.A.*, 110:16468–16473, 2013.

[91] J. R. Sellers. Myosins: a diverse superfamily. *Biochim. Biophys. Acta*, 1496:3–22, 2000.

[92] A. B. Kolomeisky and M. E. Fisher. A simple kinetic model describes the processivity of myosin-V. *Biophys. J.*, 84:1642–1650, 2003.

[93] A. Gennerich and R. D. Vale. Walking the walk: how kinesin and dynein coordinate their steps. *Curr. Opin. Cell Biol.*, 21:59–67, 2009.

[94] A. Yildiz, M. Tomishige, R. D. Vale, and P. R. Selvin. Kinesin walks hand-over-hand. *Science*, 303:676–678, 2004.

[95] K. Svoboda, C. F. Schmidt, B. J. Schnapp, and S. M. Block. Direct observation of kinesin stepping by optical trapping interferometry. *Nature*, 365:721, 1993.

[96] B. Milic, J. O. L. Andreasson, W. O. Hancock, and S. M. Block. Kinesin processivity is gated by phosphate release. *Proc. Natl. Acad. Sci. U.S.A.*, 111:14136–14140, 2014.

[97] F. J. Kull, E. P. Sablin, R. Lau, R. J. Fletterick, and R. D. Vale. Crystal structure of the kinesin motor domain reveals a structural similarity to myosin. *Nature*, 380:550–555, 1996.

[98] K. Visscher, M. Schnitzer, and S. M. Block. Single kinesin molecules studied with a molecular force clamp. *Nature*, 400:184–189, 1999.

[99] N. J. Carter and R. A. Cross. Mechanics of the kinesin step. *Nature*, 435:308, 2005.

[100] M. E. Fisher and A. B. Kolomeisky. Simple mechanochemistry describes the dynamics of kinesin molecules. *Proc. Natl. Acad. Sci. U.S.A.*, 98:7748–7753, 2001.

[101] Y. Chen. Theoretical formalism for kinesin motility I. Bead movement powered by single one-headed kinesins. *Biophys. J.*, 78:313–321, 2000.

[102] Y. Chen and B. Yan. Theoretical formalism for bead movement powered by single two-headed motors in a motility assay. *Biophys. Chem.*, 91:79–91, 2001.

[103] S. Liepelt and R. Lipowsky. Operation modes of the molecular motor kinesin. *Phys. Rev. E*, 79:011917, 2009.

[104] N. J. Carter and R. A. Cross. Kinesin's moonwalk. *Curr. Opin. Cell Biol.*, 18:61–67, 2006.

[105] S. Liepelt and R. Lipowsky. Impact of slip cycles on the operation modes and efficiency of molecular motors. *J. Stat. Phys.*, 141:1–16, 2010.

[106] S. P. Gross. Hither and yon: a review of bi-directional microtubule-based transport. *Phys. Biol.*, 1:R1, 2004.

[107] M. A. Welte. Bidirectional transport along microtubules. *Curr. Biol.*, 14:R525–R537, 2004.

[108] A. Kunwar, M. Vershinin, J. Xu, and S. P. Gross. Stepping, strain gating, and an unexpected force-velocity curve for multiple-motor-based transport. *Curr. Biol.*, 18:1173–1183, 2008.

[109] C. B. Korn, S. Klumpp, R. Lipowsky, and U. S. Schwarz. Stochastic simulations of cargo transport by processive molecular motors. *J. Chem. Phys.*, 131:245107, 2009.

[110] S. Bouzat and F. Falo. The influence of direct motor-motor interaction in models for cargo transport by a single team of motors. *Phys. Biol.*, 7:046009, 2010.

[111] W. O. Hancock. Bidirectional cargo transport: moving beyond tug of war. *Nat. Rev. Mol. Cell Biol.*, 15:615–628, 2014.

[112] S. Klein, C. Appert-Rolland, and L. Santen. Environmental control of microtubule-

based bidirectional cargo transport. *EPL*, 107:18004, 2014.

[113] K. Adachi, R. Yasuda, H. Noji, H. Itoh, Y. Harada, M. Yoshida, and K. Kinosita. Stepping rotation of F_1-ATPase visualized through angle-resolved single-fluorophore imaging. *Proc. Natl. Acad. Sci. U.S.A.*, 97(13):7243–7247, 2000.

[114] The Nobel Prize in Chemistry 2014 - Advanced Information. *Nobelprize.org*. Nobel Media AB 2014. Web. 20 Jan 2015.

[115] B. Huang, M. Bates, and X. Zhuang. Super-resolution fluorescence microscopy. *Annu. Rev. Biochem.*, 78:993–1016, 2009.

[116] S. Ernst, M. G. Düser, N. Zarrabi, S.y D. Dunn, and M. Börsch. Elastic deformations of the rotary double motor of single F_oF_1-ATP synthases detected in real time by Förster resonance energy transfer. *Biochim. Biophys. Acta*, 1817:1722–1731, 2012.

[117] B. Prevo and E. J. G. Peterman. Förster resonance energy transfer and kinesin motor proteins. *Chem. Soc. Rev.*, 43:1144–1155, 2014.

[118] S. Toyabe and E. Muneyuki. Nanosized free-energy transducer F_1-ATPase achieves 100% efficiency at finite time operation. *arXiv:1210.4017*, 2012.

[119] K. Hayashi, H. Ueno, R. Iino, and H. Noji. Fluctuation theorem applied to F_1-ATPase. *Phys. Rev. Lett.*, 104:218103, 2010.

[120] H. Ueno, S. Nishikawa, R. Iino, K. Tabata, S. Sakakihara, T. Yanagida, and H. Noji. Simple dark-fiel microscopy with nanometer spatial precision and microsecond temporal resolution. *Biophys. J.*, 98:2014–2023, 2010.

[121] R. Watanabe, K. Hayashi, H. Ueno, and H. Noji. Catalysis-enhancement via rotary fluctuation of F_1-ATPase. *Biophys. J.*, 105:2385 – 2391, 2013.

[122] R. S. Rock, S. E. Rice, A. L. Wells, T. J. Purcell andJ. A. Spudich, and H. L Sweeney. Myosin VI is a processive motor with a large step size. *Proc. Natl. Acad. Sci. U.S.A.*, 98:13655, 2001.

[123] C. S. Peskin and T. C. Elston. The role of protein flexibility in molecular motor function: Coupled diffusion in a tilted periodic potential. *SIAM J. Appl. Math.*, 60:842–867, 2000.

[124] C. S. Peskin, D. You, and T. C. Elston. Protein flexibility and the correlation ratchet. *SIAM J. Appl. Math.*, 61:776–791, 2000.

[125] Y. Chen, B. Yan, and R. J. Rubin. Fluctuations and randomness of movement of the bead powered by a single kinesin molecule in a force-clamped motility assay: Monte carlo simulations. *Biophys. J.*, 83:2360–2369, 2002.

[126] K. B. Zeldovich, J. F. Joanny, and J. Prost. Motor proteins transporting cargos. *Eur. Phys. J. E*, 17:155–163, 2005.

[127] H. Wang and H. Zhou. Stokes efficiency of molecular motor-cargo systems. *Abstract and Applied Analysis*, 2008:241736, 2008.

[128] P. Pietzonka, E. Zimmermann, and U. Seifert. Fine-structured large deviations and the fluctuation theorem: Molecular motors and beyond. *EPL*, 107:20002, 2014.

[129] D. Keller and C. Bustamante. The mechanochemistry of molecular motors. *Biophys. J.*, 78:541–556, 2000.

[130] C. Bustamante, D. Keller, and G. Oster. The physics of molecular motors. *Accounts Chem. Res.*, 34:412–420, 2001.

[131] O. Kedem and S. R. Caplan. Degree of coupling and its relation to efficiency of energy conversion. *Trans. Faraday Soc.*, 61:1897, 1965.

[132] A. Parmeggiani, F. Jülicher, A. Ajdari, and J. Prost. Energy transduction of isothermal ratchets: Generic aspects and specific examples close to and far from equilibrium. *Phys. Rev. E*, 60:2127, 1999.

[133] D. Mandal and C. Jarzynski. Hybrid models of molecular machines and the no-pumping theorem. *J. Chem. Phys.*, 137:234104, 2012.

[134] C. Kutzner, J. Czub, and H. Grubmüller. Keep it flexible: Driving macromolecular rotary motions in atomistic simulations with GROMACS. *J. Chem. Theory Comput.*, 7:1381–1393, 2011.

[135] R. E. L. DeVille and E. Vanden-Eijnden. Regular gaits and optimal velocities for motor proteins. *Biophys. J.*, 95:2681 – 2691, 2008.

[136] S. J. Lade, E. M. Craig, and H. Linke. Effectiveness of beads for tracking small-scale molecular motor dynamics. *Phys. Rev. E*, 84:021907, 2011.

[137] E. Zimmermann and U. Seifert. Effective rates from thermodynamically consistent coarse-graining of models for molecular motors with probe particles. *Phys. Rev. E*, 91:022709, 2015.

[138] R. Watanabe, D. Okuno, S. Sakakihara, K. Shimabukuro, R. Iino, M. Yoshida, and H. Noji. Mechanical modulation of catalytic power on F_1-ATPase. *Nat. Chem. Biol.*, 8:86–92, 2012.

[139] J. M. R. Parrondo and B. J. De Cisneros. Energetics of Brownian motors: a review. *Applied Physics A*, 75:179, 2002.

[140] A. Efremov and Z. Wang. Universal optimal working cycles of molecular motors. *Phys. Chem. Chem. Phys.*, 13:6223–6233, 2011.

[141] K. Kawaguchi and M. Sano. Efficiency of free energy transduction in autonomous systems. *J. Phys. Soc. Japan*, 80:083003, 2011.

[142] I. Derenyi, M. Bier, and R. D. Astumian. Generalized efficiency and its application to microscopic engines. *Phys. Rev. Lett.*, 83:903, 1999.

[143] H. Wang and G. F. Oster. The Stokes efficiency for molecular motors and its applications. *Europhys. Lett.*, 57:134, 2002.

[144] D. Suzuki and T. Munakata. Rectification efficiency of a Brownian motor. *Phys. Rev. E*, 68:021906, 2003.

[145] H. Wang. Chemical and mechanical efficiencies of molecular motors and implications for motor mechanisms. *J. Phys. Cond. Mat.*, 17:S3997–S4014, 2005.

[146] M. Qian, X. Zhang, R. J. Wilson, and J. Feng. Efficiency of Brownian motors in terms of entropy production rate. *EPL*, 84:10014, 2008.

[147] E. Boksenbojm and B. Wynants. The entropy and efficiency of a molecular motor model. *J. Phys. A: Math. Theor.*, 42:445003, 2009.

[148] S. Toyabe, H. Ueno, and E. Muneyuki. Recovery of state-specific potential of molecular motor from single-molecule trajectory. *EPL*, 97:40004, 2012.

[149] R. Yasuda, H. Noji, K. Kinosita, and M. Yoshida. F_1-ATPase is a highly efficient

molecular motor that rotates with discrete 120 degree steps. *Cell*, 93:1117, 1998.

[150] E. Muneyuki, T. Watanabe-Nakayama, T. Suzuki, M. Yoshida, T. Nishizaka, and H. Noji. Single molecule energetics of F_1-ATPase motor. *Biophys. J.*, 92:1806–1812, 2007.

[151] U. Seifert. Stochastic thermodynamics: Principles and perspectives. *Eur. Phys. J. B*, 64:423–431, 2008.

[152] T. Hatano and S. Sasa. Steady-state thermodynamics of Langevin systems. *Phys. Rev. Lett.*, 86:3463, 2001.

[153] T. Speck and U. Seifert. Restoring a fluctuation-dissipation theorem in a nonequilibrium steady state. *Europhys. Lett.*, 74:391, 2006.

[154] K. Kinosita, K. Adachi, and H. Itoh. Rotation of F_1-ATPase: How an ATP- driven molecular machine may work. *Annu. Rev. Biophys. Biomol. Struct.*, 33:245–268, 2004.

[155] T. L. Hill. Theoretical formalism for the sliding filament model of contraction of striated muscle Part I. *Prog. Biophys. Mol. Biol*, 28:267–340, 1974.

[156] T. Harada and S. Sasa. Equality connecting energy dissipation with a violation of the fluctuation-response relation. *Phys. Rev. Lett.*, 95:130602, 2005.

[157] T. Schmiedl and U. Seifert. Efficiency of molecular motors at maximum power. *EPL*, 83:30005, 2008.

[158] S. Toyabe and E. Muneyuki. Single molecule thermodynamics of ATP synthesis by F_1 -ATPase. *New J. Phys.*, 17:015008, 2015.

[159] M. J. Schilstra and S. R. Martin. An elastically tethered viscous load imposes a regular gait on the motion of myosin-V. Simulation of the effect of transient force relaxation on a stochastic process. *J. R. Soc. Interface*, 3:153–165, 2006.

[160] U. Seifert and T. Speck. Fluctuation-dissipation theorem in nonequilibrium steady states. *EPL*, 89:10007, 2010.

[161] R. Kubo. Fluctuation-dissipation theorem. *Rep. Progr. Phys.*, 29:255, 1966.

[162] U. Marconi, A. Puglisi, L. Rondoni, and A. Vulpiani. Fluctuation-dissipation: Response theory in statistical physics. *Phys. Rep.*, 461:111–195, 2008.

[163] E. Zimmermann. Fluktuationen in aktiven biomolekularen Systemen. Master's thesis, Universität Stuttgart, 2011.

[164] X. Li and A. B. Kolomeisky. Mechanisms and topology determination of complex chemical and biological network systems from first-passage theoretical approach. *J. Chem. Phys.*, 139:144106, 2013.

[165] A. Valleriani, X. Li, and A. B. Kolomeisky. Unveiling the hidden structure of complex stochastic biochemical networks. *J. Chem. Phys.*, 140:064101, 2014.

[166] K. Hayashi, C. G. Pack, M. K. Sato, K. Mouri, K. Kaizu, K. Takahashi, and Y. Okada. Viscosity and drag force involved in organelle transport: Investigation of the fluctuation dissipation theorem. *Eur. Phys. J. E*, 36(12):136, 2013.

[167] T. L. Hill. Studies in irreversible thermodynamics IV. Diagrammatic representation of steady state fluxes for unimolecular systems. *J. Theor. Biol.*, 10:442, 1966.

[168] J. Schnakenberg. Network theory of microscopic and macroscopic behavior of

master equation systems. *Rev. Mod. Phys.*, 48:571, 1976.

[169] B. Altaner, S. Grosskinsky, S. Herminghaus, L. Katthän, M. Timme, and J. Vollmer. Network representations of nonequilibrium steady states: Cycle decompositions, symmetries, and dominant paths. *Phys. Rev. E*, 85:041133, 2012.

[170] S. Rahav and C. Jarzynski. Fluctuation relations and coarse-graining. *J. Stat. Mech.: Theor. Exp.*, 2007:P09012, 2007.

[171] G. Nicolis. Transformation properties of entropy production. *Phys. Rev. E*, 83:011112, 2011.

[172] M. Esposito. Stochastic thermodynamics under coarse-graining. *Phys. Rev. E*, 85:041125, 2012.

[173] S. Bo and A. Celani. Entropy production in stochastic systems with fast and slow time-scales. *J. Stat. Phys.*, 154:1325–1351, 2014.

[174] M. Santillán and H. Qian. Irreversible thermodynamics in multiscale stochastic dynamical systems. *Phys. Rev. E*, 83:041130, 2011.

[175] K. Kawaguchi and Y. Nakayama. Fluctuation theorem for hidden entropy production. *Phys. Rev. E*, 88:022147, 2013.

[176] S. Pigolotti and A. Vulpiani. Coarse graining of master equations with fast and slow states. *J. Chem. Phys.*, 128:154114, 2008.

[177] A. Puglisi, S. Pigolotti, L. Rondoni, and A. Vulpiani. Entropy production and coarse graining in Markov processes. *J. Stat. Mech.: Theor. Exp.*, 2010:P05015, 2010.

[178] B. Altaner and J. Vollmer. Fluctuation preserving coarse graining for biochemical systems. *Phys. Rev. Lett.*, 108:228101, 2012.

[179] C. P. Amann, T. Schmiedl, and U. Seifert. Communications: Can one identify nonequilibrium in a three-state system by analyzing two-state trajectories? *J. Chem. Phys.*, 132:041102, 2010.

[180] J. Mehl, B. Lander, C. Bechinger, V. Blickle, and U. Seifert. Role of hidden slow degrees of freedom in the fluctuation theorem. *Phys. Rev. Lett.*, 108:220601, 2012.

[181] A. Crisanti, A. Puglisi, and D. Villamaina. Non-equilibrium and information: the role of cross-correlations. *Phys. Rev. E*, 85:061127, 2012.

[182] A. Gomez-Marin, J. M. R. Parrondo, and C. Van den Broeck. Lower bounds on dissipation upon coarse-graining. *Phys. Rev. E*, 78:011107, 2008.

[183] D. Tsygankov and M. E. Fisher. Kinetic models for mechanoenzymes: Structural aspects under large loads. *J. Chem. Phys.*, 128:015102, 2008.

[184] G. Lattanzi and A. Maritan. Force dependent transition rates in chemical kinetics models for motor proteins. *J. Chem. Phys.*, 117:10339–10349, 2002.

[185] G. Lattanzi and A. Maritan. Coarse grained models: the kinetics of motor proteins. *Comp. Mater. Sci.*, 30:172 – 179, 2004.

[186] P. R. Kramer, J. C. Latorre, and A. A. Khan. Two coarse-graining studies of stochastic models in molecular biology. *Commun. Math. Sci.*, 8:481 – 517, 2010.

[187] H. Qian. The mathematical theory of molecular motor movement and chemomechanical energy transduction. *J. Math. Chem.*, 27:219–234, 2000.

[188] B. Derrida. Velocity and diffusion constant of a periodic one-dimensional hopping

model. *J. Stat. Phys.*, 31:433–450, 1983.

[189] B. C. Carter, M. Vershinin, and S. P. Gross. A comparison of step-detection methods: How well can you do? *Biophys. J*, 94:306–319, 2008.

[190] F. E. Müllner, S. Syed, P. R. Selvin, and F. J. Sigworth. Improved hidden Markov models for molecular motors, part 1: Basic theory. *Biophys. J.*, 99:3684–3695, 2010.

[191] M. A. Little, B. C. Steel, F. Bai, Y. Sowa, T. Bilyard, D. M. Mueller, R. M. Berry, and N. S. Jones. Steps and bumps: Precision extraction of discrete states of molecular machines. *Biophys. J.*, 101:477–485, 2011.

[192] D. Hartich, A. C. Barato, and U. Seifert. Stochastic thermodynamics of bipartite systems: transfer entropy inequalities and a Maxwell's demon interpretation. *J. Stat. Mech.: Theor. Exp.*, 2014:P02016, 2014.

[193] N. Shiraishi and T. Sagawa. Fluctuation theorem for partially masked nonequilibrium dynamics. *Phys. Rev. E*, 91:012130, 2015.

[194] H. Ge and H. Qian. Dissipation, generalized free energy, and a self-consistent nonequilibrium thermodynamics of chemically driven open subsystems. *Phys. Rev. E*, 87:062125, 2013.

[195] D. T. Gillespie. Exact stochastic simulation of coupled chemical reactions. *J. Phys. Chem.*, 81:2340, 1977.

[196] D. T. Gillespie. *Markov Processes.* Academic Press, San Diego, 1992.

Danksagung

Ich möchte allen danken, die zum Gelingen dieser Arbeit beigetragen haben.

An erster Stelle gilt mein Dank Herrn Prof. Dr. Udo Seifert für die Ermöglichung dieser Arbeit, die wissenschaftliche Betreuung und sein Engagement.

Herrn Prof. Dr. Christian Holm danke ich für die Übernahme und das Erstellen des Mitberichts.

Anja Steinhauser danke ich für ihre Hilfsbereitschaft bei allen organisatorischen Belangen.

Ich danke allen Institutsmitgliedern, mit denen ich eine schöne Zeit verbracht habe. Insbesondere danke ich Patrick Pietzonka für die gute Zusammenarbeit, meinen Korrekturlesern Eckhard Dieterich, David Hartich, Sebastian Goldt und Patrick Pietzonka sowie den Systemadministratoren.

Außerdem danke ich Kay Brandner, Eckhard Dieterich, Patrick Pietzonka, Dr. Boris Lander, Dr. David Abreu und David Hartich für aufschlussreiche und unterhaltsame Gespräche aller Art und für ihre Hilfe.

Meiner Familie danke ich für vielfältige Unterstützung, vor allem Helene Zimmermann und meinem forfour.

Ehrenwörtliche Erklärung

Ich erkläre, dass ich diese Arbeit selbstständig verfasst und keine anderen als die angegebenen Quellen und Hilfsmittel verwendet habe.

Stuttgart, den 13. Februar 2015 Eva Zimmermann